Development of Surface Roughness in AA6111 Aluminum Alloy

Victoria Oswell

September 23, 2005

DEVELOPMENT OF SURFACE ROUGHNESS IN AA6111 ALUMINUM ALLOY

By

VICTORIA OSWELL, B. ENG. SCTY.

September 23, 2005

A Thesis
Submitted to the School of Graduate Studies
in Partial Fulfilment of the Requirements
for the Degree
Master of Applied Science

McMaster University

MASTER of APPLIED SCIENCE (2005)
Electrical and Computer Eng

McMaster University
Hamilton, Ontario

TITLE: Development of Surface Roughness in AA6111 Aluminum Alloy

AUTHOR: Victoria Oswell, B. Eng. Scty. (McMaster University)

SUPERVISORS: Dr. D. S. Wilkinson and Dr. J. D. Embury

NUMBER OF PAGES: xi, 126

Abstract

The effect of strain hardening rate and material strength on the development of surface roughness in AA6111 was investigated. No measurable change in the rate of roughening, or in the surface morphology was observed due to altering the strain hardening rate by using different test temperatures. Changing the material strength and strain hardening rate by altering the precipitation state also gave no significant change in either roughening rate or morphology with respect to strain. The development of surface roughness is also independent of strain history. Samples subjected to an intermediate polish after 20% true strain resumed roughening at the same rate regardless of amount of previous tensile strain. The development of surface roughness is dependent on only the strain level to which the sheet is deformed. The surface morphology seems to be controlled by the combination and distribution of texture components on the surface. The rate of roughening is grain size dependent and the surface grain size may provide a key to controlling roughening.

Acknowledgements

There are three good reasons to pursue a Master's degree: an avid interest in the subject being studied, an aspiration to become a professor or researcher, or an interest in working with a particular group of researchers. I decided to do my Masters for none of the above reasons. As such, I truly thank all those who have helped me along this rather rocky journey known as a Masters degree in Applied Science. Thanks to Cyrus Jeejeebhoy, Laura Marie Piotrowicz, Jared Lenover, Jess Prendergast for their support and continual questioning "are you done yet?". A special thank you to all of my friends who provided a vital set of theatrical distractions (thanks to the cast and crew of SDF04 'Twelfth Night', and everyone involved in SDF05 especially Julie Ella Debeau, and Steve and Bryan Fotheringham) which helped focus my need to leave research to those who have more patience than myself. A very special thank you to my supervisors, Drs. David Wilkinson and David Embury for having the patience to let me find my way, and the wisdom to "snap back the leash" (so they say) when I wandered to far afield. Thank you also to Chris Pelow for helping me decipher the roughness data and explain what I am actually seeing. An extra thank you to my parents, John and Susan, for supporting my decision to stay in school, perhaps a little longer than anticipated. And finally, thank you to all my officemates in A206 - you know who you are - and Mike Greenwood and Erika Bellhouse for keeping the long days and nights very interesting.

Cheers,

Tori

Contents

List of Figures

List of Tables

Chapter 1

Introduction

There is a continuing interest in the automotive sector to decrease the overall weight of the vehicles produced to improve fuel efficiency. One technique that is widely used is switching to lighter weight materials, such as from drawing quality steel that is currently most commonly used in structural frames and body paneling, to aluminum for the same components. In North America, AA5754 and AA6111 are the aluminum grades typically selected for structural members and body panels respectively. Subsequently, there has been a great deal of research done on the properties of both grades.

As a material currently proposed for use in making automotive body panels, studies investigating AA6111 have often focused on how the material roughens with respect to the imposed strain path. Surface roughness affects several parameters important to the formation and finishing of products made from flat, thin rolled sheets, namely formability [1], paint/printability, and overall visual appearance.

This study will focus on factors which affect the development of surface roughness in AA6111 aluminum sheet. The objective of this study it to quantify the parameters affecting surface roughness development in AA 6111 aluminum alloy as a function of strain. The effects of orientation with respect to the rolling direction, strain hardening rate, heat treatment, and strain history were examined.

The study was based on isolating individual parameters to determine their influence on surface roughness development. Tensile behaviour for each sample set was measured to determine mechanical properties, such as yield strength, strain hardening rate and directionality. Three different tempers and three different test temperatures were used in combination with two orientations to the rolling direction to separate the affects of strength, strain hardening rate, and material anisotropy inherent in rolled sheet.

Chapter 2

Literature Review

There has been much interest in the processes involving roughening, or the development of surface features, on the free surface of sheet metals upon deformation. This section overviews the results reported from investigations conducted on how a free surface develops under deformation. Roughness occurs over a variety of length scales, from micro- to macro-roughening. This chapter is organized to begin with an introduction as to what is meant by roughening and a further explanation of the length-scales involved. It will outline the topics in decreasing order of scale, starting with parameters on the order of the the size of the entire sheet, and progressing to parameters which are on the order of the size of individual grains. In order, these topics include: sheet thickness, relationship between top and bottom surfaces, strain and strain state, sample orientation, grain size, crystallographic texture, and finally strain hardening rate.

2.1 Definition of Roughness and Length Scale

Roughness is a term used to describe both the morphology of a material's free surface and the amplitude (or height) of the surface features present. Roughness usually refers to surface features on the meso- to macroscopic scale. A surface can attain a 'roughness' by a variety of methods, such as contact with dies or other materials, deformation, machining marks, deformation, and corrosion to name a few [2]. The focus of this study is to develop a greater understanding of the development of surface roughness due to plastic deformation.

Deformation roughness occurs over microscopic, mesoscopic and macroscopic length scales. Microscopic roughening occurs within individual grains in the form of slip steps. Mesoscopic roughening occurs over several grains and is associated with 'orange-peel' type roughening. Macroscopic roughening spans multiple grains and forms correlated, long range surface features commonly referred to as roping or ridging. These features usually have an associated wavelength over which they occur. Figure 2.1 schematically shows short-range roughness which occurs on the mesoscopic scale, and long range roughness which occurs on the macroscopic scale. Of the three length scales, mesoscopic and macroscopic roughening affects have gained the most interest as they affect both the aesthetics of the material surface as well as the formability limits.

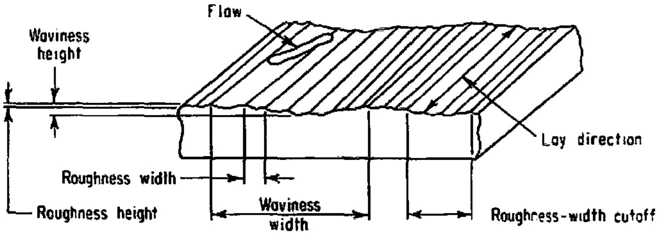

Figure 2.1: Schematic of the Different Roughness Length Scales. Taken from [3]

Surface roughness increases with deformation. It has been shown that as the amount of deformation increases, new surface features form on the surface, their amplitude increases, but the location of the resulting features (i.e. peaks or ridges, and valleys) on the surface does not change [4, 5]. Thomson and Nayak also investigated the effect of existing surface features on roughness development. The resulting line profiles of a polished sample of low-carbon steel with isolated engraved 'valleys' with increasing strain along the tensile axis shows that the existing valleys do not initially change until higher strains. However, new surface features begin to develop almost immediately upon testing [5], as seen in Figure 2.2. Figure 2.3 shows the change in surface topography over two grains in a sheet of 1mm thick Al-5%Mg with increasing tensile strain as measured by atomic force microscopy. As the strain increases, the grains start to rotate out of plane. This reaction becomes more apparent at strains higher than 3.5% [6].

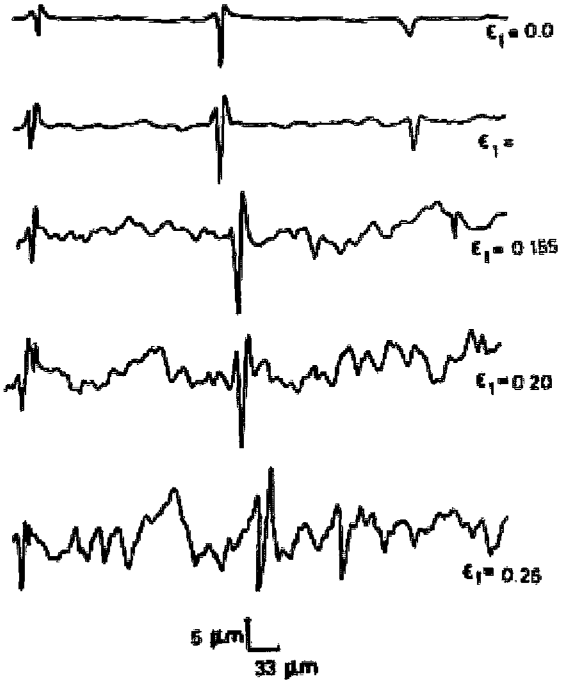

Figure 2.2: New Features forming on a surface after onset of deformation

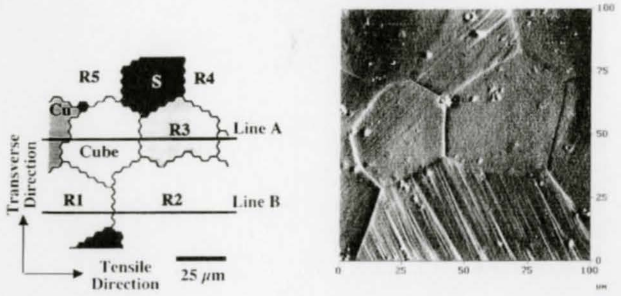

(a) Schematic of region scanned

(b) AFM image of area at 3.5% strain

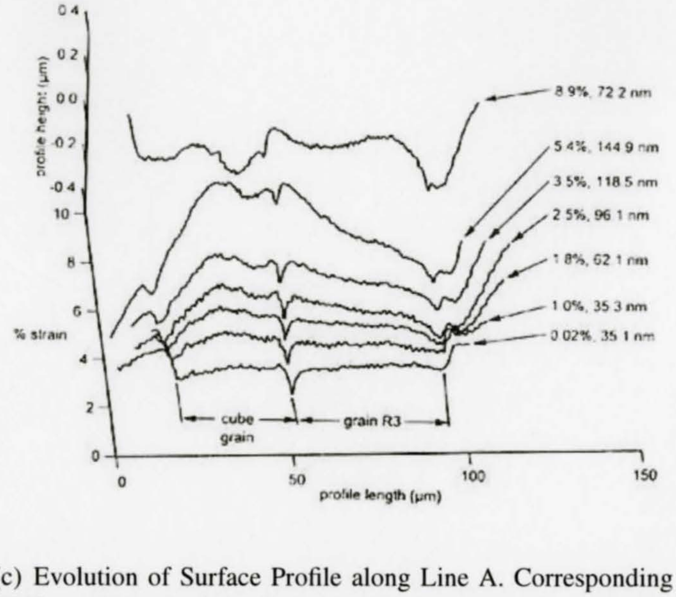

(c) Evolution of Surface Profile along Line A. Corresponding RMS roughness and tensile strain values are given for each profile.

Figure 2.3: Changes in Surface Topography with Increasing Tensile Strain. From [6]

2.2 Effect of Sheet Thickness

The effect of thickness was investigated by several researchers [5, 7, 8]. Thomson and Nayak tested low-carbon steel sheet with four different thicknesses in uniaxial tension. They reported a decrease in the roughness as the thickness increased for all but the thinnest sample, which is reported to be approaching plane stress [5]. However, reported results from hydraulic bulge tests show the development of surface roughness to be independent of sheet thickness for all thickness investigated [7, 8]. Shimizu et al. also reported roughness development is independent of sheet thickness on their tests on polycrystalline iron sheets 2.5mm and 4mm thick in uniaxial tension [4].

2.3 Relationship between Top and Bottom Surfaces

There has been much discussion and disagreement of the relationship of the topography between the top and bottom surfaces. Several different relationships have been suggested, as shown in Figure 2.4; ribbed, corrugated and random/irregular. Experimental work by Wittridge and Knutsen supported the development of a ribbed profile after 20% elongation [17]. However, Baczynski et al. reported neither a ribbed nor a corrugated surface to surface profile developed and the placement of ridges and valleys were irregular related when

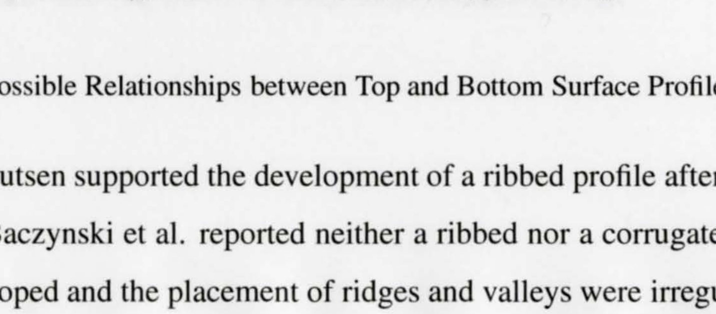

Figure 2.4: Possible Relationships between Top and Bottom Surface Profiles. From [14]

elongated to 15% strain [14]. Wu and Lloyd reported the relationship between the top and bottom surfaces develops with strain, from initially corrugated at small strains through irregular, to ribbed at higher strains [24]. Several models which have textural components running through the thickness of the model have shown that the texture component present is the main factor in determining the cross section profile when tested perpendicular tot eh rolling direction [2, 25]. Combinations of Cube and Goss, as well as Cube and S yielded ribbed profiles [2, 25] while combinations of S1 and S2 (same Taylor factor, opposite shear tendencies) yielded corrugated profiles [25]. By altering the texture component distribution, a combination of Cube and Goss components switched from a ribbed profile to a corrugated profile while a combination of Cube and S components retained a corrugated profile regardless of distribution [25], as shown in Figure 2.5.

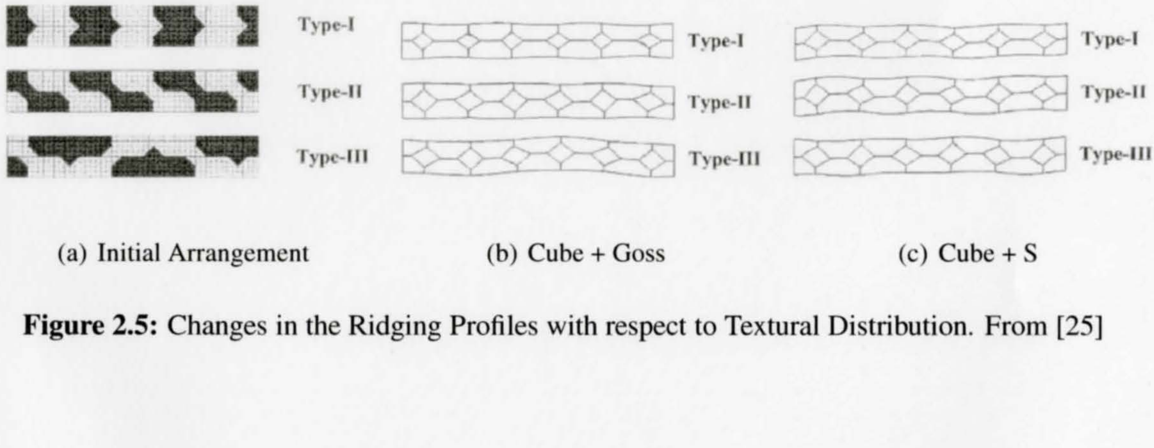

(a) Initial Arrangement (b) Cube + Goss (c) Cube + S

Figure 2.5: Changes in the Ridging Profiles with respect to Textural Distribution. From [25]

2.4 Effect of Magnitude of Strain and Strain State

A variety of researchers report, as shown in Figure 2.6, that the roughness increases linearly with strain. However, there have been conflicting reports as to the exact relationship between different combinations of strain-based and roughness parameters. Although Thomson and Nayak reported that the equivalent strain is not an adequate strain parameter, the equivalent strain has been used by many researchers [4, 9, 11] and gives a linear dependence between strain and roughness. In several studies, the thickness strain has been used

[7, 8]. It also reveals a mostly linear dependence. However, at thickness strains above 0.5 in equibiaxial stretching, the roughness increases rapidly as seen in Figure 2.6. This strain level is reported to be close to localized necking [8].

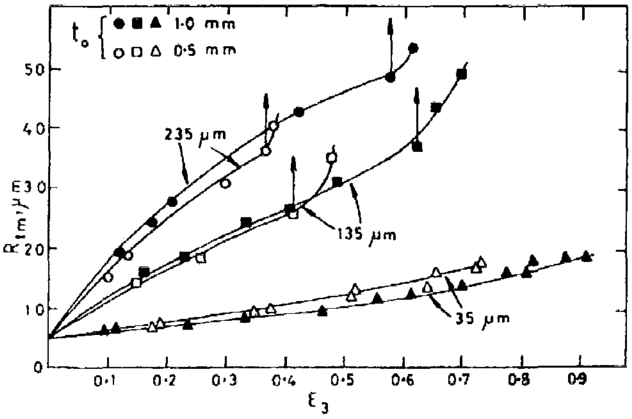

Figure 2.6: Effect of Roughness versus Thickness Strain for Grain Sizes and Sheet Thicknesses of 70-30 brass sheet. From [7]

The effect of strain state, as given by the ratio of minor to major strain, on the development of a surface has been debated for a number of years. This ratio is either reported as ρ or β and is in the form $\rho = \frac{\epsilon_2}{\epsilon_1}$. There seem to be contradicting reports as to the whether the strain state has any effect on surface roughness. Thomson and Nayak report a decrease in the roughness with respect to strain with an increase in strain ratio ρ from -1 to 1 on polished low-carbon steel. Kawai et al. [10] show an increasing dependence on strain state with increasing strain in pure aluminum 0.8mm thick with an initial surface roughness of 0.02μm C.L.A. C. L. A. refers to the 'centre line average', which is now commonly called the average roughness. As the strain ratio decreases from 1.0 to -0.44, the mean roughening rate increases slightly, leading to a larger change in the roughness with respect to strain state at higher strains . Guangnan et al. [11] also report a change in the roughening rate with respect to strain state, which is material dependent. They report very little difference in the roughness with respect to equivalent strain for the two types of aluminum tested regardless of initial roughness. However, each of the three steel sample sets showed a distinct spread in roughening rates with respect to strain depending if they were tested in uniaxial tension, plane strain, or equibiaxial stretching . In Becker's well-known paper [13] he reports both experimental and model-based results supporting the dependence of the roughening rate on the strain state. Experimentally, the mean roughening rate with respect to effective strain was greater for the sample tested in uniaxial tension than biaxial tension. Using a two-dimensional crystal plasticity model that accounts for crystallographic slip and grain rotation, Becker simulated the roughness for five strain histories. Unlike results reported by Thomson and Nayak or Kawai et al., there is no clear trend between the strain ratio and the rate of roughening; biaxial tension (ρ=1.0) and in-plane shear (ρ= -1.0) have very similar roughening rates. Simulated roughening in uniaxial (ρ= -0.5) and plane strain tension (ρ= 0.0) also show similar roughening rates. However, biaxial tension and in-plane shear have a lower roughening rate that uniaxial and plane strain tension [13]. Wilson et al. [8] reported strain state had no effect on copper samples tested with three different die aspect ratios, resulting in strain ratios of 1.0, 0.7 and 0.4. Again, the roughness increased linearly at the same rate with respect to thickness strain for all samples .

Thomson and Shafer [12] conducted experiments on low carbon steel and sintered copper tested with a variety of different stress states. The resulting measurement revealed that the rate of roughening changed between different stress states only at higher values of initial roughness. They report a strong dependence on stress state for steel samples tested with an initial roughness between 2.25 and 3.25μm C.L.A. However, for steel and copper samples with an initial roughness of 0.25μm C.L.A, there is no appreciable difference in roughening rate with respect to strain state. Roughness of all samples increased linearly with effective strain .

2.5 Effect of Tensile Axis-Rolling Direction Orientation

The orientation between the tensile axis and the rolling direction is a very important aspect with respect to the development of long range roughness. Mesoscale/Orange peel type roughening occurs regardless of orientation. However, roping is observed more prominently when the tensile axis is perpendicular to the rolling direction [13, 19, 21, 23, 25]. In automotive aluminum alloys, AA6111 specifically, it is reported that long range roughening effect, roping/ridging, develop parallel to the rolling direction when tested perpendicular to the rolling direction [14, 21].

The stated reasons for this distinct morphological difference between the two test orientations with respect to the rolling direction include anisotropy effects due to texture[14] which will be further discussed in a subsequent section. A change in strain path is reported to not only affect the magnitude of roughening, but the roughness with respect to orientation, which gives rise to an anisotropic effect to roughening. Kawai et al.'s [10] study reports that the slope of the difference between the average roughness measured parallel and perpendicular to the principle strain direction, $\Delta Ra = Ra_1 - Ra_2$, plotted against the principle in-plane strain vector, $\epsilon_d = (\epsilon_1^2 + \epsilon_2^2)^{1/2}$, changes significantly with principle strain ratio, ρ. Samples tested in plane strain had the greatest roughening anisotropy while samples tested in balanced bi-axial tension had nearly no anisotropic roughening and roughened the same amount regardless of measurement orientation. Zhao et al. [25] suggest that part of the explanation is the relationship between the Taylor factors of neighbouring grains with respect to the tensile axis. The Taylor factor, M, is a measure of the ability of a particular grain orientation, or texture component, to accommodate plastic flow. The Cube orientation has the same Taylor factor when tested parallel and perpendicular to the rolling direction; $M_{Cube}^{RD} = M_{Cube}^{TD} = 2.45$. However, the Goss texture component exhibits a large plastic anisotropy, and its Taylor factor differs significantly with test orientation; $M_{Goss}^{RD} = 2.45$, $M_{Goss}^{TD} = 4.9$. When tested parallel to the rolling direction there is no difference in how the two texture components accommodate plastic flow, thus no roughness develops. When tested perpendicular to the rolling direction, there is a significant different in how each grain accommodates plastic flow. The Cube orientated grains develop slip bands on their surface and tend to depress forming valleys. The Goss orientated grains tend not to develop slip bands and form ridges instead [17, 20, 25], resulting in the development of long range correlated surface roughness.

2.6 Effect of Grain Size

The proportional relationship between the average grain size and the resulting deformation roughness is well documented: as the grain size increases, the magnitude of the roughness also increases [7, 9, 10]. Figure 2.6 illustrates the relationships of thickness and grain size. The roughness value, cited as the average maximum height of the profile, R_{tm}, for 70-30 brass sheet subjected to equibiaxial stretching is not appreciably different between sheets 0.5mm and 1.0mm thick. However, as the average grain size increases from 35μm to 235μm, the rate of roughening with respect to strain increases [7]. Kawai et al. [10] conclude that the average roughness is approximately proportional to the average grain size for a thickness to average grain size ratio greater than three, leading to the conclusion that the surface roughness is influenced by a subsurface layer two to three grains thick. A study on the affect of grain size distribution has not yet been systematically conducted.

Fukuda et al.[7, 8]) proposed the following equation relating roughening to the average grain size, d_o and effective strain, $\bar{\varepsilon}$:

$$R' \simeq K d_o \bar{\varepsilon} \tag{2.1}$$

where K is a materials constant depending on the slip characteristics, and $R' = R - R_o$; R_o is the initial roughness[7, 8]. This model was devised for sheets with large thickness to average grain size ratios deformed with a strain ratio from +1.0 to -1.0.

2.7 Effect of Crystallographic Texture

Within most of the previously mentioned studies, the effect of specific grains was also investigated. Multiple researchers conclude that the development of surface roughness is dependent on grain rotation of surface grains [4, 8, 11, 17, 19] Surface grains are not as constrained as other grains in the bulk material, which are surrounded by other grains. Grains on the surface can more easily rotate and deform since any part of the grain exposed to the free surface, for the most part, are not constrained [17, 18]. Following from this line of thought, the role of individual texture components as well as distribution of texture components have received a lot of interest. The effect of grain-to-grain, or neighbouring grain, interaction is a second area of interest and is covered in a subsequent section.

2.7.1 Brief Definition of Texture

There are several definitions of texture used in literature. For the purposes of this study, 'texture' is used to describe the orientation of individual grains with respect to the rolling direction of the sheet. Individual textures are denoted using several different conventions. A set of three angles (Euler or Bunge), or a plane-direction pair are two common naming conventions. There are several textures that have been given names by which they are commonly known, such as 'Cube' and 'Goss' textures [16]. This thesis will primarily use the plane-direction and name conventions to denote individual texture components. The plane-direction convention is similar to other orientation relationships used in crystallography, such as the Kurdjumov-Sachs relationship [15]. However, instead of citing parallel planes and directions between two grains, texture components are cited as having a plane and direction parallel to the rolling direction of the sheet. For example, the $\{011\}< 100 >$ texture component, also known as the 'Goss' texture component, is orientated in the sheet such that a plane from the $\{011\}$ family is parallel to the rolling direction, and one direction from the $< 100 >$ family of directions in that plane is also parallel to the rolling direction.

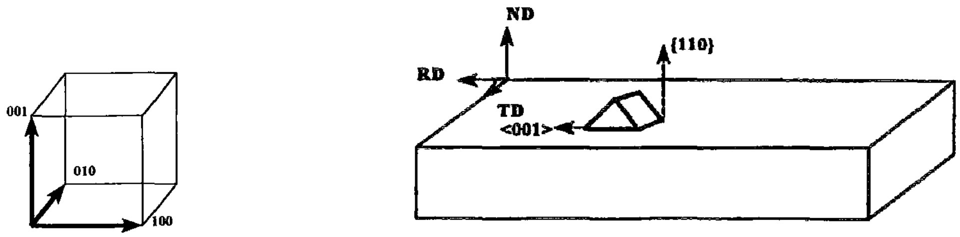

(a) Reference Cubic Crystal Coordinate System (b)

Figure 2.7: Schematic Illustration of the relationship between the crystal and sample axes for the Goss texture component. From [16]

Table 2.1: Texture Component List

Common Name	Plane-Direction	Common Name	Plane-Direction
Cube	{001} < 100 >	Goss	{011} < 100 >
R	{124} < 211 >	S	{123} < 634 >
P	{011} < 122 >	P*	{011} < 455 >
Q	{013} < 231 >	Cu	{112} < 111 >
X	{112} < 110 >	A	{001} < 130 >

Adapted from [19]

This is shown schematically in Figure 2.7.

There have been two principle relationships investigated between texture and the formation of surface roughness: distribution of texture components within the sheet and the effect of specific texture components. Research on these two topics will be outlined with respect to the two different length scales - mesoscopic or short range scale (orange peel), and macroscopic or long range scale (roping/ridging). Table 2.1 gives the common name and plane/direction pair for the individual texture components introduced in this section.

2.7.2 Effect of Texture on Mesoscopic Roughening/Short-Range Surface Features

Few studies have been conducted on the relationship between mesoscopic roughening and crystallographic texture. Wilson et al. [23] report that material with a strong texture (material with most of its grains with the same texture component) can have a lower magnitude of mesoscopic roughness due to the limited range of Taylor factors present within the grains of the sheet. They report that copper with a strong Cube texture (approximately 0.94 volume fraction) has a lower surface roughness with respect to strain . Baczynski et al. [14] conducted tensile tests parallel and perpendicular to the rolling direction on a AA6111 sample with exclusively Cube texture component and the resulting roughness only had mesoscopic type roughening , in agreement with Wilson et al. The experimental study conducted by Lee et al. [22] on AA6022-T4 material 1mm thick in plane strain with the rolling direction parallel to the tensile direction reported that there is no clear relationship between the crystallographic texture and the development of orange peel on the surface. However, grains with the brass orientation tended to be located in ridges/peaks while grains with either Cube or Copper orientation tended for be located in valleys.

The distribution of texture components as well as the specific components present have a significant effect on the development of the surface. A random arrangement of texture components were found to yield orange peel-type roughening while texture segregation has been linked to longer range surface features such as roping [14, 17, 19]. Using an FEM model developed to model the surface development of AA6111, Wu et al. [19] reassigned the existing texture components, where are initially banded, to give a uniform spatial distribution. The resulting surface morphology after simulated testing to a strain of 0.1 in uniaxial tension perpendicular to the rolling direction is distinctly isotropic, with no distinct ridges or valleys.

The effect of randomly orientated grains has been investigated by several researchers.

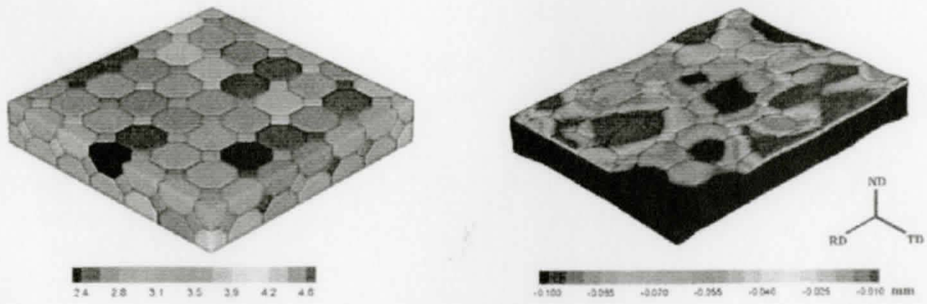

(a) Taylor Factor Mesh of Undeformed Surface

(b) Surface Profile after 20% stretching parallel to the rolling direction

Figure 2.8: Relationship between Developed Surface Roughness and Taylor Factor for a Random Distribution of Texture Components. From [25]

Becker [13] replaced the measured initial texture orientations with three separate sets of 77 random orientations into his 2D through-thickness FEM model and reported that the calculated average roughnesses for all three random orientation assignments do not differ, indicating that roughness is not dependant on the distribution of a random arrangement of texture components. For randomly arranged texture components, Zhao et al. [25] report no relationship between the Taylor factor and the resulting surface height displacement, or developed roughness. Their FEA model is based on Wigner-Seitz polyhedra unit cells to form a sheet of one equivalent 'grain' thick, and 6mm by 6mm in size. The resulting comparison between the Taylor factor for each grain and the surface profile, Figure 2.8 from simulations of uniaxial tension parallel to the rolling direction showed no direct relation between the Taylor factor for individual 'grains' and the developed surface roughness.

2.7.3 Effect on Macroscopic Roughening/Long-Range Surface Features

Considerable work has been done investigating the formation of roping/ridging, especially in aluminum alloys. The main area of interest is the effect texture, both different components and distribution, has on the development of surface morphology during deformation.

There is a general consensus that different texture components and texture component distribution are a significant factor in causing roping to occur [2, 14, 17, 19, 21, 23, 24, 25]. Early studies conducted by Wittridge and Knutsen [17] related the formation of ropes on the surface to the distribution of R-component texture, $\{124\}< 211 >$, colonies in a primarily Cube matrix. When tested perpendicular to the rolling direction, this sample developed a very distinct roped morphology. R-component is much harder and is very resistant to thinning in the normal direction. However, the Cube orientation has a lower strain hardening capacity, and thus undergoes slip and form 'valleys' upon deformation. This process leads to the morphology shown in Figure 2.9. Although there is continuing discussion and debate surrounding the process, this outlines the basic concept as to how textural 'banding' can cause a roped morphology upon straining. Baczynski et al. [14] reported that the spatial distribution of the Goss component was the main factor in the development of long range roughness. A banded structure of Cube and Goss grains formed ropes on the sample surface when tested perpendicular to the rolling direction.

Developed models have lead to a further understanding on the role of individual texture components as well as the affect of spatial arrangement of components on the resulting surface morphology. Beaudoin et al. [21] reported that valleys were populated by Cube orientated grains while grains in the ridges/peaks were of S orientation for FEM simulations based on backscatter Kikuchi diffraction patterns were run in biaxial stretching and near-plane-strain deformation. Wu et al. [19] developed an FEM model which utilized electron backscatter diffraction (EBSD) data. By removing specific texture components (Cube, Goss, R, X), they were able to determine how those components affected the development of roping. From the predicted surface profiles, the effect of those four components on roping is in the order X $\gg$ Cube $>$ Goss $>$ R. Simulations were also run when texture component pairs were removed. The removal of Cube-R and Cube-Goss pairs only yielded a slight change in the surface morphology. When Cube-X or Goss-X pairs were removed, the simulated roping tendency reduced significantly . Using the same model as above,

(a) R-component Colonies in a Cube matrix aligned parallel to the rolling direction

(b) Initial development of roughening upon deformation

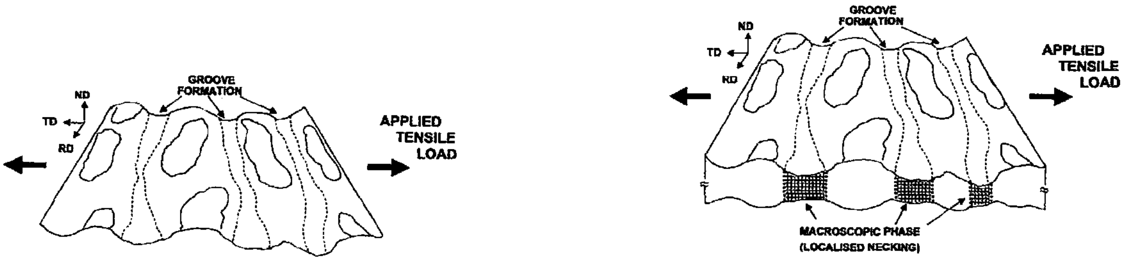

(c) Linking of Valleys to form continuous grooves

(d) Macroscopic phase leading to strain localization through the specimen thickness

Figure 2.9: Schematic Illustration of how Texture Bands can produce a Ribbed Morphology. From [17]

Wu and Lloyd [24] further investigated the affect P*, S, P, Q, Cu, and A as well as Cube, Goss, R, and X. These texture components are reported to only have a small effect on the surface roughness. The removal of Goss had the largest effect for a single component. Removing the combined texture components on the RD-rotated Cube fibre (the texture fibre encompassing the components from Cube to Goss) yielded the largest reduction in surface roughness. Wu and Lloyd conclude that the distribution of combinations of texture components is the controlling factor in roughening. Zhao et al.'s [25] model was developed to also investigate the reaction at the grain boundaries rather than use measured data as primary input. Three different strain states, uniaxial tension both parallel and perpendicular to the rolling direction and biaxial tension, were simulated with four different texture component combinations; Cube and Goss, Cube and Brass, Cube and Copper, and Cube and S, with a banded arrangement of texture components. This configuration forced a rope-like morphology to occur. Figure 2.10 shows the difference between the developed morphology within one texture combination as well as the difference between simulations done using one strain state and different texture component combinations. When tested parallel to the rolling direction, only a mild amount of roughening occurred in all combinations, with the Cube and Goss combination showing the least. Combinations of Cube and Goss, Cube and Brass, and Cube and S show a distinct increase in overall roughness as well as the development of a distinctly roped profile when tested perpendicular to the rolling direction. The magnitude of the resulting roughness is the highest after biaxial tension, with the Cube and Goss combination having the most banded morphology.

The effect increased tendency for certain components to shear, as opposed to slip, on roughening was also investigated. The S component is known to shear in the normal-transverse plane when deformed in the rolling-transverse plane [25]. Using the banded component model, Zhao et al. simulated a pair of two crystallographically equivalent S orientations common in rolled material; S1 and S2. Each S-type orientation had the same Taylor factor when tested parallel or perpendicular to the rolling direction. However, they

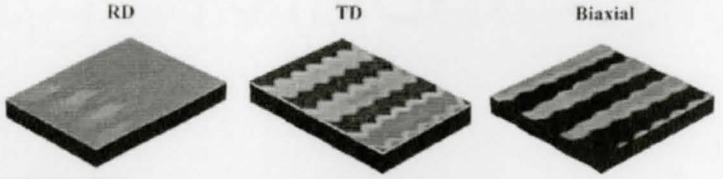

(a) Cube + Goss

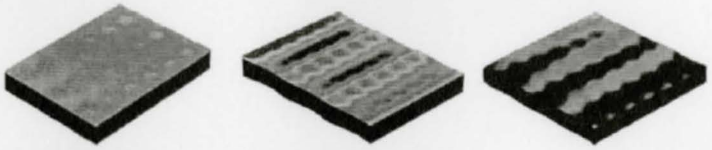

(b) Cube + Brass

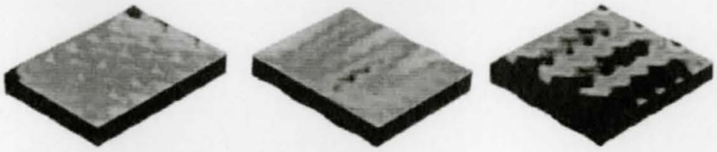

(c) Cube + Copper

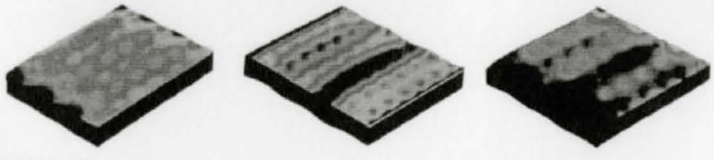

(d) Cube + S

Figure 2.10: Development of Ridging/Roping Profiles under Various Texture Component pairs and Sample Orientation. From [25]

exhibit the opposite shear tendency when stretched perpendicular to the rolling direction. Figure 2.11 shows the results from simulations run on three strain states. The overall roughening trends are similar to the Cube-S texture component pair as shown in Figure 2.10d: a diffuse banded structure when deformed parallel to the rolling direction 2.11(a), a strongly banded structure when deformed perpendicular to the rolling direction 2.11(b), and a distinctly banded morphology after biaxial tension 2.11(c). However, the ridges and valleys in Figure 2.10 are spread over the grain boundary while the 'border' between ridges and valley conform to the grain boundaries especially after testing perpendicular to the rolling direction in Figure 2.11, indicating that the shearing tendency of these orientations is the

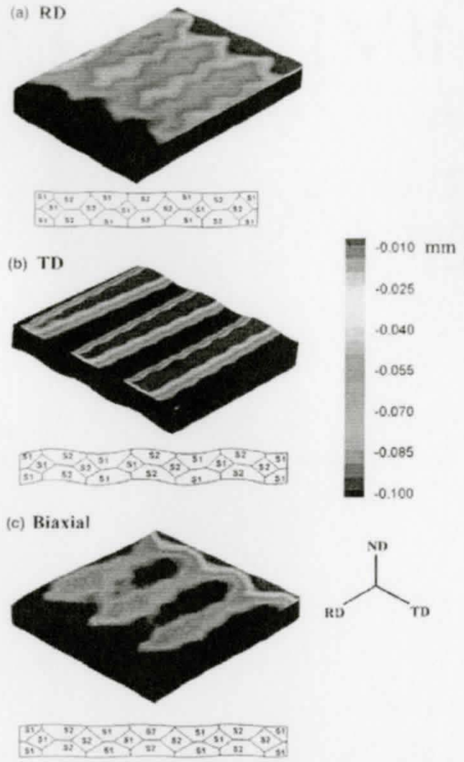

(a) Resulting Profiles due to Combining Two Equivalent, but Mechanically Different, texture orientations

Texture Component	Euler Angles		
	φ_1	ϕ	φ_2
S1	60^0	32^0	65^0
S2	300^0	148^0	245^0

(b) Shear Texture Component and Associated Euler Angles

Figure 2.11: Changes in the Roughness Profile with respect to strain direction and state. From [25]

cause of the resulting morphology [25].

2.7.4 Effect of Neighbouring Grain Interaction

Multiple studies have been conducted which report that there is a significant effect of neighbouring grains on each other.

Shimizu et al.'s [4] experimental study on polycrystalline iron revealed adjacent grains tended to have similar values of principle strain, indicating that neighbouring grains may be subject to mutual restriction during deformation. This effect can be seen through the work of Tong et al. [6]. Their study used AFM measurements taken across two grains, one of Cube orientation and the other with a random texture orientation (R3), with increasing strain revealed the inhomogeneous deformation within the Cube grain. It appears that the plastic response within the Cube grain in very inhomogeneous. Not only does this grain rotate out of plane, but it appears to change its shape from initially having a flat profile to an increase in height of the centre portion of the grain while the regions close to the grain boundaries seem to depress at higher strains. This is not the case in grain R3, whose profile remains essentially flat and just rotates out of plane. There seems to be two effects occurring at once: the cube grain is deforming in response to the imposed macroscopic strain and is rising from the surface but is constrained by the shared grain boundary with the randomly orientated grain, and the section of the shared grain boundary is being 'pulled up' which causes the randomly orientated grain to start to rotate out of plane. A similar reaction seems to be occurring on the other side of the Cube grain along its grain boundary with the Copper-orientated grain to its left. In this case, the region of the Cube grain close to this grain boundary seems to be constrained. It is not stated which process may be the primary mechanism for this effect.

Choi et al. [20] examined 6022-T4 aluminum sheet 0.825mm thick deformed in plane-strain tension both parallel and perpendicular to the rolling direction up to a strain of 24%. They report very visible slip lines in some of the grains in samples tested in either orientation, and that not all surface grains produced slip lines. Some grains remained smooth at higher strains (up to 24%). Furthermore, grains that exhibited slip lines were depressed into valleys while those without slip lines existed in hills (commonly called 'peaks'). They conclude that the plastic response of the surface grains, which exist with partially relaxed deformation geometry, is highly dependant on the activities of individual slip systems which can be altered by the plastic interaction with neighbouring grains. If a grain produces slip bands and is situated next to a grain that does not exhibit the same deformation characteristics and retains an unslip banded surface, it is likely that the un-slip banded neighbour will rotate or undergo grain boundary sliding to maintain grain compatibility. Also, a texture study confirmed that grains exhibiting slip bands which depress and those that appear without slip bands can have the same texture. There was also a relationship between the tensile/rolling direction and the spatial arrangement of grains with and without slip lines. Samples tested perpendicular to the rolling direction exhibited an interaction between grains with and without slip lines that produces hills and valleys that are linearly organized and span from 1 to 3 grains, as shown in Figure 2.12. Choi et al. conclude that the primary source of mesoscale roughening in this materials was the plastic interaction between neighbouring grains. Beaudoin et al. [21] investigated ridging in AA6111-T4 aluminum sheet using a 2D FEM model to examine the formation of roughness on the surface under strains up to 18%. Their simulations indicated that grains of the same or very similar texture orientation will form the same type of surface feature - either a peak/ridge or a valley depending if the grains elevate or depress respectively. They further state that the behaviour of individual grains differs from what is expected based on the average macroscale strain due to neighbouring grain interactions. Simulations run placing the sheet in plane strain exhibited grains of Cube orientation both deforming readily and becoming part of a valley, and being very stable forming into a peak. The conclusion drawn is that the neighbour interactions play a significant role in the deformation behaviour of surface grains [21]. As previously stated, Zhao et al.'s [25] investigation included a comparison between the Taylor factor and the resulting deformation surface roughness. As shown in Figure 2.8, the 'grains' deviate from expected behaviour based on their Taylor factor, indicating that the Taylor factor itself is not sufficient to predict the behaviour of grains on the surface of a metal. Grain interaction is given as one important factor in determining the development of surface roughness [21, 25].

Thus far only the interaction between surface grains has been outlined. The same principle applies to subsurface layers of grains. Lee et al. [22] report that the first three to four layers interact with the surface grain, and these subsurface grains collectively can greatly affect the resulting behaviour of the surface grain. The resulting roughening behaviour is affected to a greater degree by the grains surrounding the surface grain rather than the

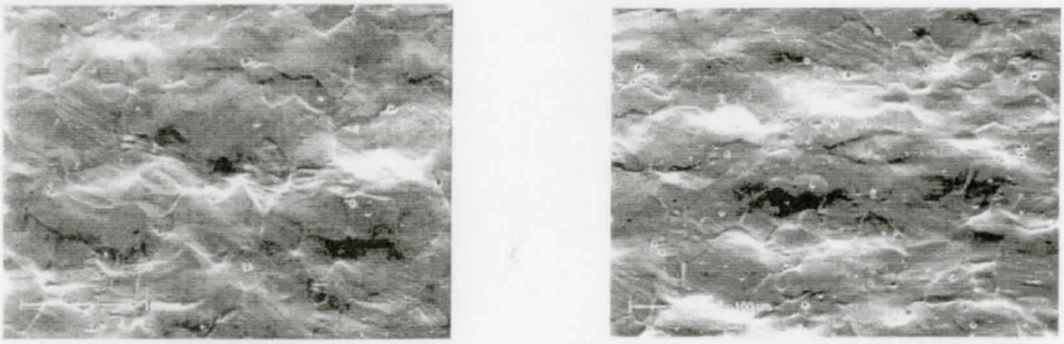

(a) Tested Parallel to Rolling Direction to 23% strain

(b) Tested Perpendicular to Rolling Direction to 24% strain

Figure 2.12: SEM micrographs of meso-scale roughening by plastic interaction between slip-banded and nonslip-banded grains (Tensile Axis: Top to Bottom). From [20]

surface grain itself. Wu and Lloyd [24] report that roughening is affected by the plastic response of interior grains, not only dependent upon the response of surface grains. As such, their simulated roughness calculated by their model could be significantly underestimated since the specific effect of the interior grains is not taken into account.

2.8 Recent Work on Effect of Strain Hardening Rate

Modeling work by a number of authors suggests a relationship between the strain hardening rate and the development of the free surface of a metal subject to deformation. Becker [13] reports that any factor affecting the plastic response of the sheet, such as strain hardening, crystallographic texture, and material homogeneity, should also affect the surface. Modeling work done suggested that a decrease in the strain hardening rate should increase the amount of roughness on the surface of the sheet [24] although a change in strain hardening rate has a negligible effect on the development of roping [19].

Chapter 3

Experimental Methods

3.1 Materials

The material used in this study was a direct-chill (DC) cast AA6111 aluminum alloy supplied by Alcan International, Kingston Research and Development Centre in Kingston, Ontario. The composition of the alloy is given as 0.67wt% silicon, 0.70wt% copper, 0.68wt% magnesium, 0.35wt% iron with the remaining material being aluminum. The material was supplied as rolled annealed sheet 2mm thick cut into sections approximately 23cm wide by 1.2m long.

3.2 Samples for Tensile Testing

Tensile samples were machined in two sizes. One set of tensile samples had a gauge section 9mm wide with a 35mm gauge length. Experiments using samples of this size include those tested at different temperatures and those tested with different temper treatments. The second set of tensile samples had a gauge section 9mm wide with a 25mm gauge length.

Experiments on samples with an intermediate polish used the shorter tensile specimens. Schematics of both samples sizes are shown in Figure 3.1. To investigate the effect of the orientation relationship between the rolling direction and tensile direction on surface development, both sample sizes were machined both parallel and perpendicular to the rolling direction, as shown in Figure 3.2.

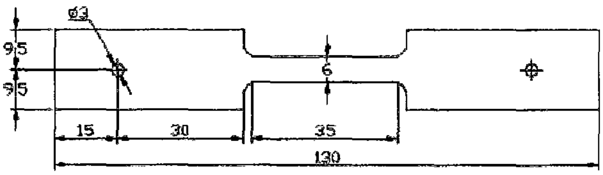

(a) 35mm gauge length

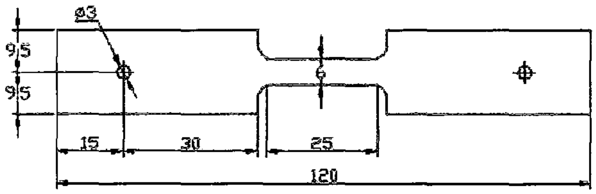

(b) 25mm gauge length

Figure 3.1: Schematic diagrams of samples used for mechanical testing. All dimensions in millimeters.

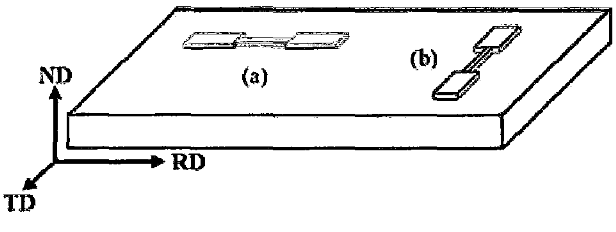

Figure 3.2: Diagram of samples cut (a) parallel and (b) perpendicular to the rolling direction.

3.3 Grain Size Measurements

Grain size measurements were done on three T4 samples; two samples analyzed in the rolling/transverse plane, and one sample used for analysis of the rolling/normal and transverse/normal planes. The samples were polished to a $1\mu m$ diamond finish and etched using Keller's Reagent. The samples were etched by gently swabbing the polished surface with Keller's Reagent for 60 seconds. They were then thoroughly rinsed in warm water and soaked in a 50% nitric acid solution for 15 seconds. Samples were then rinsed and dried. Keller's Reagent contains 2.5% nitric acid, 1.5% hydrochloric acid, and 1.0% hydrofluoric acid by in water. The grain size was measured according to ASTM standard E112 using the mean linear intercept method.

3.4 Heat Treatment and Sample Preparation

After machining, samples were solutionized at 560^0C for 20 minutes then immediately water quenched. All subsequent heat treatments were done immediately after quenching. T4 samples were naturally aged for at least 13 days. Artificially peak aged samples, T6, were immediately aged at 180^0C for 8 hours. Over-aged samples, designated as OA, were immediately aged at 250^0C for one hour. The main objective of this study is to determine if the development of surface roughness with increasing strain is significantly affected by changes in strength and strain hardening rate. A consistent initial surface was necessary to ensure any resultant topographical development was not a product of different initial surfaces. All samples were manually mechanically ground using 1200, 2400 and 4000 grit silicon carbide (SiC) paper sequentially and were thoroughly rinsed between papers. Samples for the temperature tests were given a quick 1 micron diamond polish before tensile testing. This polish did not completely remove the scratches from the 4000 SiC grit paper polish, but did visibly reduce the severity of the scratches. Initial roughness measurements from 5 samples confirmed a consistent surface. Samples with different temper treatments and the sample set which included samples with an intermediate polish were electropolished after manual grinding. The grip sections of the samples were masked off using Lacomit^{TM} varnish and let dry for at least one hour in a fume hood before electropolishing. The electrolyte used was a solution of 1.5% nitric acid, 4.5% perchloric acid in methanol. A 750ml solution was mixed per batch of electropolishing. The samples were electropolished at 20-30 volts for 7-10 seconds at a starting temperature of 10^0C. During electropolishing, the temperature of the electrolyte could increase by as much as 5^0C, giving an overall electropolishing temperature between 10 and 15^0C. During this procedure, the electrolyte was cooled using a methanol/ice bath. Each electrolyte mixture could only be used to electropolish between 8 and 10 samples before becoming contaminated. Attempts to electropolish further samples resulted in the development of irregular pits and a distinct film on the surface of the sample. Severely pitted samples could not be used as there was no region to measure the deformed surface without also having an etch pit present. After electropolishing, the samples were rinsed in methanol then air-dried. The electropolishing apparatus is shown in Figure 3.3.

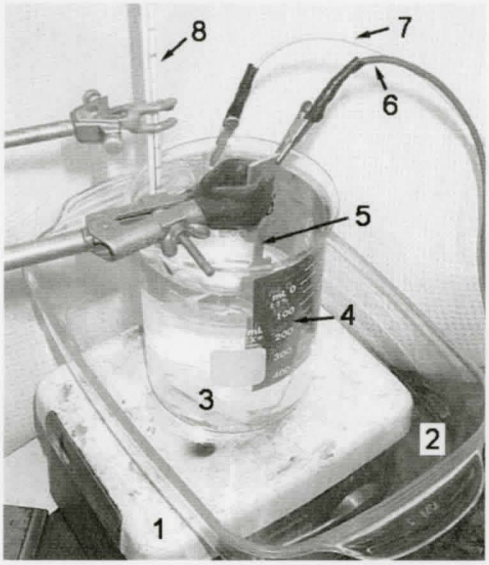

1	Hot Plate/Stir Base
2	Methanol/Ice Bath
3	Stir Rod
4	Austenitic Stainless Steel electrode
5	Aluminum Sample
6	To + of power supply - Anode
7	To - of power supply - Cathode
8	Thermometer

Figure 3.3: Electropolishing Apparatus.

3.5 Mechanical Testing

Each test condition tested samples machined both parallel and perpendicular to the rolling direction. Individual samples were deformed to various true strains up to and including fracture. The surface roughness was then measured. Samples were tested using either a hydraulic MTS tensile testing machine with a 100kN load cell or a screw driven Instron tensile testing machine with a 10kN load cell. Extension was measured using two different clip-on extensometers. The extensometer used with the hydraulic system has a gauge length of 12.7mm and the one used with the screw driven system has a gauge length of 12.5mm. All tests were conducted at a constant cross head speed of 0.75 mm/min, which resulted in a bulk strain rate of $1 \mathrm{X} 10^{-3}$ /s for both tensile machines.

To ensure the differing stiffness between the hydraulic machine and the screw driven machine could be disregarded as a possible source for differing mechanical responses and potential differences in surface development, room temperature samples were tested using the hydraulic system both parallel and perpendicular to the rolling direction. The true stress-strain curves for room temperature samples tested parallel to the rolling direction gathered using the screw driven system and the hydraulic system are shown in Figure 3.4. In the plastic region, the true stress required for the same true strain is within 2%. Both curves appear smooth, with no visible serrations, indicating that this material is not subject to the Portevin-Le Chatelier effect. Both curves being essentially the same indicates that the difference in stiffness between the two testing systems used does not greatly affect the mechanical response of the samples tested parallel to the rolling direction. Tests conducted on samples perpendicular to the rolling direction showed similar results. The mechanical response does not significantly change with respect to tensile machine used. Data gathered using the hydraulic system can be directly compared to data gathered from the screw driven system.

The following paragraphs outline the specific mechanical testing procedure for samples tested at different temperatures, with different temper treatments, and the sample set which

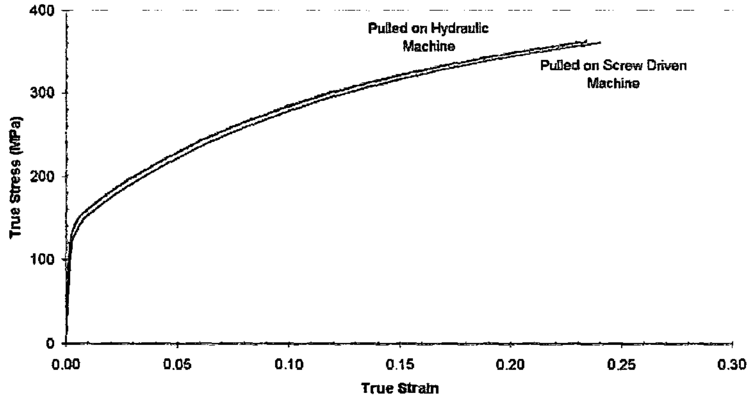

Figure 3.4: T4 295K samples Tested to fracture using Both Tensile Machines plotted to UTS.

includes an intermediate polishing step respectively.

Samples tested at different temperatures were T4 samples. The specific test temperatures were 295K, 212K, and 77K. To attain the lower testing temperatures, samples were immersed in a low temperature bath during mechanical testing. Samples tested at 212K were immersed in a dry ice/ethanol bath. The temperature of the dry ice/ethanol bath was monitored using a low temperature thermometer. Samples tested at 77K were immersed in liquid nitrogen. In both cases, the temperature of the sample was assumed to be the same as the bath. Samples for each test temperature were deformed to 5%, 10%, 15%, and 20% true strain as well as to fracture. Samples tested at 77K were also deformed to 25% true strain and one sample tested perpendicular to the rolling direction was deformed to 30% true strain. Testing on some of the samples tested at low temperatures was stopped prematurely to adjust the extensometer. The sample remained immersed in the cooling media while the effective gauge distance of the extensometer was adjusted. The test was resumed immediately afterwards. This interruption resulted in a stress spike after reloading, indicating that there had been some relaxation during this process. All room temperature samples were tested using the screw driven tensile system and all low temperature samples were tested using the hydraulic tensile system.

Tensile tests on samples with different temper treatments, T4, T6, and OA, were done at room temperature (295K). Samples from each temper condition were pulled to fracture. T4 samples were pulled to true strains of 5%, 15% and 20%. T6 samples were pulled to 5%, 10%, and 15% true strain. OA samples were pulled to 5%, 8%, and 10% true strain. All samples were tested using the screw driven machine.

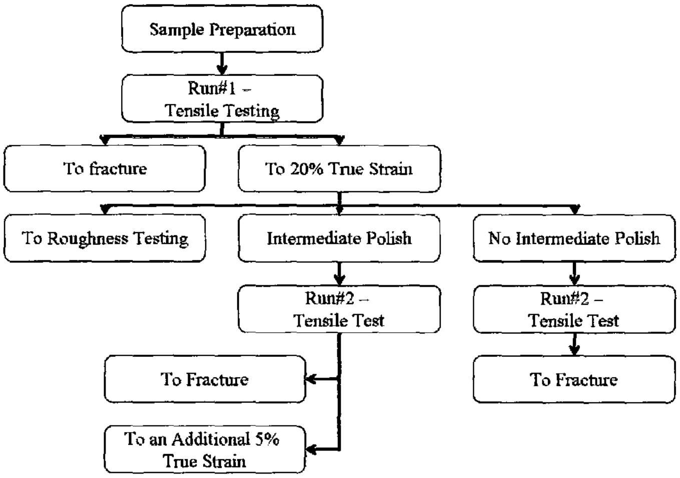

Figure 3.5: Testing Steps for Experimental run including samples with an Intermediate Polishing Step

Experiments which included an intermediate polishing step were done on samples in the T4 condition tested at room temperature. Samples were deformed into the plastic region, testing was stopped and the sample was repolished before testing resumed. The testing procedure used for these experiments had three parts; initial tensile testing designated as Run #1, the intermediate polishing step, and the second tensile test designated as Run #2. Ten samples of each orientation were prepared for this. During Run #1, one sample each was tested to fracture parallel and perpendicular to the rolling direction. The rest of the samples were pulled to 20% true strain and unloaded. One sample of each orientation was used for surface roughness measurements. During the intermediate polishing step, the samples were polished using the same procedure as their initial preparation. Two samples of each orientation were given an intermediate polish. Run #2 commenced 48 hours after Run #1. During Run #2, one polished sample and one unpolished sample were pulled to fracture for each orientation. At least one polished sample per orientation was tested to an additional 5% true strain. All samples were tested using the hydraulic tensile system. The flow chart shown in Figure 3.5 outlines the preparation procedures for experiments involving an intermediate polishing step.

3.5.1 Calculation of Strain Hardening Data

The strain hardening rate is calculated using Origin 6.1. Calculated true stress-strain data from tensile testing is used. The calculated data is copied and pasted into a new project in Origin. The data is plotted and extrapolated to 500 points. It is then smoothed using the Savitzky-Golay filter with a polynomial factor of 2 and a smoothing value of 10 to 20 points. The true stress is differentiated with respect to the strain to give $\frac{d\sigma_t}{d\varepsilon_t}$, or the true strain hardening rate. The strain hardening rate is plotted with respect to both true stress and true strain. It is plotted with respect to true stress to determine the differences in the strain hardening rate between test conditions. Plots of strain hardening rate versus true strain are included to serve as a comparison to other parameters also compared to true stain, such as roughness data.

3.5.2 Calculation of Strain Hardening Parameters

Stain hardening data is often quoted in terms of materials constants to accompany the curves calculated in Section 3.5.1. It was assumed that the following hardening model can be used for this material:

$$\sigma_t = K\varepsilon_t^n \tag{3.1}$$

where σ_t and ε_t is the true stress and strain respectively, n is the strain hardening exponent, and K is the strength coefficient.

To determine the values of n and K for a specific test condition, the calculated true stress-strain data is plotted on a log-log scale using Microsoft Excel. Data between the 0.2% offset yield stress and the true stress at the maximum load is used for this calculation. Calculation of K and n-values should be done over data after the material has become completely plastic. In this material, there is a large elastic to plastic transition region. There is still a mixture of elastic/plastic behaviour after the calculated 0.2% offset value. However, the offset yield stress and corresponding true strain was chosen as a lower bound value to give a consistent reference point between samples tested under different conditions. A linear trend line was applied to each data set. The equation of the linear fit line as well as the R^2 value was calculated. The slope of the fit line is taken as the n-value. The K value is then calculated using the graphically derived value for n. The R^2 value, also known as the coefficient of determination, is a measure of how closely the trend line fits the individual data points. Values of R^2 greater than 0.95 resulting from regression analysis are considered to show a good fit between the experimental data and the linear trend line.

3.5.3 Calculation of Necking True Stresses and Strains

The true stress and strain for the onset of diffuse necking are calculated using the Considére's criterion:

$$\frac{d\sigma_t}{d\varepsilon_t} = \sigma_t \tag{3.2}$$

Local necking, or localized instability, in uniaxial tension can be described by the condition [26]:

$$\frac{d\sigma_t}{d\varepsilon_t} = \frac{\sigma_t}{2} \tag{3.3}$$

3.6 Surface Analysis

A surface includes both the relatively short range and the longer range wavelength roughness. There are a wide variety of parameters used to quantify a surface, as well as numerous techniques for collecting the data. The following two sections address the issues relevant to each topic. The first discusses the measurement techniques used to quantify the surface. The second subsection discusses the parameters which are used why these are preferred.

3.6.1 Surface Analysis Techniques

The surface roughness was measured using three systems: the Alpha-Step 200 stylus-type profilometer, the WYKO NT2000 Optical non-contact profilometer, and the Solarius Laser-Scan non-contact system with a LT8010 confocal sensor.

The Alpha-Step 200 Profilometer

The Alpha-Step 200 system measures the sample surface using single line traces. The average roughness value associated with the line trace in automatically calculated. A sample of a typical Alpha-Step trace on a sample tested to 15% true strain parallel to the rolling direction at 212K is shown in Figure 3.6. The stylus is diamond tipped with a diameter of 12.5μm. The scan speed was set to 7.5 μm/s and records 400 data points per line trace. For this study, line traces are set at 1 cm in length. Samples are manually aligned. The surface profile is measured by drawing the stylus across the sample surface and recording its vertical movements. These movements are translated into the line profile representing surface features along the trace line.

There are several limitations involved with using a stylus instrument. The curvature of the stylus tip can lead to certain features being masked out. If the stylus is wider than a surface feature, the feature will be glossed over, leading to a reduced magnitude measure-

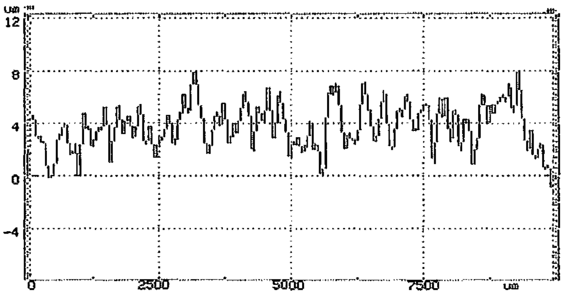

Figure 3.6: Line trace generated by the Alpha-Step system.

ment of valleys. If the surface's features are too steep, anomalous readings can be caused due to the stylus not being able to easily climb over the feature. Since analysis is based on a single trace, there is the possibility the trace can miss pertinent surface features. The trace reading can also be altered by surface contamination. Both these factors can lead to an inaccurate depiction of the overall surface if only one trace is used. Multiple measurements are required to gain an accurate representation of the surface. The internal software of the system has the ability to level the profile to correct for tilted samples. Two points are selected and the measured profile is adjusted so that the two selected points are the same height. Leveling is done automatically between the first and last point measured after the trace is complete. Leveling can be adjusted manually as necessary. It is possible that surface features maybe artificially altered if leveling is not done correctly. Care must be taken to ensure that only sample tilt is adjusted for.

On each sample tested within the uniform strain region, the centre and each quarter along the width was marked using a permanent marker with a 0.5mm tip. Traces were started at the mark, and measured along the gauge length of the sample parallel to the tensile axis. Three traces were done per side of each measured sample, giving a total of 6 line traces per sample. The system provides a print out of the line trace and calculates the average roughness. The average roughness for each test condition at strain is taken as the average of the average roughness values for each individual line trace for one sample. The error associated with the averaged average roughness is taken as the standard deviation between the individual line traces. The standard deviation of the measured average roughness values for a given sample was calculated using:

$$STD = \sqrt{\frac{\sum_{i=1}^{m}(x_i - \bar{x})^2}{m}} \tag{3.4}$$

where x_i is the average roughness for reading i, $\bar{x}$ is the average of all average roughness values and m is the sample size, in this case the total number of readings per sample.

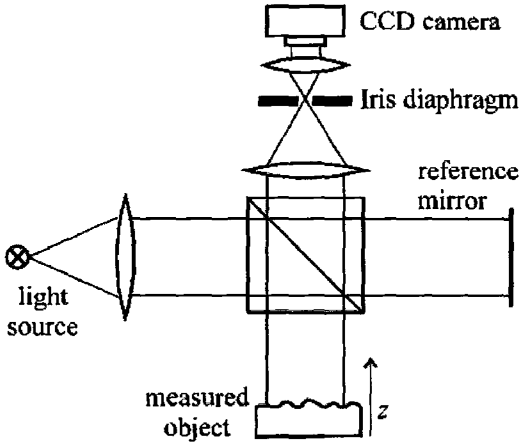

Figure 3.7: Schematic of a basic white light interferometry set-up [31]

The WYKO NT2000 Non-Contact Profilometer

WYKO NT2000 non-contact system uses white light interferometry to scan a section of the sample's surface. A schematic of the set-up for the basics of white light interferometry is shown in Figure 3.7. White light interferometry uses the interference pattern between a white light beam and the beam reflected from the sample surface through a specified height range to generate a topographical map of the scanned surface area. A variety of surface roughness parameters can be calculated for this region. A sample contour plot taken on a sample used in this study is shown in Figure 3.8. Although the WYKO system captures more of the surface than the Alpha-Step system, the same principles apply - if a feature

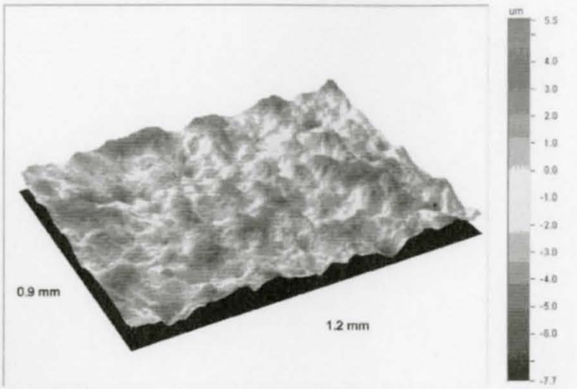

Figure 3.8: Contour plot generated from data gathered from by the WYKO system, in greyscale, from a sample pulled to 15% true strain parallel to the rolling direction at 212K.

occurs over a length scale larger than the scan area, the WYKO system could misrepresent the feature by only capturing a section of it, or not capture it at all. In areas where there is a steep slope between data points, such as when a high peak is next to a low valley, interferometry data is subject to drop-off. Drop-off is a result of the lack of an interference fringe resulting from no light being reflected from the steep slope. When no interference fringes are generated, no data is recorded for that region. During data post processing, the data can be filled in using the Data Restore function in the accompanying software. Data Restore calculates the value of the missing data pixels by interpolating between the adjacent pixels. Whether the data restore function can be used depends on the specifics of the surface being measured. This function can only be applied if the resulting surface data and parameters are not appreciably changed. If the surface being measured requires a highly accurate height resolution, on the order of nanometers, the error associated with using the Data Restore function is very large as compared to the surface profile. In this case, Data Restore introduces features to the data that are not part of the surface and so cannot be used. If the roughness is very large, on the order of microns, then added error from the restore is very small as compared to the overall surface topography and the resulting restored data does not significantly change the data. However, if there is a significant amount of data drop-off, using Data Restore can artificially alter the roughness parameters, and possibly create surface features not actually present. Care must be taken to ensure the restored data is an accurate representation of the sample surface. This is done by comparing it to the initial scan.

A median filter is then used to smooth the data, removing any sharp spikes due to noise. The number of pixels referenced around the specific point to be smoothed is adjustable. For this study a 5 by 5 median filter is used. Figure 3.9 illustrates how data measured from a T6 sample tested perpendicular to the rolling direction to 15% true strain changes after Data Restore and a median filter is applied to illustrate the differences these analysis techniques impart between the raw data and the processed data.

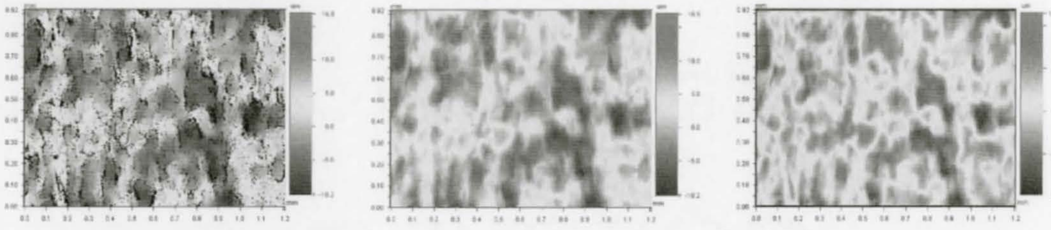

(a) Raw Data

(b) After Data Restore

(c) After Data Restore and Median Filter of 5

Figure 3.9: WYKO Data changes due to post processing.

For this study, the WYKO system scan size was set to a 0.9 by 1.2mm area. Samples are manually aligned. The samples measured with the Alpha-Step system are the same measured using the WYKO system. Two measurements were taken per side with the WYKO system for samples tested in the uniform strain region. Both Data Restore and a median filter with a value of 5 were used to process the raw data from each scan. Values measured on the same sample were averaged and the standard deviation between these measurements was calculated using Eqn 3.4 to calculate the surface parameter values for each sample.

For samples tested to fracture, three distances starting at the fracture tip were scanned to measure the roughness in a high strain region. The necked region of the fracture sample was first marked off using a permanent marker with a 0.5mm tip 1mm, 2mm and 3mm from the fracture edge. One measurement was done per mark along the centre of the sample.

The LaserScan system with LT8018 Confocal Sensor

The LaserScan system by Solarius with a LT8010 confocal sensor was used to scan larger surface regions. The LaserScan system uses the same premise as the Alpha-Step system; it utilizes line traces to quantify the surface. However, the LaserScan system has the ability to stitch together multiple line traces to generate a topographic map of the sample surface. The LaserScan system is a non-contact profilometer utilizing a laser with a wavelength of 670nm and a spot size of 2μm to measure line traces on the sample surface. The sensor array vibrates through a vertical range of $\pm 300\mu$m at a frequency of 1400 Hz. The vertical resolution of the system is 0.1μm. The stage moves the sample at a rate of 2mm/s in the x-direction to take a line trace. Sampling was done every 5μm in the x-direction. After every x-direction trace, the stage was moved 15μm in the y-direction.

As the array vibrates, it detects the height of a surface feature in relation to the height of the sensor. When the reflected light is in focus, it passes through the detector pinhole to the detector, as shown in Figure 3.10, which notes the vertical position of the sensor. Once the line trace is complete, the stage returns to its starting x position, moves the sample predetermined distance in the y direction, and begins another line trace. By measuring and combining parallel line traces, the system can generate a topographical surface map for a given region.

The overall scan area used in this study was 5mm across the width of the sample (y-direction) and 8mm along the tensile axis (x-direction). 1600 height measurements were taken over the 8mm trace distance. Over the 5mm scan width, 333 lines traces were taken. Combined, approximately 533 333 height measurements were taken per sample. From these measurements the software generates a 2D surface map where the height is indicated on a colour scale. A surface map measured on a sample tested at 212K parallel to the

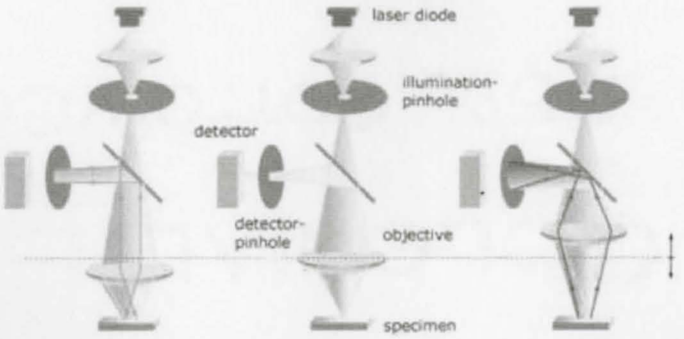

Figure 3.10: A schematic set-up of the LT8010 confocal sensor in the LaserScan system by Solarius. From [32]

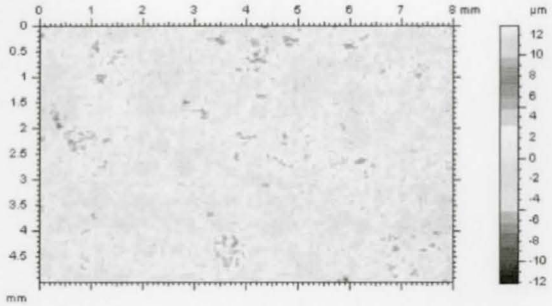

Figure 3.11: An example of a LaserScan Surface Map; in greyscale.

rolling direction to 15% true strain converted to a greyscale image is shown in Figure 3.11. Samples tested at different temperatures deformed to 15% true strain, samples tested after different temper treatments deformed to 5% true strain as well as tested to the highest true strain before the onset of necking, full strain series (5%, 15%, and 20% true strain) for temper T4, and samples for the intermediate polish experiments tested to 20% true strain after Run #1 as well as those deformed to a further 5% true strain after an intermediate polish were scanned. One scan was done per sample.

3.6.2 Surface Roughness Parameters

There are a variety of parameters which may be used to quantify the surface roughness. In this study, two common parameters are used: average roughness, Ra, and the 10-point mean roughness, Rz.

The average roughness is defined as the arithmetic average of the height from the mean value over the entire profile for a given profile length. The height of any point in the sample surface profile shown in Figure 3.12 is given by f(x) for a distance x along the surface. The average roughness over a total length x = L is given by:

$$R_a = \frac{1}{L}\int_0^L |f(x)|dx \tag{3.5}$$

The average roughness gives a first approximation view of the sample surface.

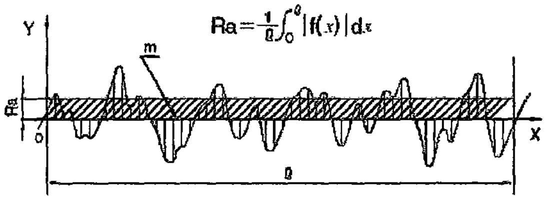

Figure 3.12: A schematic surface profile given by f(x) for a distance *l*. From [33]

Since an overall average of the profile is calculated, it is possible to have the same average roughness value for different surface morphologies, as shown in Figure 3.13.

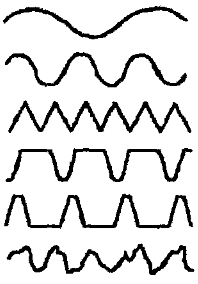

Figure 3.13: Line profiles with identical average roughness, Ra, values. From [34]

To further differentiate between surfaces, the ten-point mean roughness parameter, Rz, is used. The ten-point mean roughness gives a measure of the 'peakiness' of the surface. It is the average magnitude of the 5 greatest peak heights and 5 deepest valley depths, and is given by:

$$R_z = \frac{1}{5}\left[\sum_{i=1}^{5}|f^{peak}(x_i)| + \sum_{j=1}^{5}|f^{valley}(x_i)|\right] \tag{3.6}$$

A schematic of a profile with the ten-point mean roughness calculated is shown in Figure 3.14. In this diagram, Y designates the height from the median line, m, to the peak or valley. Ypi and Yvj are the magnitudes of the height of the ith peak or depth of the jth valley respectively.

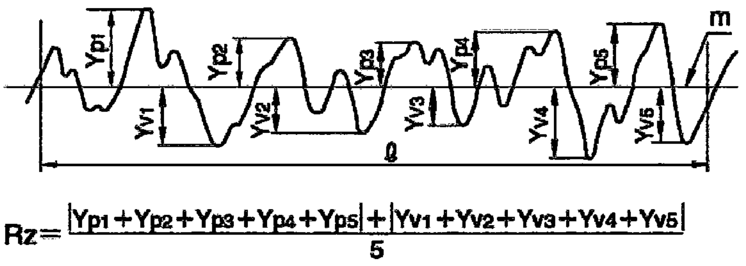

Figure 3.14: Schematic surface profile with 10-point mean roughness, Rz, value calculated. From [33]

Although an average roughness may be similar between surfaces, the spacing of the peaks and valleys as well as the height difference between adjacent peak-valley pairs can be very different. Using a parameter that measures these heights can further distinguish the differences between separate surface morphologies.

3.6.3 Spatial Analysis of LaserScan Surface Maps

Spatial analysis was done to measure the relationship between the average grain size and surface features present in the surface maps. For this study, a modified covariance function is used. The covariance function compares the similarity or dissimilarity between the values

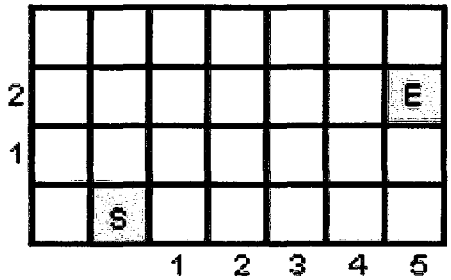

Figure 3.15: Relation between step size and pixel location in an image.

of two data points separated by given step size, and is given by:

$$G(n,m) = \frac{1}{XY}\sum_{i=1}^{X}\sum_{j=1}^{Y}\left(f(i,j)-\bar{f}\right)\left(f(i+n,j+m)-\bar{f}\right) \tag{3.7}$$

where $f(i,j)$ is the value of the height at coordinates i and j, $\bar{f}$ is the average height value calculated using all height values within the scan area, n and m are the step sizes in the i and j direction (or x,y directions) respectively, and X and Y are the lengths of the analyzed area in pixels in the x and y direction respectively. A data point given by $f(i+n,j+m)$ for a step size of (n,m) is defined as that data point the number of pixels away from the reference pixel in the specified direction. As illustrated in Figure 3.15, a reference cell $f(i,j)$ with an associated height value is shown shaded with an 'S'. If the height value in this cell is going to be compared to the height in a cell n = 5 and m = 2 step sizes away, the height of 'S' would be compared to the height of cell 'E' located at $(i+5,j+2)$.

All spatial analysis using the LaserScan surface maps had the i-direction, which is the same as the x-direction mentioned above, aligned with the tensile direction (length of 8mm). The analysis was further simplified by only comparing height values along the tensile axis. As such, only steps in i-direction were needed. The modified equation is:

$$G(n,m=0) = \frac{1}{XY}\sum_{i=1}^{X}\sum_{j=1}^{Y}\left(f(i,j)-\bar{f}\right)\left(f(i+n,j)-\bar{f}\right) \tag{3.8}$$

The surface map portions of the LaserScan data files were cut and copied into separate files using Adobe Photoshop 6.0. MatLab 13 was used to convert the .tif images into a matrix containing the height values for (i, j) locations on the surface. Each pixel in the original surface map has an associated height value that will be used as the input data for the covariance function. One step size is equal to one pixel.

Initial runs over the full 8mm by 5mm surface map were not feasible due to computational time constraints. The analyzed area was reduced to a 5mm by 4mm area, with the length parallel to the tensile axis being 5mm long. The equivalent distance on the surface for one step size is found by dividing the length scale of interested from the original surface map by the number of pixels required to illustrate that distance. For example, LaserScan surface maps of the samples tested at different temperatures contained 351 pixels along the tensile axis for a scan length of 8mm. The equivalent spatial measure along the tensile axis for one step size is 22.8μm per step size. The resulting covariance function value, $G(n, m = 0)$, is plotted against the distance between surface features. The relative value of $G(n, m = 0)$ with respect to a given distance gives an indication of how many point have similar height values and not what the specific height value is. If $G(n, m = 0)$ has a high value, most of the heights for that separation distance are very similar. For example, if a surface has a repeating series of ridges 1mm apart running perpendicular to the step direction, the relative covariance function value versus separation distance plot will show a large positive value for a separation distance of 1mm. A smaller 'bump' in the curve will result if only many of points have similar heights for the given separation distance. If a large negative value for $G(n, m = 0)$ results, the heights of a majority of the data point for a given separation distance have very different values (i.e. height values between peak/valley pairs). A 'dip' results if only many of the points have different values.

3.7 Optical Microscopy

3.7.1 Determination of Strains in Localized Flow Region

Localized flow strains (strains in the neck) were calculated for the regions with corresponding roughness data. The marks used to align the samples for roughness measurement in the WYKO system were used as reference marks for strain measurement. A series of digital pictures across the sample width and thickness were taken using a Zeiss Axioplan 2 universal light microscope. The images were stitched using Adobe Photoshop 6.0. Any colour correction was done at this time. Pertinent features in the composite images were measured using ImageTool 3.0.

Only one image was needed to capture the thickness of the samples, as shown in Figure 3.16. Three to four pictures were required to generate width images. Individual images were manually stitched using Adobe Photoshop 6.0. Images that fit together vertically were stitched first. The resulting columns of pictures were then stitched to their neighbouring column. The process was repeated until the overall image was complete. It is possible to have misalignments between individual pictures due to pixel mismatch. Pixel mismatch occurs when the pixels representing a feature on one picture do not completely align with the pixels of the same feature in the second picture. This effect can compound over several pictures, causing a change in the distance between features of the composite which is solely due to analysis. The maximum distance change over the 4 picture composite at 50X magnification due to mismatch is 0.01mm. The edges of some samples are difficult to directly define as the edge region spans up to a 4 by 4 pixel region. The error associated with measurements containing an edge is 0.04mm per edge. A typical image used to measure for the marked width in the necked region is shown as Figure 3.17. Both the thickness and width images were taken of a T4 sample tested at 295K parallel to the rolling direction.

The dimensions within the necked region can change rapidly over fairly small lengths. Five different measurements were taken over the width of the mark to account for the range

Figure 3.16: A typical composite image used to measure the thickness of a sample corresponding to regions where surface roughness measurements were taken.

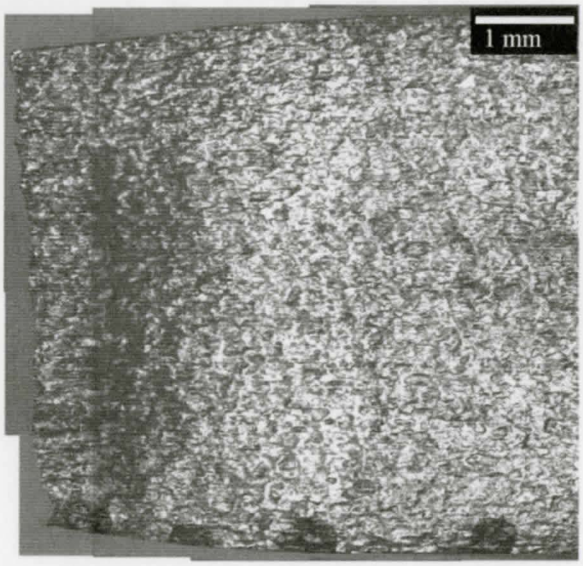

Figure 3.17: A typical composite image used to measure the width of a sample corresponding to regions where surface roughness measurements were taken.

of strain over which the roughness measurement was made. These values were averaged and the standard deviation of the set was calculated to get an length value for each mark. The average thickness and width of the sample for each mark is denoted as t_{mark} and w_{mark} respectively. The averages of the width and thickness measurements were used to determine the true strain at the mark using:

$$\varepsilon_{t,mark} = \ln\left(\frac{A_0}{t_{mark}w_{mark}}\right) \tag{3.9}$$

where A_0 is the original cross sectional area.

To calculate the error associated with a product of two values each with its own error as given by:

$$\alpha \pm \Delta\alpha = (\beta \pm \Delta\beta)\,(\gamma \pm \Delta\gamma)\,, \tag{3.10}$$

the following formula is used:

$$\Delta\alpha = (\beta\gamma)\sqrt{\left(\frac{\Delta\beta}{\beta}\right)^2 + \left(\frac{\Delta\gamma}{\gamma}\right)^2} \tag{3.11}$$

The total measurement error for the thickness distances is the standard deviation between the individual measurements for one mark plus 0.08mm for the edges, and the total for the width distances is the calculated standard deviation of the width measurement per mark plus 0.09mm for any pixel mismatch and for the edges. The total error in resulting strain measurement is calculated using:

$$\Delta A = (w_{mark})(t_{mark})\sqrt{\left(\frac{\Delta w_{mark}}{w_{mark}}\right)^2 + \left(\frac{\Delta t_{mark}}{t_{mark}}\right)^2} \tag{3.12}$$

$$\Delta\varepsilon_{mark} = \frac{\Delta A_{mark}}{A_{mark}} \tag{3.13}$$

where $\Delta\varepsilon_{mark}$ is the error in the true strain at the mark, ΔA_{mark} is the error associated with the cross sectional area at the mark, Δw_{mark} and Δt_{mark} are the errors in the width and thickness measurements respectively.

3.7.2 Composite Surface Images

Optical images of sample surfaces were compiled to gain a direct view of the surface. Several different optical images were taken of the same sample on several different magnifications. Pictures were taken at 25X magnification in an attempt to capture any long range effect that may be present. Although these images did show a relatively large area, the resulting image did not show a lot of detail. There was also some discrepancy with respect to observed features being a part of the surface or a result of analysis technique. On several samples, it appeared that pertinent surface features aligned the same way in viewing field regardless of the direction of the sample on the microscope stage. This was further investigated and discussed in the Results section. Samples viewed at higher magnifications were taken to gain a more definitive view of individual grain affects. Pictures taken at 50X and 100X were stitched together to form composite images at these higher magnifications respectively. Adobe Photoshop 6.0 was used to organize and stitch together pictures using the same procedure outlined in the previous section.

3.8 Reduction of Area Measurements

The reduction of area, RA, at final fracture was calculated using images of the fracture surface taken with a scanning electron microscope (SEM). Samples were mounted so they could be viewed normal to the tensile axis. At least two images were taken per sample. Figure 3.18 shows a typical image used for RA measurements. The fracture area was measured using ImageTool 3.0 image analysis software. The averaged RA values of the individual measured areas were used as the overall RA measurement. The area was measured by manually outlining the whole fracture surface. The edge was denoted at the region where the fracture surface met the sample side. This region was not well defined on all sides of the sample in the SEM images, and measured approximately 4 to 5 pixels wide for each edge of each image. Based on the width of the undefined edge area, the overall error associated with the fracture area due to the lack of edge definition was calculated to be 0.16mm.

The true stress and strain at fracture is calculated using the average value for RA using:

$$\sigma_{fracture} = \frac{F_{fracture}}{RA} \tag{3.14}$$

$$\varepsilon_{fracture} = \ln\left(\frac{A_0}{RA}\right) \tag{3.15}$$

where $F_{fracture}$ is the recorded force at fracture.

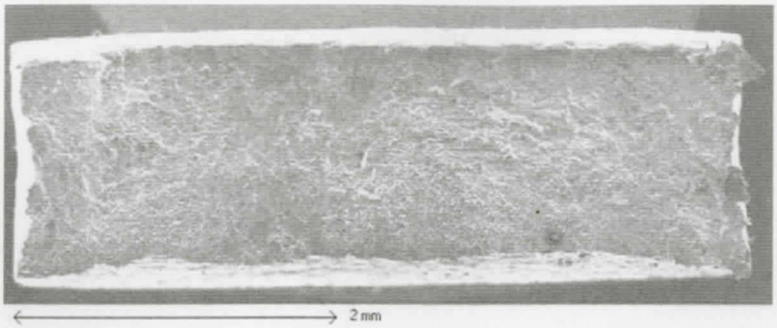

Figure 3.18: Typical image used for reduction of area measurements. This sample was pulled at 212K perpendicular to the rolling direction.

The error for the true fracture stress and strain is calculated using:

$$\Delta\sigma_{fracture} = \sigma_{fracture}\left(\frac{\Delta RA}{RA}\right) \tag{3.16}$$

$$\Delta\varepsilon_{fracture} = \frac{\Delta RA}{RA} \tag{3.17}$$

Chapter 4

Experimental Results

The role of strain hardening rate, strength and orientation on the development of roughness on unconstrained surfaces in AA6111 sheet aluminum was investigated. The development of surface features due to deformation, commonly known as surface roughness, were measured as a function of strain. Two orientations were tested by machining samples with the sheet's rolling direction parallel and perpendicular to the tensile axis. A series of T4 samples were tested at three different temperatures to determine the affect of different strain hardening rates.

AA6111 is a heat treatable alloy, forming precipitates whose size, shape and distribution is dependent on the specific temper treatment. Different temper treatments alter the strength of the material. Samples with one of three different temper treatments were tested at room temperature, 295K. The temper treatments investigated are naturally aged (T4), artificially peak aged (T6), and overaged (OA). A T6 treatment of DC-AA6111 typically has both β" and Q' type precipitates [27]. Samples artificially aged at 250^0C for 30 minutes also show both β" and Q' type precipitates. However, these precipitates are significantly coarser than those formed during the T6 temper treatment [27]. Overaged samples using during this study were treated at 250^0C for 1 hour to allow for precipitate coarsening.

A third experimental set was conducted on T4 samples tested at 295K with an intermediate polishing step done after 20% true strain to determine if surface roughening was dependent upon deformation history.

The surfaces of deformed samples in all studies were measured in terms of two well defined surface parameters, the average roughness (Ra) and the ten-point mean roughness (Rz). The topography of a larger section of the surface was measured using both LaserScan surface maps and optical microscopy. This study was conducted to investigate changes in the development of surface features with respect to length scale, grain size and shape.

This section begins with the characterization of the DC-AA6111 aluminum alloy used in this study. The results from experiments conducted on sample with different strain hardening rates due to testing at different temperatures and samples with different strengths due to different temper treatments as well as an experimental set with an intermediate polishing step are presented. A summary of results will be given at the end.

4.1 Grain Size Measurements

Grain size measurements were done on the rolling / transverse direction plane, rolling / normal direction plane and the transverse / normal direction plane. Measuring the grain size in these planes will give an approximation of the grain size and shape in three dimensions.

Grain size measurements in the rolling/tranverse plane were done using two polished and etched T4 samples; one of each orientation. The grain size both parallel and perpendicular to the rolling direction was measured on each sample. A total of 26 lines were used, 13 in each orientation. The measured grain sizes for each orientation were averaged and their standard deviation was calculated using Eqn 3.4. On the sample surface, the average grain size parallel to the rolling direction is 92 μm and 82 μm perpendicular to the rolling direction. The overall average for both direction was 87.1 μm with a standard deviation of 9.5 μm. The grain sizes range from 66.2 to 108.8 μm overall. Although the standard deviation for the overall average encompasses the averages measured in both orientations, more of the grains are slightly elongated parallel to the rolling direction.

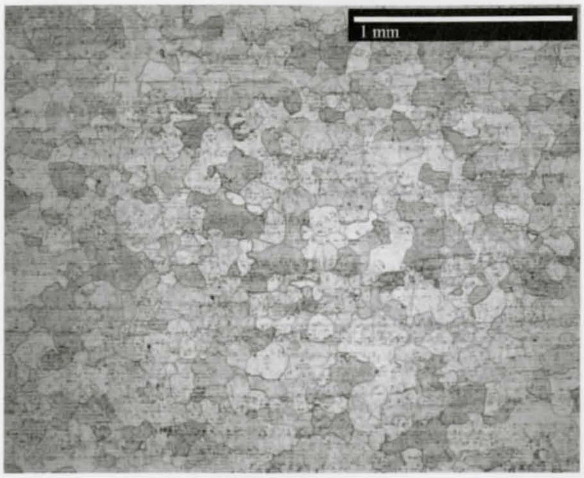

Figure 4.1: Representative Image used for Grain Size Analysis (Rolling direction is left to right)

Grain size measurements on the rolling/normal and transverse/normal plane were done on a different undeformed T4 sample. Measurement in the rolling/normal direction used total of 36 lines, 16 parallel to the transverse direction and 16 parallel to the normal direction. The resulting grain sizes are 65.9μm parallel to the rolling direction and 27.4μm parallel to the normal direction. The average grain size parallel to the transverse direction in the transverse/normal planes is 58.1μm and 27.5μ parallel to the normal direction. A total of 24 lines were used, 12 in either direction for grain size measurements on the transverse/normal plane.

In measurements taken through the thickness of the sample (i.e. in planes including the normal direction), the grains are elongated in the rolling and transverse directions with respect to the normal direction with an aspect ratio of 2.4 and 2.1 respectively.

The averages for each grain size measurement is summarize in Table 4.1.

This material also has visible stringers of inclusions/precipitates aligned parallel to the rolling direction. The stringer lines range in size, from distinct rows of precipitates that run the length of the viewed field, to shorter rows of precipitates. The distance between stringer rows is approximately 145μm and is shown in Figure 4.1.

Table 4.1: Grain Sizes with respect to Orientation (all measurements in μm)

Measurement Plane	Orientation	Average
Rolling/Transverse Plane	‖ RD	92.0 ± 6.5
	‖ TD	82.2 ± 9.5
	Overall	87.1 ± 9.5
Rolling/Normal Plane	‖ RD	65.9 ± 7.4
	‖ ND	27.4 ± 1.6
Transverse/Normal Plane	‖ TD	58.1 ± 4.7
	‖ ND	27.5 ± 2.4

4.2 EBSD Data

A limited EBSD study was done on an undeformed electropolished T6 samples cut parallel to the rolling direction. An 983 by 773 μm area was scanned using a step size of 3 μm. The scan area spanned approximately 19 grains parallel to and 17 grains perpendicular to the rolling direction. The resulting inverse pole figure map and inverse pole figure are shown in Figure 4.2. The texture distribution of the grains measured are mainly in the area close to the [001]-[111] boundary.

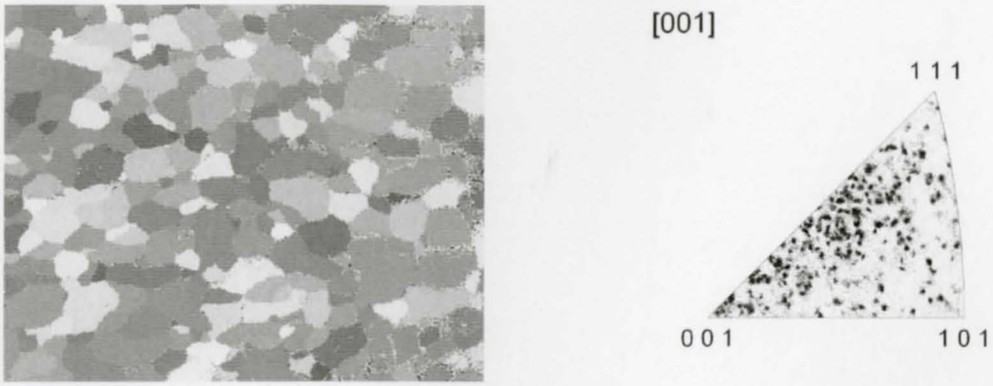

(a) Inverse Pole Figure Map (Grey Scale Represents Different Textures)

(b) Inverse Pole Figure

Figure 4.2: EBSD Results for an undeformed T6 sample cut parallel to the rolling direction.

4.3 Experiments Conducted at Various Strain Hardening Rates

To fulfill a major objective of this study, determining how changes in strain hardening rate affect the development of surface roughness, a series of T4 samples were tested both parallel and perpendicular to the rolling direction in uniaxial tension to different values of true strain up to and including fracture for three different test temperatures; 295K, 212K and 77K.

True stress-strain curves calculated from these tensile tests were used to quantify the mechanical properties. Surface parameters were measured from each test condition using the WYKO and Alpha-Step systems. The surface morphology of each condition was measured using LaserScan surface maps and composite optical microscopy images.

4.3.1 Mechanical Testing Results

For each combination of test temperature and orientation at least six samples were tested. The resulting true tensile curves from the samples within one testing condition show varying degrees of scatter in the strength with respect to true strain. The greatest difference between individual true tensile curves of the same test condition occur when samples are tested at lower temperatures. The maximum difference in the strength for an equivalent true strain in the plastic region is 6%. The tensile curves for samples tested at 295K show the greatest similarity in strength with respect to true strain. Regardless of test orientation, the difference in the strength with is below 3%. Figure 4.3 compares the set of tensile curves for samples tested at 295K and 212K perpendicular to the rolling direction. Tensile results for 8 and 9 samples respectively tested to various true strains are shown per Figure. Samples tested to failure are plotted up to their ultimate tensile strength. Notice the greater spread in the strength with respect to strain for samples tested at 212K as compared to those tested at 295K.

Three samples with the same testing conditions were pulled to fracture with the exception of samples tested parallel to the rolling direction at 295K where only two samples were tested to fracture. There is noticeable scatter in the fracture stress and strain within each test condition. Figure 4.4 show two test conditions illustrating a large and small range of true tensile curves to fracture for samples tested at 295K parallel to and at 77K perpendicular to the rolling direction respectively.

The difference in the fracture measurements are within measurement error for samples tested at 212K parallel to the rolling direction and at 295K and 77K perpendicular to the rolling direction. Samples tested at 295K and 77K parallel to the rolling direction and at 212K perpendicular to the rolling direction show significant difference in both the fracture true stress and strain. These difference can be due to the nature of the RA measurement itself, as previously discussed. The nature of the primary fracture mechanism at each temperature is another possible source of the differences between samples within one testing temperature.

A brief fractography study was done on samples tested to fracture at all three temperatures and two orientations. Fractography images taken using the SEM show a combination of microvoid coalescence (MVC) and shear-type failure at all temperatures. The fracture surface of samples tested at 295K and 212K at both orientations appear similar. All four surfaces show very distinct and extensive voids, associated with MVC. Damage formation and accumulation in DC-AA6111 T4 material was investigated by Gimple, and results for samples tested at 295K here show no significant difference when compared to his work on low-iron content T4 AA6111 [30]. The approximate area of the flatter regions, associated with shear-type failure, is the same between these four test conditions. Individual voids are also present in a majority of these flatter shear-type regions.

There is a significant increase in the amount of shear-type failure on the fracture surface of both samples tested at 77K. No voids are present within the shear-regions on the fracture surfaces of both samples tested at 77K.

To obtain a value for the fracture true stress and strain for each testing condition, the values for the fracture true stress and strain within each test condition are averaged and the standard deviation of the error for each sample combined using Equation 3.4. A comparison of the full true stress-strain curves from each test temperature with respect to orientation is shown in Figure 4.5. Due to limitation in the extensometer's travel distance, tests conducted at 77K and many conducted at 212K required interrupting to adjust the extensometer as described in Section 3.5 before testing is resumed. Examples are clearly visible on the tensile curves as a distinct jump in Figure 4.5.

Mechanical properties for all test conditions are shown in Tables 4.2 and 4.3. As expected, as the test temperature decreases, the yield stress increases. The yield stress did not change appreciably with respect to orientation in this material.

Within each set of temperature testing conditions there is minimal difference between the calculated strain hardening rate curves with respect to strain between samples. Sample

Table 4.2: Yield Stress and Necking Values for all Temperature Samples

Test Temperature	Orientation	0.2% Yield Stress (MPa)	Diffuse Necking		Local Necking	
			Stress (MPa)	Strain (in %)	Stress (MPa)	Strain (in %)
295K	$\parallel$ RD	132.7± 3.2	358.7 ± 1.5	23.4 ± 0.6	363.9 ± ···	25.1 ± ···
	$\perp$ RD	133.8 ± 4.3	358.3 ± 2.2	23.1 ± 0.9	363.8 ± 1.4	25.2 ± 1.2
212K	$\parallel$ RD	144.7 ± 8.2	381.9 ± 2.6	23.5 ± 0.1	389.6 ± 4.9	25.8 ± 0.4
	$\perp$ RD	144.0 ± 4.3	383.3 ± 5.4	23.7 ± 0.9	392.9 ± 1.7	25.8 ± 0.5
77K	$\parallel$ RD	182.4 ± 3.2	539.1 ± 1.3	30.9 ± 0.0	··· ± ···	··· ± ···
	$\perp$ RD	186.8 ± 4.5	535.3 ± 1.3	30.6 ± 0.1	556.2 ± 2.0	35.3 ± 0.8

Table 4.3: Calculated Fracture and Strain Hardening Parameters for Temperature Samples

Test Temperature	Orientation	Calculated Fracture		Strain Hardening Parameters		
		Stress (MPa)	Strain (in %)	n-values	K values	R^2 value
295K	$\parallel$ RD	474.3 ± 18.2	70.7 ± 3.7	0.278 ± 0.006	611.3 ± 85.3	0.989
	$\perp$ RD	432.8 ± 19.0	62.6 ± 4.3	0.274 ± 0.001	544.1 ± 7.92	0.988
212K	$\parallel$ RD	500.7 ± 42.3	63.8 ± 8.7	0.276 ± 0.001	577.1 ± 19.7	0.979
	$\perp$ RD	486.1 ± 23.4	64.8 ± 4.8	0.280 ± 0.002	634.5 ± 28.6	0.980
77K	$\parallel$ RD	653.3 ± 25.8	55.7 ± 3.9	0.327 ± 0.004	1859 ± 163	0.972
	$\perp$ RD	626.5 ± 40.8	53.9 ± 6.6	0.316 ± 0.002	1460 ± 79.3	0.972

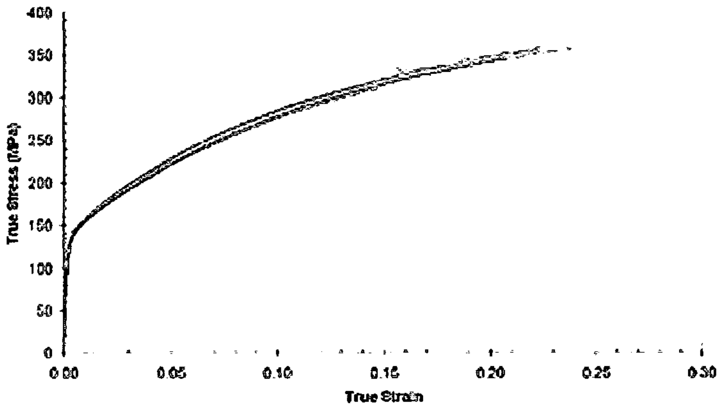

(a) Tested at 295K perpendicular to the rolling direction; similar curves

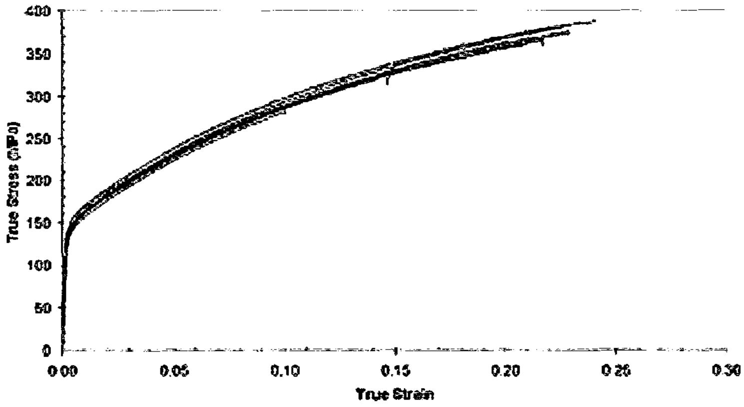

(b) Tested at 212K perpendicular to the rolling direction; greater degree of scatter

Figure 4.3: All tensile curves for select temperature sample sets.

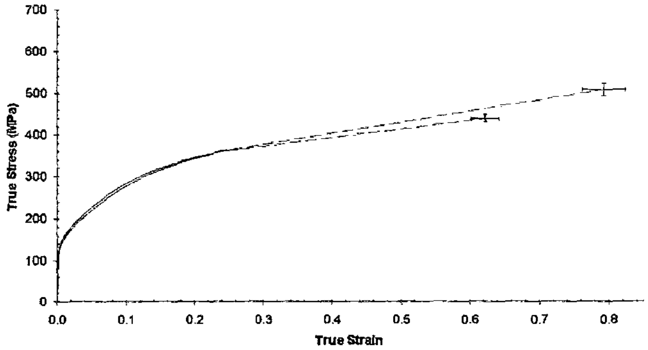

(a) Samples tested at 295K parallel to the rolling direction - Greatly differing fracture statistics between samples

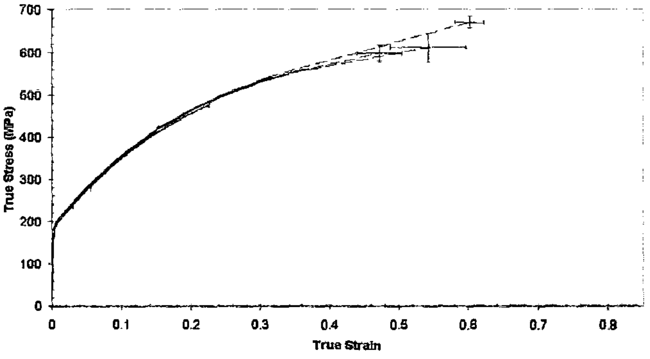

(b) Samples tested at 77K perpendicular to the rolling direction - Close fracture statistics between samples

Figure 4.4: Samples tested to fracture illustrating the possible range of fracture stresses and strains for samples tested at different temperatures.

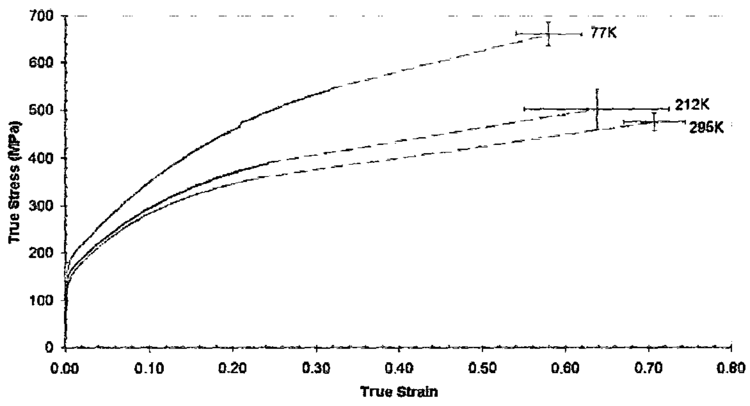

(a) Tested parallel to the rolling direction

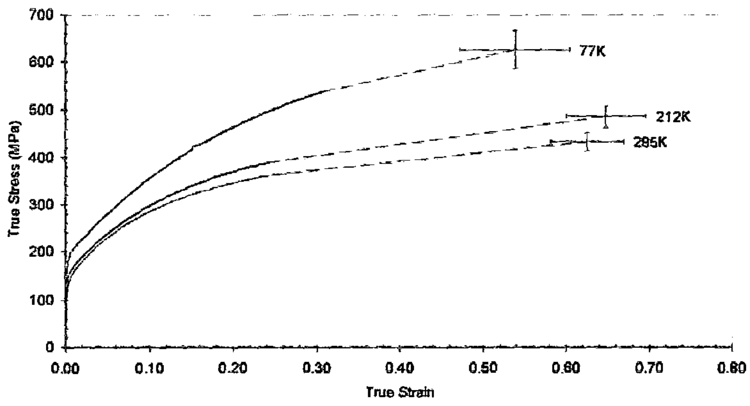

(b) Tested perpendicular to the rolling direction

Figure 4.5: Samples tested to Fracture For all Test Temperatures.

strain hardening curves for samples tested at 212K perpendicular to the rolling direction are shown in Figure 4.6 with respect to strain. Strain hardening calculations in regions very close to the strain value where it was necessary to interrupt the test to adjust the extensometer produce a section of extraneous data when differentiated. This is a result of data analysis and not representative of a material response. As such, data in this region is replaced with a dashed line, as seen in Figure 4.7. Figure 4.7 compare the strain hardening rate for each test orientation with respect to true stress.

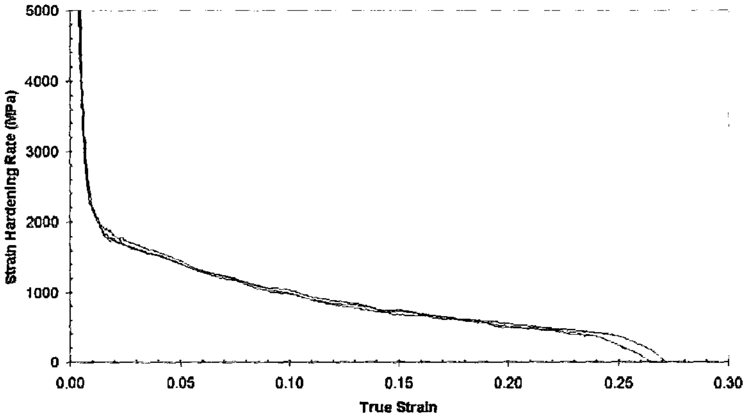

Figure 4.6: Strain Hardening Curves for Series Set tested at 212K perpendicular to the rolling direction

Samples tested at 295K and 212K have very similar strain hardening rates. However, samples tested at 212K have a slightly higher strain hardening rate. Samples tested at 77K have a noticeably higher strain hardening rate. The strain hardening rate for a given test temperature are the same regardless of orientation.

It is typical to display strain hardening data with respect to stress. In this study, many relationships, including those involving roughening parameters, are stated with respect to strain. As a comparison to other parameters shown with respect to strain, Figure 4.8 shows the strain hardening rate for each test temperature plotted with respect to strain.

Strain hardening parameters for samples tested at all three temperatures and both orientations are shown in Table 4.3. The n-value for samples tested perpendicular and parallel to the rolling direction at 295K are very similar, ranging from 0.274 and 0.278. The n-values of samples tested at 77K are approximately 0.05 higher. K values for samples tested at 295K and 212K are similar. Values for K range from 2.72 to 2.75 for samples tested at 295K and 212K. For samples tested at 77K, the K parameter was slightly higher at 2.88 for both orientations.

The lowest calculated R^2 value is 0.972. There was an overall good fit between the trendline used to calculate the strain hardening parameters and the raw data.

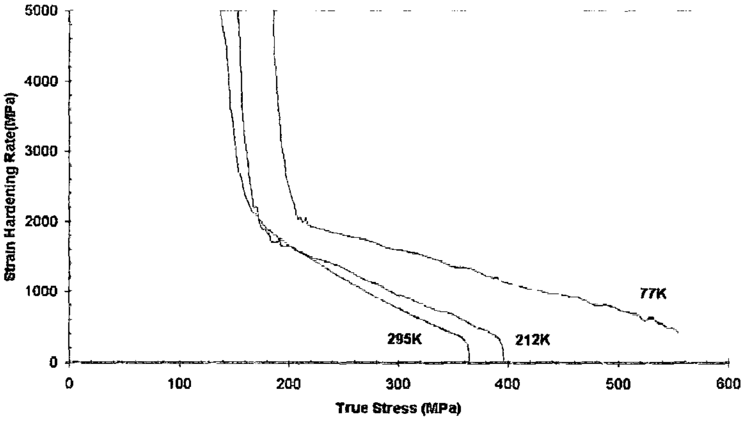

(a) Tested parallel to the rolling direction

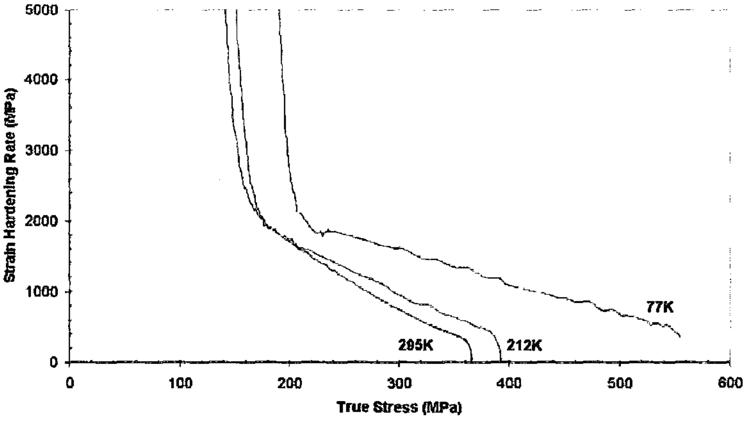

(b) Tested perpendicular to the Rolling Direction

Figure 4.7: Strain Hardening Curves versus True Stress for Samples tested at all temperatures with respect to orientation

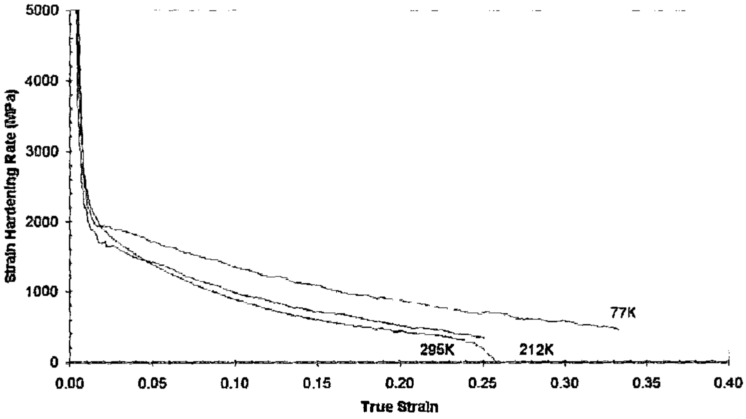

(a) Tested parallel to the rolling direction

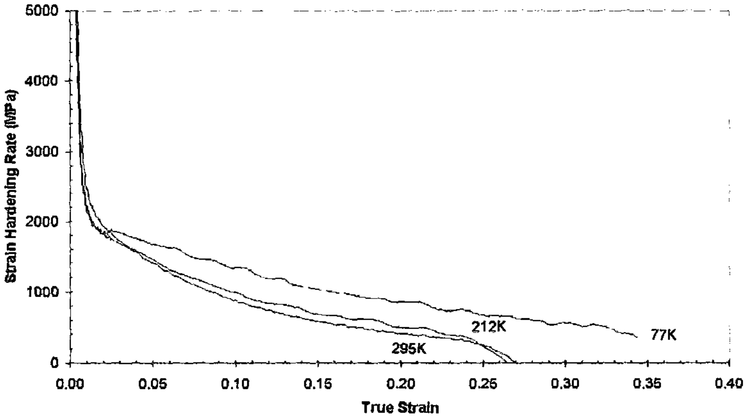

(b) Tested perpendicular to the Rolling Direction

Figure 4.8: Strain Hardening Curves versus True Strain for Samples tested at all temperatures with respect to orientation

4.3.2 Surface Parameters

The two surface parameters used to describe the surface are the average roughness, Ra, and the ten-point mean roughness, Rz. Two different measurement systems, the Alpha step system and the WYKO system, were used to gather Ra and Rz data.

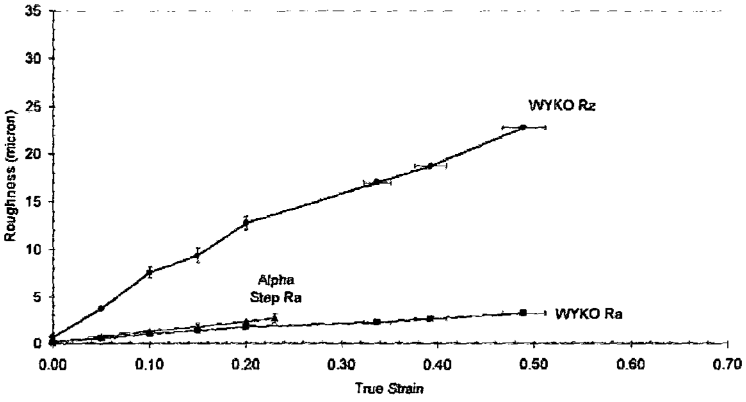

(a) Samples tested at 295K parallel to the rolling direction

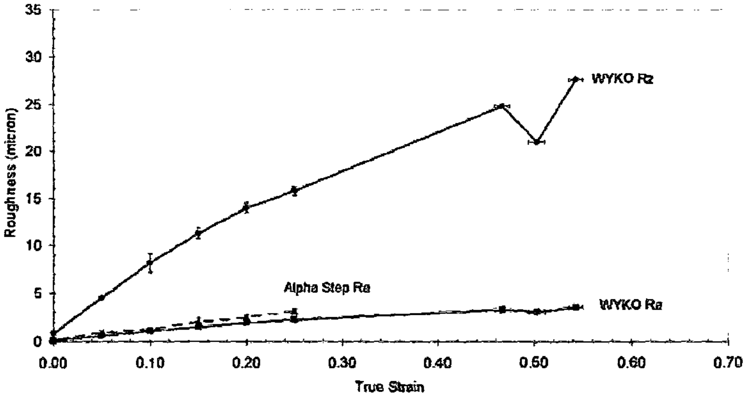

(b) Samples tested at 77K perpendicular to the rolling direction

Figure 4.9: All Roughness data for two sets of samples tested at different temperatures and orientations.

Roughness parameters generated using both measurement systems are shown for two representative test temperature and orientations. Samples tested at 295K parallel to the rolling direction and samples tested at 77K perpendicular to the rolling direction are shown in Figure 4.9. For all test conditions both roughness parameters are approximately linear with increasing true strain. Deviations from linearity are discussed with the respective parameter. The ten-point mean roughness increases quicker than the average roughness with respect to strain regardless of test temperature or orientation. This indicates an increase in the magnitude of the peaks and valleys as the sample is deformed. The average roughness values measured by the Alpha-Step and WYKO systems prior to localization are within error at all strains.

Only one roughness measurement was taken in the necked region per true strain measurement. It is possible this reading may not be representative of the surface in general at that strain, as shown in Figure 4.9(b). It is possible this is mainly due to either a random surface effect or sample curvature which can alter the calculated surface roughness parameters.

Figure 4.10 compares the average roughness values measured from samples tested at the three test temperatures by the WYKO system with respect to orientation. Up to the onset of localization, the rate of average roughening is essentially the same regardless of temperature. After the sample has started to locally neck, there is a greater degree of difference between the roughening rate of each test temperature with respect to strain. Samples tested perpendicular to the rolling direction show a greater difference between the post-necking roughening rate with respect to strain than those tested parallel to the rolling direction. The samples tested at 295K and 77K perpendicular to the rolling direction retain the same post-necking roughening rate while the roughening rate of the sample tested at 212K decreases.

The average roughening rate does not vary greatly between samples tested parallel and perpendicular to the rolling direction with respect to strain at the same temperature as shown in Figure 4.11. Samples tested at 295K and 77K roughen at the same rate regardless of orientation. Samples tested at 212K have the same pre-necking roughening rate. There appears to be a significant difference in the post-necking roughening rate between samples tested parallel to and perpendicular to the rolling direction. The sample tested parallel to the rolling direction has a higher post-necking roughening rate than the sample tested perpendicular to the rolling direction.

The ten-point mean roughness for each test temperature with respect to orientation shows the same relationships between samples tested at different temperatures as the average roughness trends. In all test conditions, the ten-point mean surface roughness increases linearly with strain. Before the onset of localized necking, the roughening rate with respect to strain does not differ with test temperature or test orientation. The post-necking ten-point mean roughening rate for samples tested at 295K and 77K do not differ. However, samples tested at 212K show some dependence on test orientation. The sample tested parallel to the rolling direction has a higher post-necking roughening rate than the sample tested perpendicular to the rolling direction.

4.3.3 Surface Morphology

Composite optical images and LaserScan surface maps are the two techniques used to measure the surface morphology.

LaserScan Results

Surface maps measured using the LaserScan system of samples tested to 15% true strain for both test orientations are shown in Figure 4.12. The scale indicates the vertical height in microns. For all surface maps, the height scale range was set for a range of 24 μm.

All surface maps show clusters with the same height ranging in size and shape. For samples tested parallel to the rolling direction, these clusters appear to be slightly elongated parallel to the rolling direction in samples tested at 295K and 212K. The valleys, visible as blue regions, on the surface also appear to align parallel to the rolling direction. The sample tested at 77K does not appear to show the same trend. The cluster sizes appear

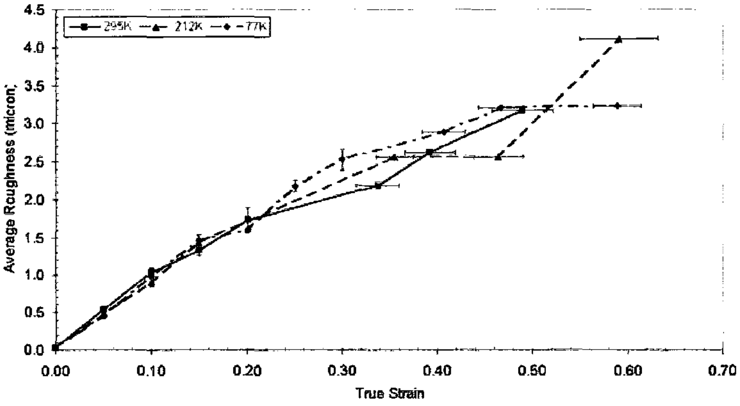

(a) Tested parallel to the rolling direction

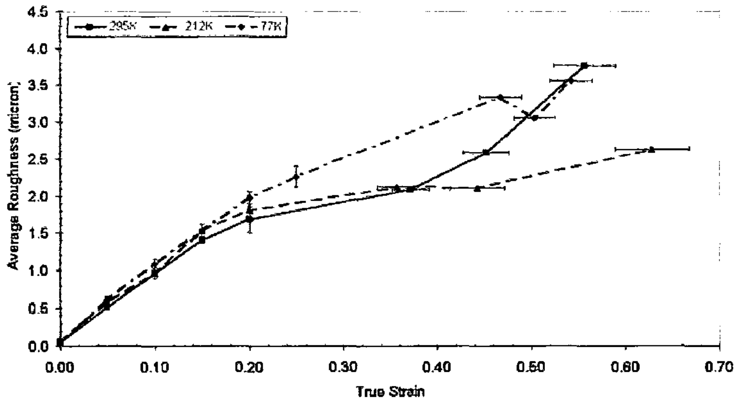

(b) Tested perpendicular to the rolling direction

Figure 4.10: The Average Roughness measured using the WYKO system for all samples.

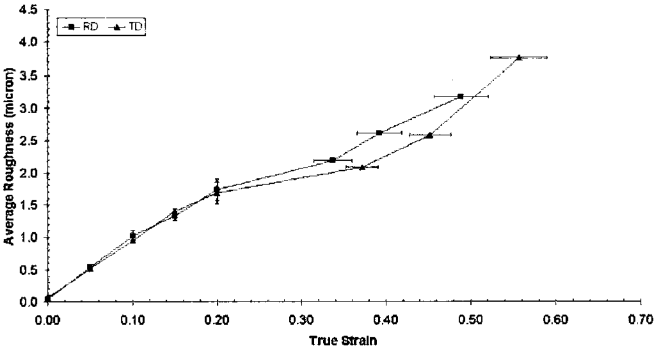

(a) 295K

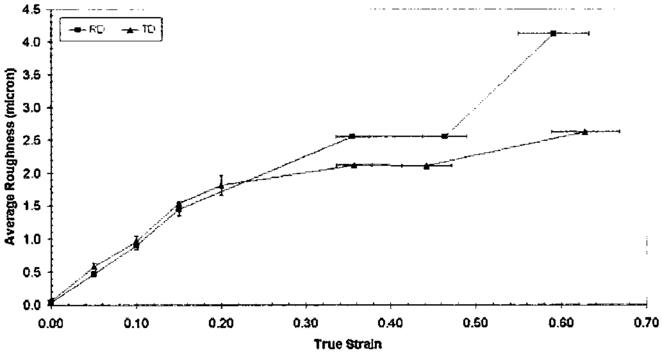

(b) 212K

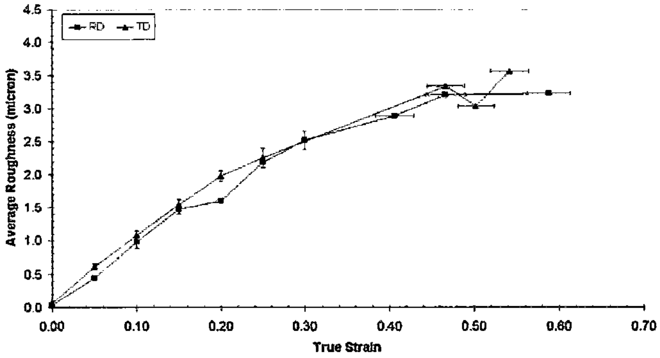

(c) 77K

Figure 4.11: Comparison of samples tested at different orientation at the same temperature.

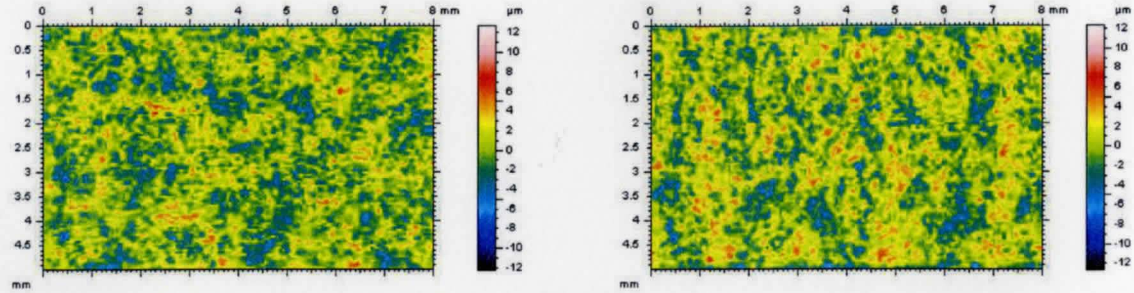

(a) 295K-Parallel (b) 295K-Perpendicular

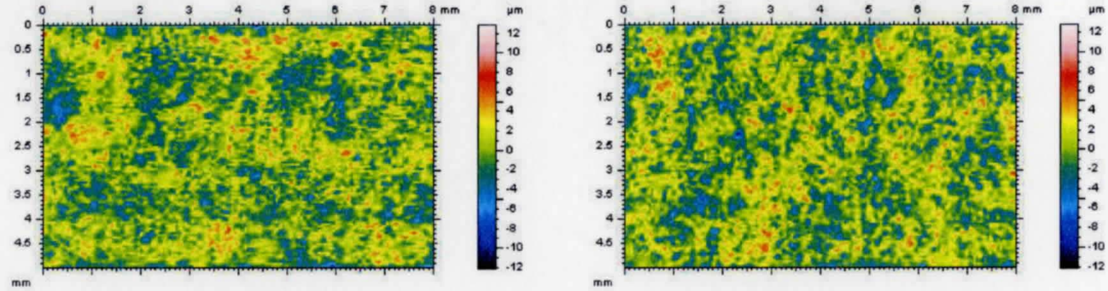

(c) 212K-Parallel (d) 212K-Perpendicular

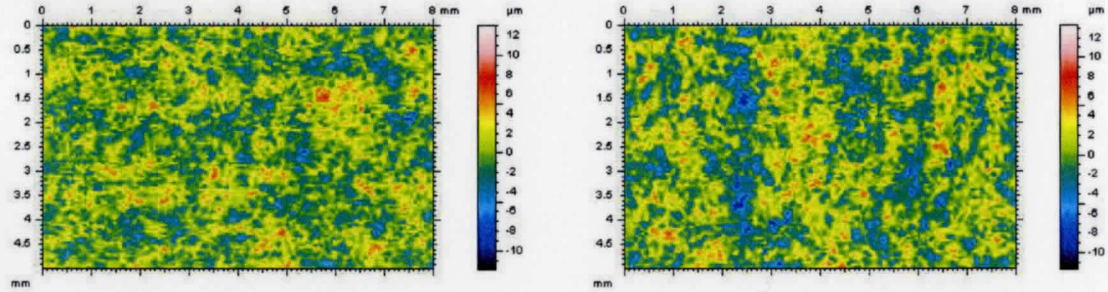

(e) 77K-Parallel (f) 77K-Perpendicular

Figure 4.12: LaserScan Surface Maps for Samples tested at various temperatures to 15% true strain. Rolling direction left to right.

to be more random, although there are still several clusters that are distinctly elongated both parallel and perpendicular to the rolling direction respectively. Samples tested perpendicular to the rolling direction also show a weak although more distinct relationship with the rolling direction. For samples tested at all temperatures, clusters align parallel to the rolling direction. However, distinct peak ridges and valleys which are not aligned parallel to the rolling direction are also present. As the test temperature decreases, the ridges and valleys aligning parallel to the rolling direction appear to become more distinct.

The surface maps were quantitatively analyzed using the covariance function as outlined in Section 3.6.3. Figure 4.13 shows the resulting G(n,m=0) with respect to distance between features along the tensile axis for samples tested at the same orientation. Covariance function for samples tested parallel to the rolling direction show a very steep drop off for features with a distance greater than 0.23mm (10 steps) apart, as shown in Figure 4.13(a). Data values within a spatial distance of 0.23mm apart very similar height values. Features with a spatial distance greater than 0.23mm have height values with non-similar values. Non-similar is used here to describe separation distances over which there is neither a strong similarity, nor a strong difference between the surface heights. There does not appear to be any very strong height relation between surface features with a spatial separation of 0.23mm or greater. Covariance analysis does show that some weak spatial relationships are present. The sample tested at 212K has a distinct bump in the curve for surface features 3.10mm apart (136 steps). For larger separation values, the profiles of the sample tested at 212K has a distinct wavy profile. There is a weak spatial relationship associated over the respective length scale. Sample tested at 77K shows a wavy profile, but with no distinct high or low regions. Sample tested at 295K has the smoothest profile, indicating a strong similarity between heights over all step sizes.

As shown in Figure 4.13(b), samples tested perpendicular to the rolling direction show a stronger relationship between the spacing of surface features in each test temperature as well as between different test temperatures. Similar to samples tested parallel to the rolling

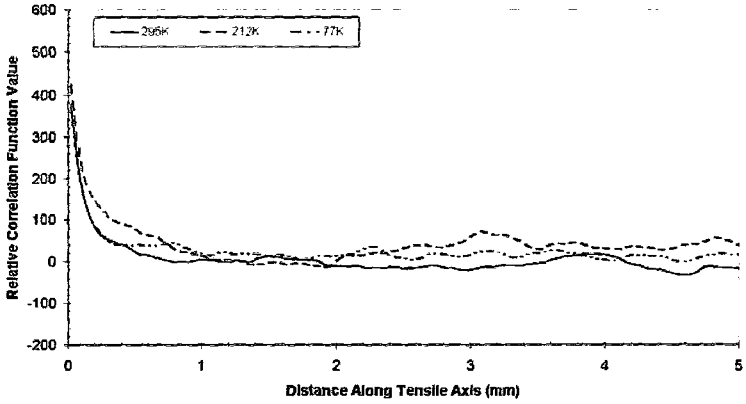

(a) Tested parallel to the rolling direction

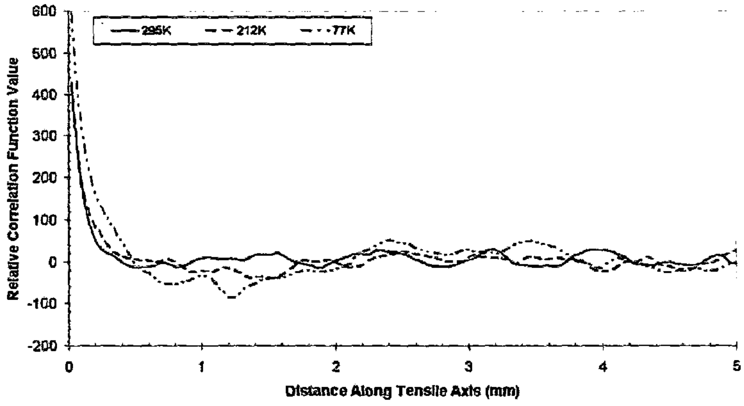

(b) Tested perpendicular to the rolling direction

Figure 4.13: Comparison of Covariance Functions versus Separation Distance between Surface Features for all temperatures.

direction, there is a significant drop off in the curves after a spatial separation between surface point of 0.23mm. At separation distances greater than 0.23mm, it is very interesting to note that the curves for each test temperature show very similar profile. At greater spatial separations, the covariance function with respect to separation distance of surface features develops a distinct wavy profile, showing a weak, but consistent relationship of the distances between surface features. Each curve as a bump over a range of spatial distances between 2.37mm and 2.53mm. They all show a subsequent dip for a separation distance of approximately 2.80mm. The sample tested at 295K shows a weak bump for distance separations 3.19mm and 3.99mm. Sample tested at 77K has a distinct dip in the curve at a surface feature with a separation of 1.23mm, indicating a difference in height at this distance. There is also a noticeable bump at a separation distance of 3.49mm. Both samples tested at 212K and 77K have a dip for spacial separations of 4.04mm and 3.99mm respectively. Table 4.4 gives the separation distance between point on the surface as well as the number of average grain sizes associated with each spatial distance.

Table 4.4: Distances in mm for Specified Step Sizes

Test Temperature	Orientation	Step Size	Distance (mm)	# of Avg. Grain Sizes
All	$\parallel$ RD	10	0.23	2.62
212K	$\parallel$ RD	136	3.10	35.6
All	$\perp$ RD	104	2.37	27.2
All	$\perp$ RD	111	2.53	29.1
All	$\perp$ RD	123	2.80	32.2
295K	$\perp$ RD	140	3.19	36.7
295K	$\perp$ RD	175	3.99	45.8
212K	$\perp$ RD	177	4.04	46.3
77K	$\perp$ RD	54	1.23	14.1
77K	$\perp$ RD	100	2.28	26.2
77K	$\perp$ RD	153	3.49	40.1
77K	$\perp$ RD	175	3.99	45.8

Optical Micrographs

Optical micrographs were taken on all samples tested to 15% true strain at 50X and 100X magnification. Composite images were constructed as per Section 3.7.1. All images show a developed roughness on the surface on the order of several average grain sizes. There does not appear to be a significant difference in the morphology between surfaces tested at different temperatures. The pattern of ridges and valleys on each surface appears to be very similar, showing no distinct difference. However, there is a very weak directionality in the visible ridges in samples tested at 295K and 212K. When tested parallel to the rolling direction, the grain clusters and distinct valleys present on the surfaces of these samples seem to align parallel to the rolling direction. Samples tested perpendicular to the rolling direction at 295K and 212K show grain clusters and valleys that weakly align parallel to the rolling direction. The samples tested parallel to the rolling direction at 77K showed the same weak relationship between the tensile axis and the rolling direction, ridges and valleys align parallel to the rolling direction. Surface features on the sample tested perpendicular to the rolling direction at 77K did not appear to have this relationship. Both grain clusters and valley appeared to form roughly isotropically, preferring neither direction. Composite sample surfaces are shown in Figures 4.14 through 4.19 inclusive.

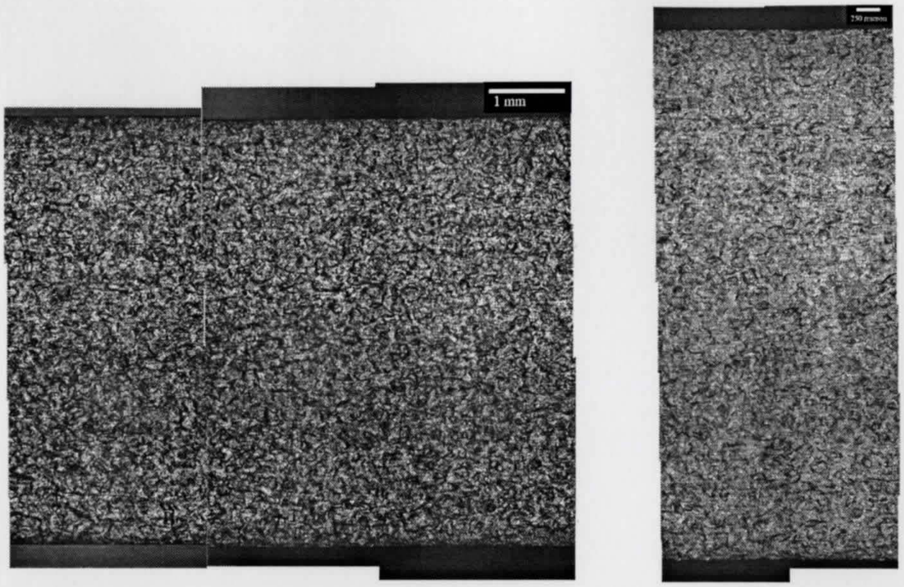

(a) 50X (b) 100X

Figure 4.14: Composite Optical Images for Samples tested Parallel to the rolling direction at 295K.

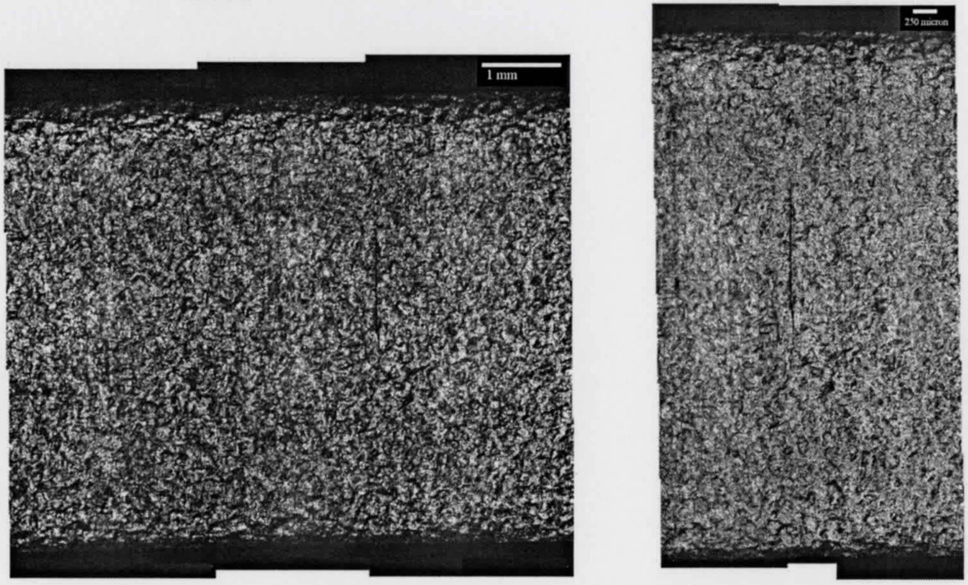

(a) 50X (b) 100X

Figure 4.15: Composite Optical Images for Samples tested Perpendicular to the rolling direction at 295K.

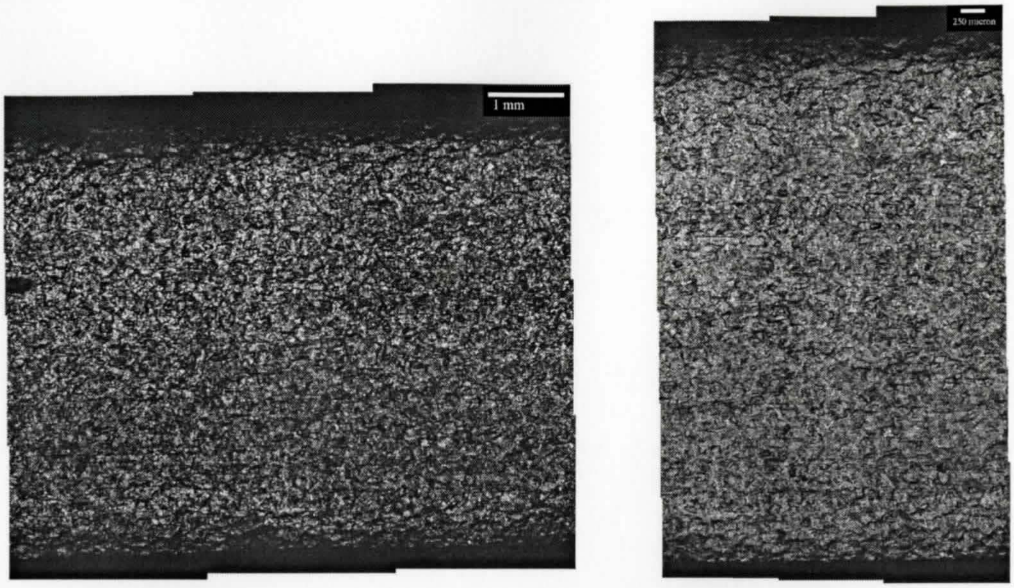

(a) 50X (b) 100X

Figure 4.16: Composite Optical Images for Samples tested Parallel to the rolling direction at 212K.

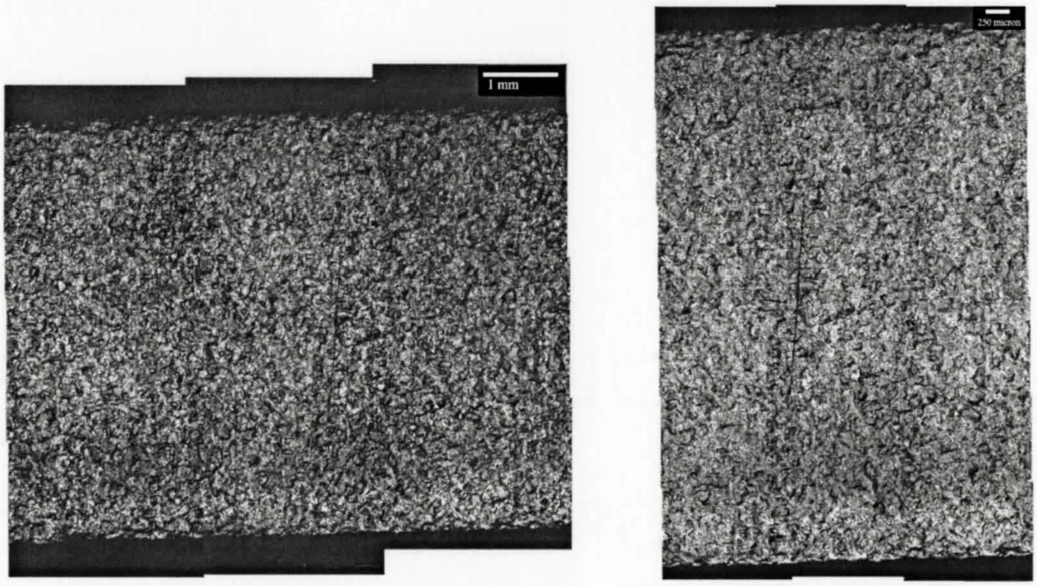

(a) 50X (b) 100X

Figure 4.17: Composite Optical Images for Samples tested Perpendicular to the rolling direction at 212K.

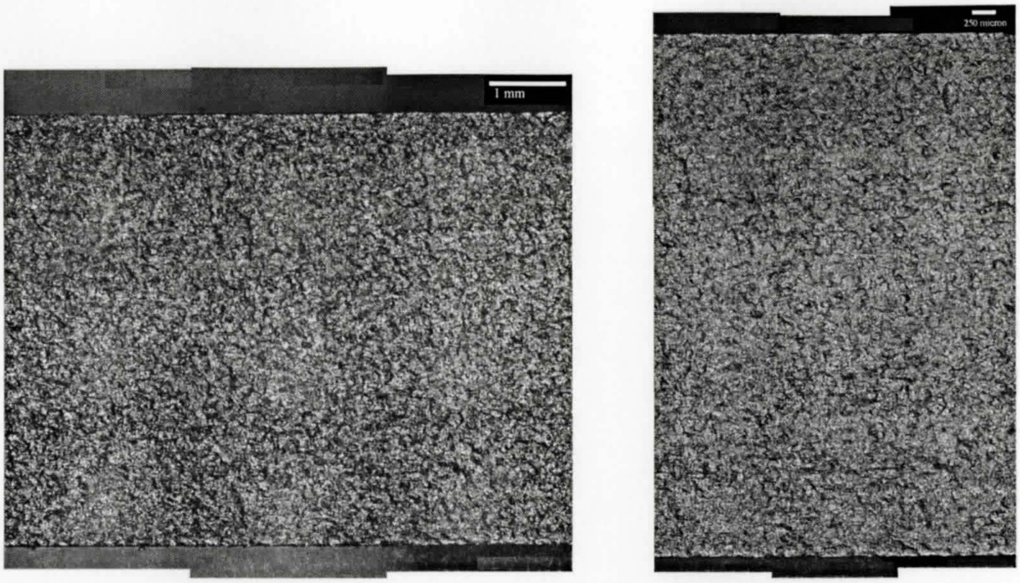

(a) 50X (b) 100X

Figure 4.18: Composite Optical Images for Samples tested Parallel to the rolling direction at 77K.

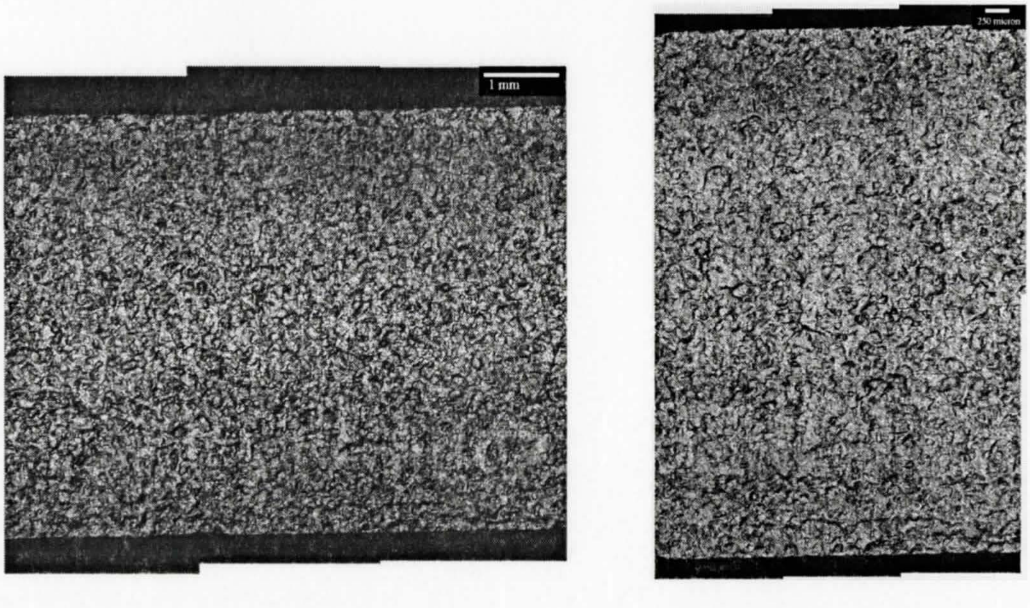

(a) 50X (b) 100X

Figure 4.19: Composite Optical Images for Samples tested Perpendicular to the rolling direction at 77K.

4.4 Experiments Conducted with Different Sample Strengths

AA6111 is an age-hardenable aluminum alloy. Heat treatments affect the type, size and shape of the precipitates formed, which affect the mechanical properties. When heat treated at temperatures above 250^{0}C, non-shearable precipitates form [27]. It has been shown there is a difference in slip distribution between shearable and non-shearable precipitates in this material, which affects the material strength and strain hardening rate. To determine the effect of both material strength and a change in strain hardening rate using a material property on surface roughening, samples were heat treated to form three different tempers designated T4, T6 and OA. Specifics about their heat treatment cycles are in Section 3.4. Samples with three different temper treatments were tested at 295K parallel and perpendicular to the rolling direction over a range of true strain up to and including fracture. Calculated true stress-strain curves were used to determine the mechanical properties. The surface parameters were measured using the Alpha-Step and WYKO systems. LaserScan surface maps and composite optical images were used to quantify the sample morphology.

4.4.1 Mechanical Testing Results

At least 7 samples were tested at 295K for each temper treatment. The difference between true stress-strain curves within one test condition are smaller than the maximum change in stress with respect to strain for samples tested at different temperatures. OA samples tested perpendicular to the rolling direction show the greatest difference, approximately 4%, between the strength of individual samples with respect to true strain. T4 samples tested parallel to the rolling direction have the least amount of strength scatter with respect to strain at approximately 1%. The full series of tensile curves for all samples within one test condition of the two mentioned above conditions are shown in Figure 4.20. Samples tested to fracture are plotted to their ultimate tensile strength.

Three samples were tested to fracture for each set of test conditions. The greatest difference between true fracture stress-strain values occurs in T4 samples tested parallel to the rolling direction. The smallest difference occurs in T6 samples tested perpendicular to the rolling direction. The full stress-strain curves of each sample tested to failure for both test conditions are shown in Figure 4.21. Possible sources for differences between fracture stress and strain values between samples of the same test condition include measurement error as well as a sample having an internal defect with could initiate damage and fracture processes sooner. The values of the true fracture stress and strain values for each test condition are the averages of the values for individual samples. The associated error is calculated using the individual error values of samples within each testing condition using Eqn. 3.11.

The true stress-strain curves up to fracture for samples tested parallel and perpendicular to the rolling direction with fracture values closest to their text condition average is shown in Figure 4.22.

Mechanical properties of samples with different temper treatments are given in Tables 4.5 and 4.6. The artificially aged T6 samples have a higher 0.2% offset yield stress than the naturally aged T4 samples. The OA samples have the highest 0.2% offset yield stress.

The strain hardening rate for each temper treatment show a minimal scatter between individual samples within the same test condition, representatively shown in Figure 4.23. Strain hardening rates for each temper parallel and perpendicular to the rolling direction are shown in Figure 4.25. Although there is a large difference in the range of stresses over which Stage III hardening occurs between the three tempers, there does not appear to be a difference in the slope of the strain hardening rate versus stress once stage III has been reached. Surface roughness data is often plotted versus strain. As such, strain hardening data is shown with respect to strain in Figure 4.25 for comparison.

Associated calculated n-values are given in Table 4.6. There is no difference in strain hardening parameters between samples pulled parallel and perpendicular for a specific temper. T4 samples have an n-value of 0.27, T6 has 0.12 and OA have an n-value of 0.07. K

Table 4.5: Yield Stress and Necking Values for all Temper Samples

Test Temperature	Orientation	0.2% Yield Stress (MPa)	Diffuse Necking		Local Necking	
			Stress (MPa)	Strain (in %)	Stress (MPa)	Strain (in %)
T4	∥ RD	139.3 ± 2.9	356.6 ± 3.0	23.0 ± 0.3	363.3 ± 3.0	25.3 ± 0.3
	⊥ RD	138.0 ± 0.6	354.5 ± 4.2	22.7 ± 0.4	359.2 ± 4.0	24.3 ± 0.9
T6	∥ RD	289.7 ± 8.9	426.1 ± 6.1	14.9 ± 1.2	434.2 ± 7.1	17.2 ± 1.4
	⊥ RD	290.5 ± 7.3	427.4 ± 5.5	14.2 ± 1.1	433.0 ± 8.7	15.8 ± 1.9
OA	∥ RD	312.7 ± 4.6	381.6 ± 3.6	9.4 ± 0.1	387.2 ± 3.3	11.3 ± 0.2
	⊥ RD	309.8 ± 6.1	383.6 ± 8.2	9.3 ± 0.6	389.3 ± 9.3	11.2 ± 0.9

Table 4.6: Calculated Fracture and n-values for Temper Samples

		Calculated Fracture		Strain Hardening Values		
Temper	Orientation	Stress (MPa)	Strain (in %)	n-values	K values (MPa)	R^2 value
T4	∥ RD	469.9 ± 26.3	70.8 ± 5.5	0.269 ± 0.003	486.4 ± 37.9	0.987
	⊥ RD	468.5 ± 25.9	64.1 ± 5.5	0.272 ± 0.002	520.8 ± 19.7	0.988
T6	∥ RD	548.5 ± 22.0	57.3 ± 4.0	0.122 ± 0.008	17.02 ± 3.29	0.979
	⊥ RD	592.9 ± 26.3	57.8 ± 4.5	0.123 ± 0.005	16.96 ± 1.93	0.984
OA	∥ RD	523.8 ± 23.2	63.1 ± 4.5	0.069 ± 0.001	4.945 ± 0.147	0.984
	⊥ RD	500.5 ± 21.6	56.7 ± 4.3	0.074 ± 0.005	5.569 ± 0.717	0.990

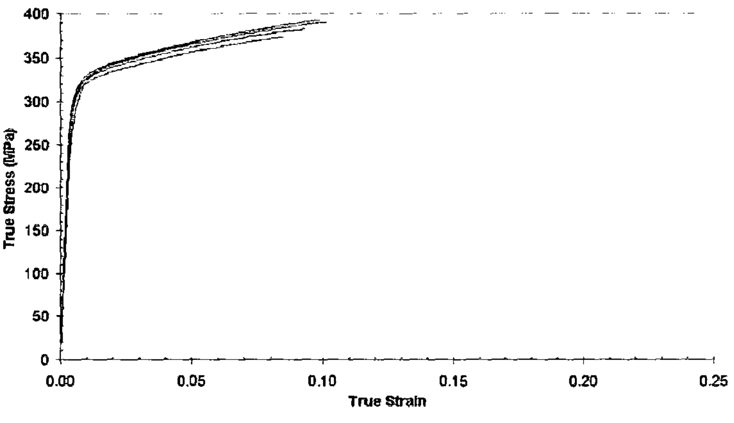

(a) OA Samples tested perpendicular to the rolling direction

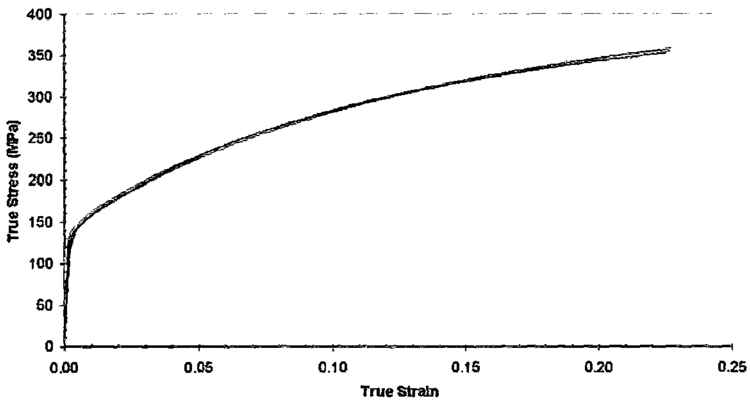

(b) T4 Samples tested parallel to the rolling direction

Figure 4.20: Selected Full Series curves for samples within Two different Temper Treatment conditions.

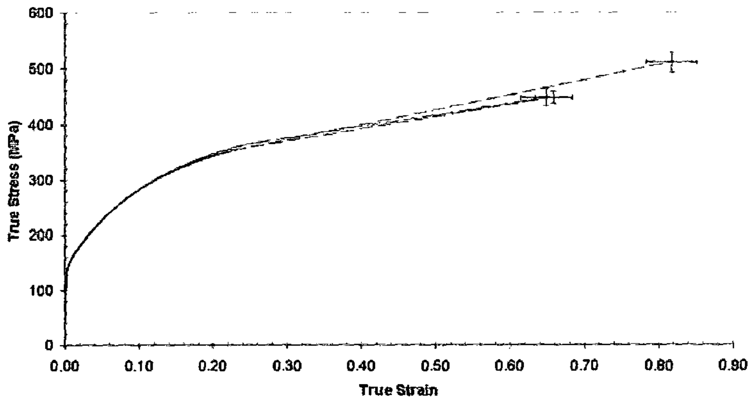

(a) T4 samples tested parallel to the rolling direction - Greatly differing fracture statistics between samples

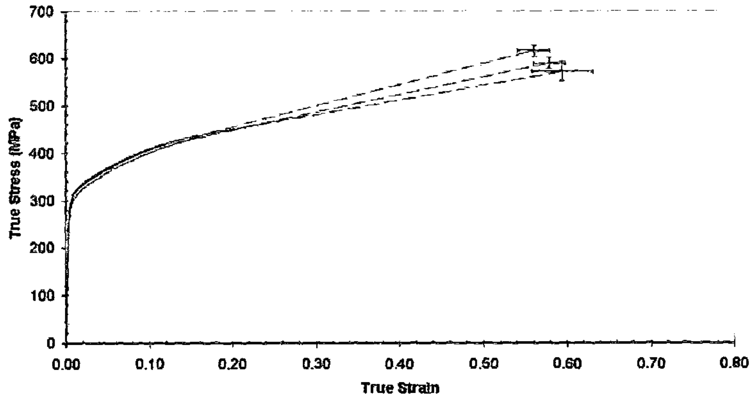

(b) T6 samples tested perpendicular to the rolling direction - Close fracture statistics between samples

Figure 4.21: Samples tested to fracture illustrating the possible range of fracture stresses and strains for samples with different temper treatments.

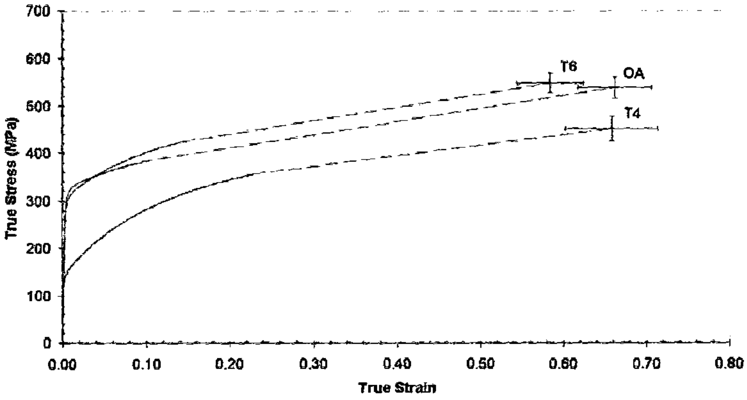

(a) Tested parallel to the rolling direction

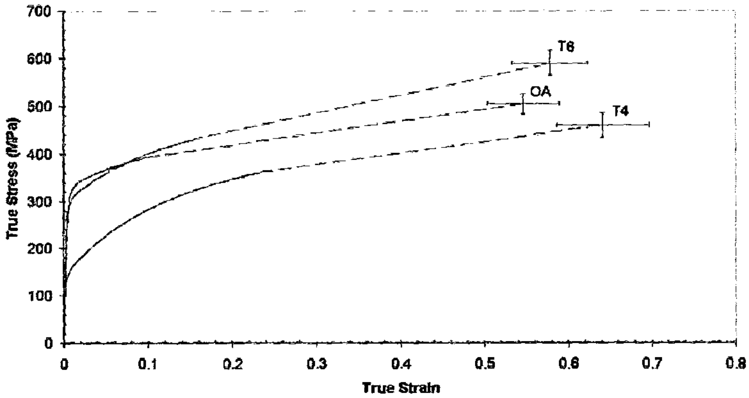

(b) Tested perpendicular to the rolling direction

Figure 4.22: Samples from each temper treatment tested to Fracture with respect to orientation.

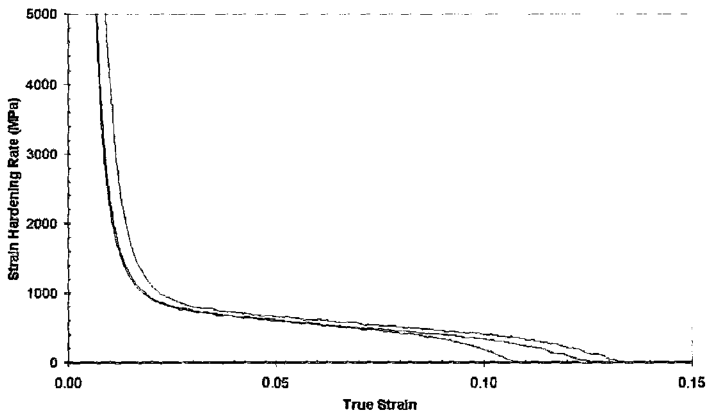

Figure 4.23: Strain Hardening rate for all OA samples tested to fracture perpendicular to the rolling direction.

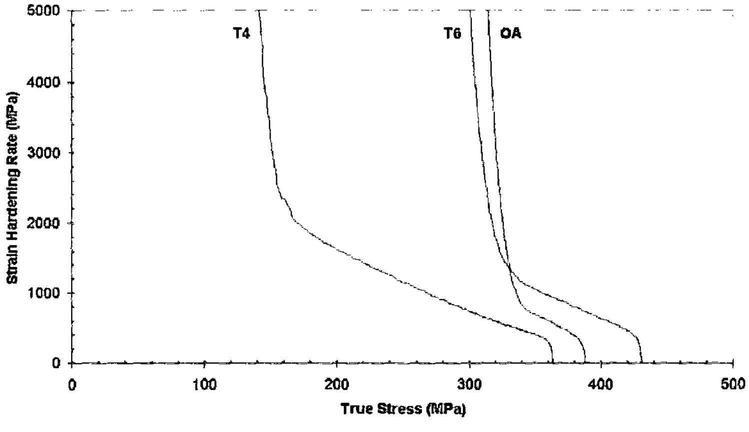

(a) Tested parallel to the rolling direction

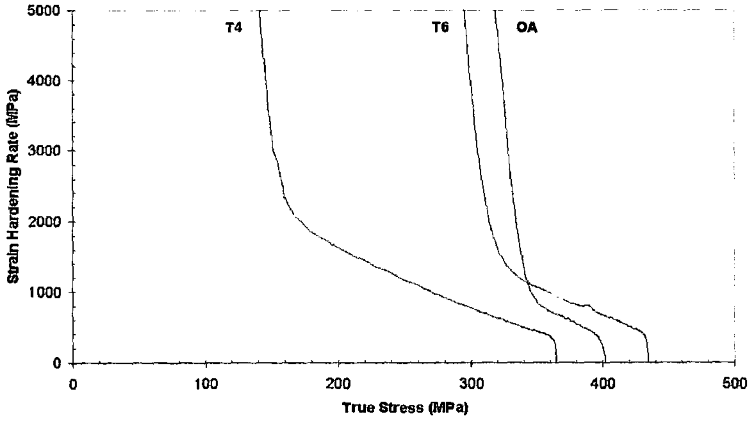

(b) Tested Perpendicular to the rolling direction

Figure 4.24: Strain Hardening Curves for all temper treatments with respect to true stress.

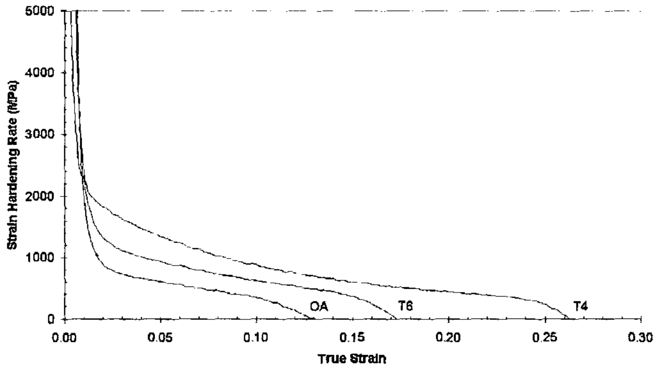

(a) Tested parallel to the rolling direction

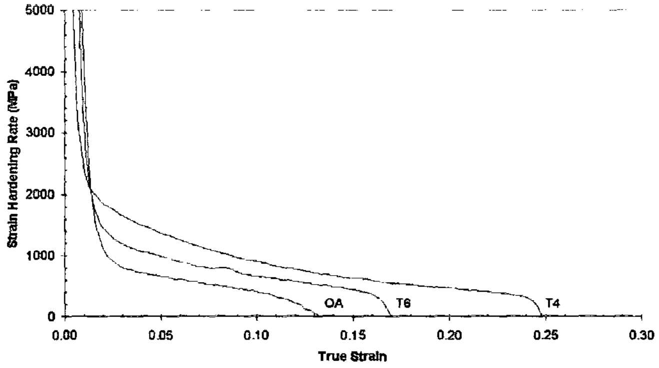

(b) Tested Perpendicular to the rolling direction

Figure 4.25: Strain Hardening Curves for all tempers with respect to true strain.

values for T4 and T6 samples are 2.72, and OA samples have a lower K value of 2.65. The smallest R^2 value overall for the temper set is 0.9787.

4.4.2 Surface Parameters

For each temper treatment and orientation, all roughness parameters increase approximately linearly with increasing true strain. A representative set of surface parameters plotted again true strain for OA samples tested parallel to the rolling direction is shown in Figure 4.26. The average roughness measured using the Alpha-Step system and the WYKO system are very close. As seen in Figure 4.26, the average roughness trend line from measurement using the Alpha-Step system is almost completely hidden by the WYKO average roughness trend line. The ten-point mean roughness increases more rapidly, or equivalently has a higher roughening rate, than the average roughness in all test conditions corresponding with the increase in magnitude of peaks and valleys on the surface.

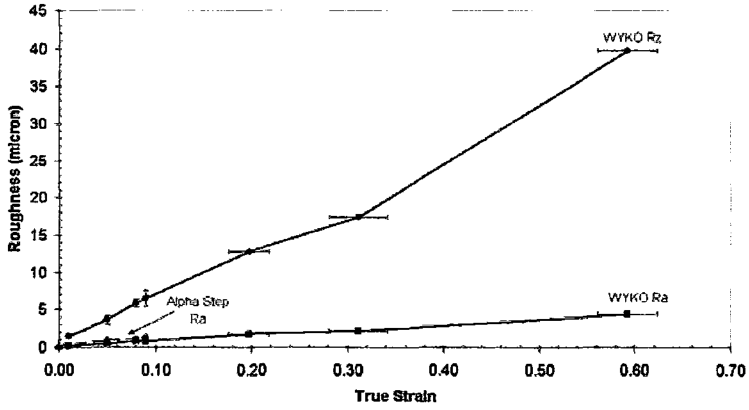

Figure 4.26: Comparison of measurements taken using Alpha-Step and WYKO systems - OA samples tested parallel to the rolling direction.

The average roughness for each temper treatment with respect to orientation is shown in Figure 4.27.

For samples tested perpendicular to the rolling direction, the rate of average roughening appears the same before and after the onset of localization. Samples tested parallel to the rolling direction show a slightly larger difference in pre-localization roughness between individual temper treatments. However, samples show a difference in the average roughness at higher strains. The T6 sample appear to continue roughening at the same rate post-localization. The T4 sample seems to have a drastically reduced roughening rate between 20 to 35% strain. After 35% strain, the roughness increases at its previous rate,

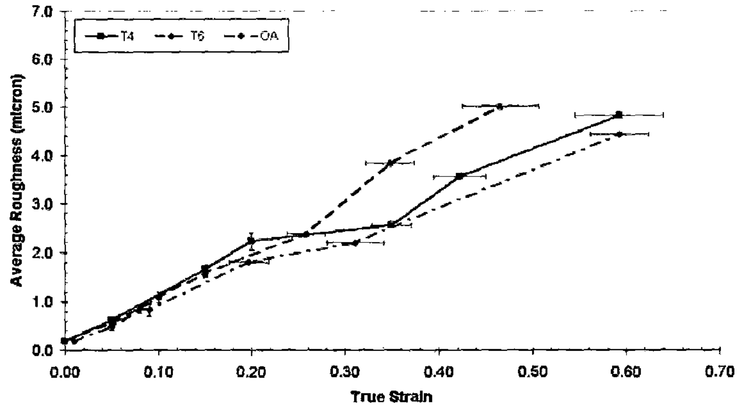

(a) Tested parallel to the rolling direction

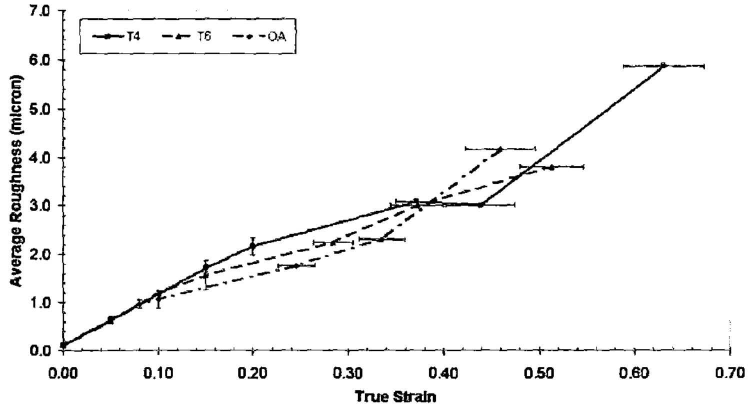

(b) Tested Perpendicular to the rolling direction

Figure 4.27: Average Roughness values as measured using the WYKO system for each temper with respect to orientation.

leading to a lower average roughness at higher strains than the T6 sample. The OA sample also seems to have a region of reduced roughening between 20% and 32% true strain. The T4 sample has a higher roughening rate than the OA sample with respect to strain.

The pre-localization average roughening rate for each temper treatment is the same for each test orientation as shown in Figure 4.28. The post-localization average roughening rate for the T4 and OA samples does not differ between sample orientation. The T6 samples show a difference in the roughness after localization, with the sample tested parallel to the rolling direction appearing to roughen faster that the one tested perpendicular to the rolling direction.

The ten-point mean roughness values with respect to strain and orientation show a similar relationship between different temper treatments as the average roughness values. The T4 and OA samples tested parallel to the rolling direction have very similar ten-point roughness with respect to strain. It is assumed that the roughness measurement taken at 35% in the T6 series is artificially high, possibly due to an abnormal surface feature or surface contamination. If the point at 35% is ignored, the T6 sample still appears to have a slightly higher ten-point roughness at higher strains. There is no significant difference between the ten-point mean roughness for samples with temper treatments tested perpendicular to the rolling direction. The roughening rate appears to be the same for each of the three tempers.

4.4.3 Surface Morphology

LaserScan surface maps and composite optical images were used to quantify the surface morphology for each combination of temper treatment and test orientation.

LaserScan Results

LaserScan surface maps were taken of samples with different temper treatments tested to strains close to localization as well as T4 samples deformed to increasing values of

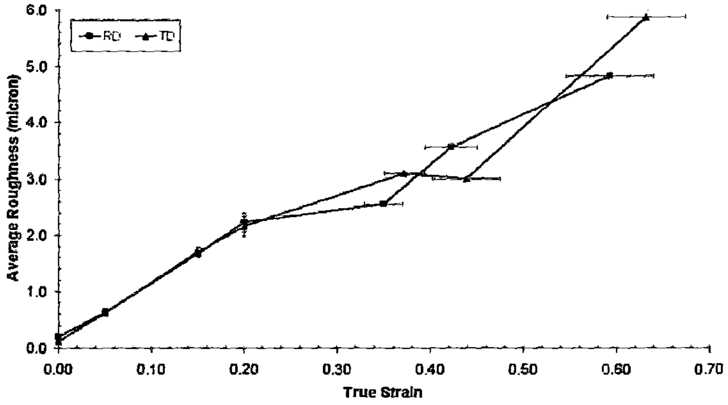

(a) T4

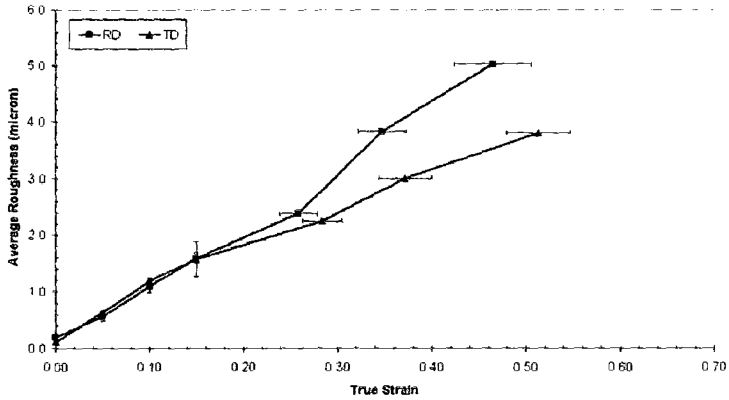

(b) T6

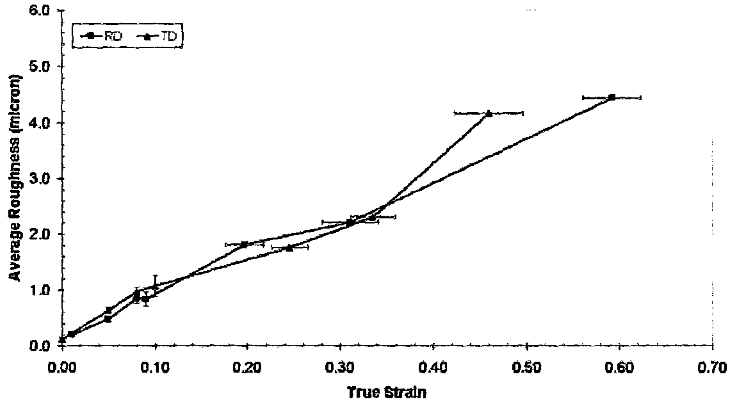

(c) OA

Figure 4.28: Comparison between average roughness values tested at orientation at the same temper treatment.

strain. LaserScan data from the T4 samples deformed to different strains is used to chart the evolution of surface features with respect to strain. LaserScan data from samples of different temper treatments are used to compare the surface development between tempers.

Surface maps for T4 samples tested at both orientations to 5%, 15% and 20% true strain are shown in Figure 4.29. A separate sample is tested and measured at each strain. The height range is scaled to a 40 μm span. As the strain increases, there is a distinct increase in the number and height of surface features such as clusters. For samples tested parallel to the rolling direction, grain clusters start to form that appear elongated parallel to the rolling direction, as seen in Figure 4.29(c). As strain increases, grain clusters continue to align parallel to the rolling direction. When samples are tested perpendicular to the rolling direction, the grain cluster shape does not show any particular alignment with the rolling direction. Features on the surface at higher strain do not appear to have any directional preference with respect to the rolling direction.

Surface maps for samples with different temper treatments tested to the indicated value strain are shown in Figure 4.30. Each surface map has a different height range; the T4 sample scan is scaled to a 40 μm span, T6 to a 20μm span, and OA to a 15 μm span. Both the T4 and T6 maps show grain clusters elongated parallel to the rolling direction. The T6 map also shows groups of clusters aligning perpendicular to the rolling direction. The surface map of the OA sample shows some grain clusters elongated parallel to the rolling direction. This alignment does not appear as prominent as in either of the surface maps for the T4 or T6 samples. Samples tested perpendicular to the rolling direction show a slightly stronger alignment of clusters parallel to the rolling direction. These surface maps have the same height range as those tested parallel to the rolling direction. Figure 4.30(d) shows that individual clusters on the surface of the T6 sample do not appear to have a directional preference. The ridges and valleys on the surface of the T4 and OA samples appear to align parallel with the rolling direction.

Analyzed surface maps using the covariance function for T4 tested to different strains

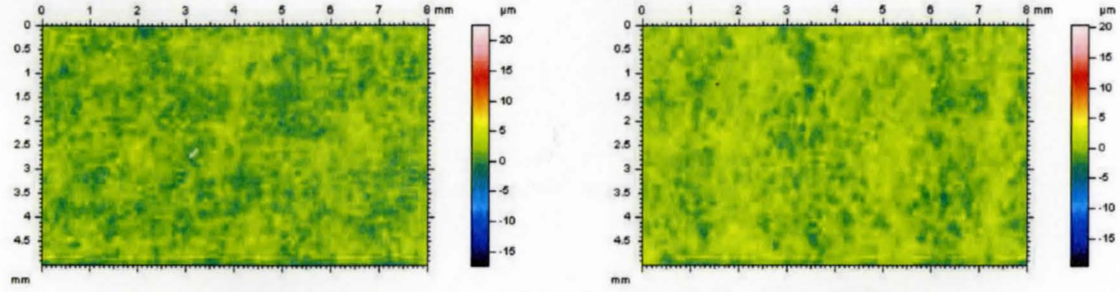

(a) 5% true strain-Parallel (b) 5% true strain-Perpendicular

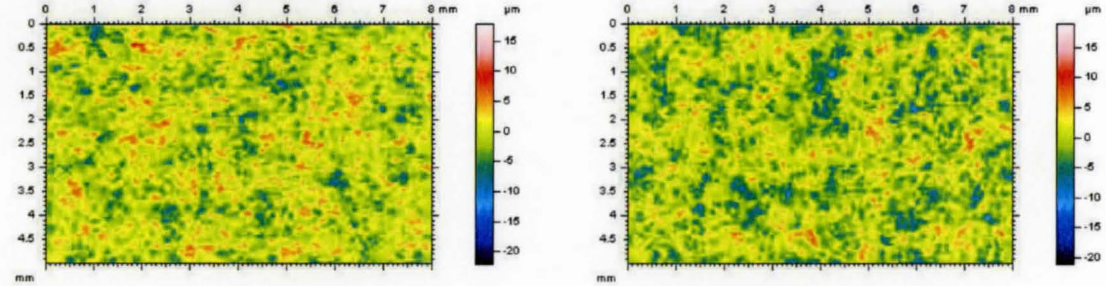

(c) 15% true strain-Parallel (d) 15% true strain-Perpendicular

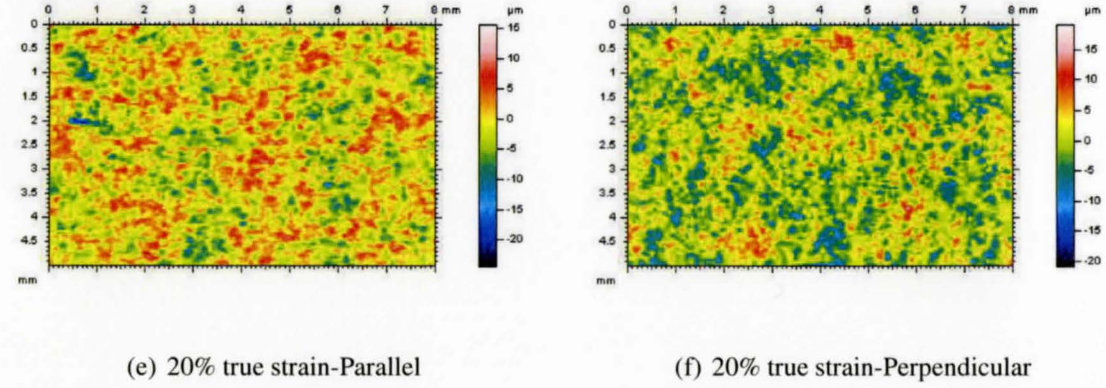

(e) 20% true strain-Parallel (f) 20% true strain-Perpendicular

Figure 4.29: LaserScan surface maps for T4 true strain series tested to various strains at both orientations. Rolling direction left to right.

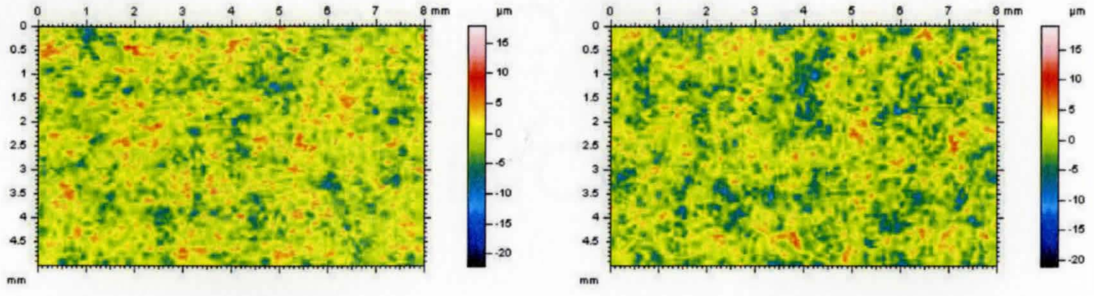

(a) T4, 15% true strain-Parallel

(b) T4, 15% true strain-Perpendicular

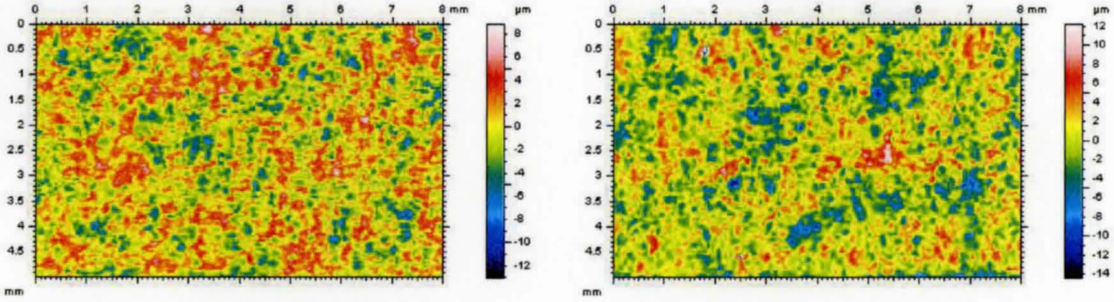

(c) T6, 15% true strain-Parallel

(d) T6, 15% true strain-Perpendicular

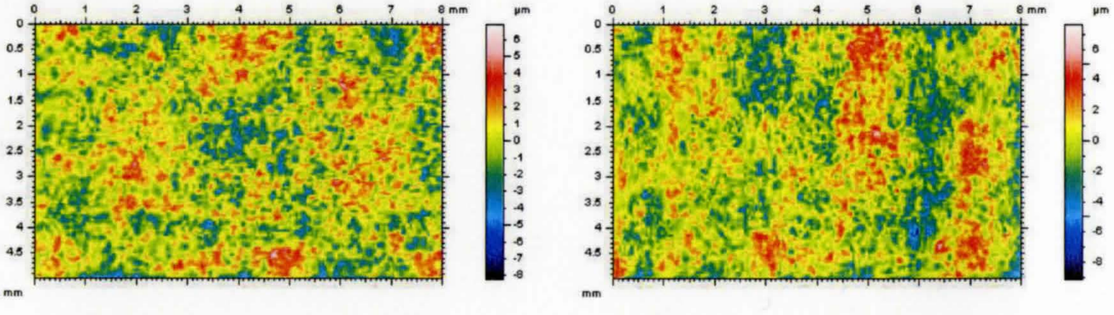

(e) OA, 8% true strain-Parallel

(f) OA, 8% true strain-Perpendicular

Figure 4.30: LaserScan surface maps for Samples with different Temper Treatments. Rolling direction left to right.

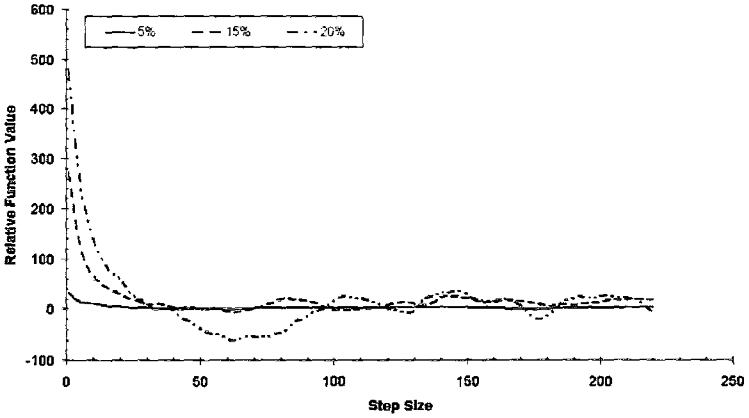

(a) Tested parallel to the rolling direction

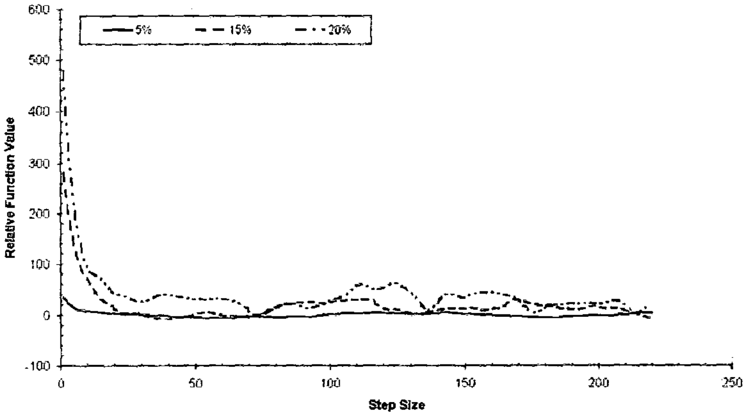

(b) Tested Perpendicular to the rolling direction

Figure 4.31: Covariance Function, G(n,m=0), Results for a true strain series of T4 Samples for each orientation.

are shown in Figure 4.31 with respect to the distance between surface features. In samples tested in both orientations, the profiles develop increasingly deeper dips and higher bumps, following the development of surface features with increasing strain. The samples tested to 5% true strain parallel to the rolling direction have flat curves. At 5% strain the surface has not yet developed a significant amount of deformation roughness. At 15% true strain, a distinct pattern of undulations has developed on the G(n,m=0) versus distance plot. These correspond to the development of spatially related peaks and valleys on the sample surface. The curve at 20% true strain is very similar to the 15% strain curve, but does show an increase in the magnitude of the dips and bumps, as shown in Figure 4.31(a). Samples tested perpendicular to the rolling direction show the same development of the G(n,m=0) versus feature spacing plot with respect to increasing strain - the curves becoming more undulated with increasing strain. However, the progression is not a clear. The plot for the sample tested to 20% true strain sits higher on the plot. This effect is most likely due to sample curvature. However, in Figure 4.31(b) it can be clearly seen that the sample tested to 20% has an increase in both the number and magnitude of undulations as compared with the samples tested to 5%.

A comparison of the spatial relationship between surface features along the tensile axis between different tempers with respect to orientation is shown in Figure 4.32. Surface maps taken of the T4 samples are scaled so that they contain more pixels per inch than maps taken of the T6 or OA samples, which mean the spatial distance per step size is different between T4 and T6/OA surface maps. One step size for the T4 sample is 22.8 μm. For the T6 and OA samples, one step size is 21.6 μm. The plots of the covariance function versus distance along the surface between features is already scaled to compensate for this difference. There is a strong similarity in the heights of surface features over a separation less than 0.23mm. It can be seen clearly in both figures that the magnitude of the value of the covariance function below a separation distance of 0.23mm is less for the T4 sample. This is likely due to the height scaling of the input surface maps. With the smaller height range, T6 and OA samples artificially show a stronger relationship between neighbouring data points than the T4 sample.

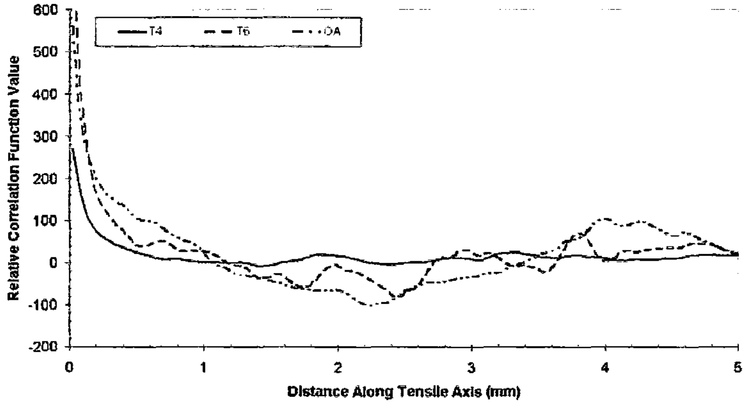

(a) Tested parallel to the rolling direction

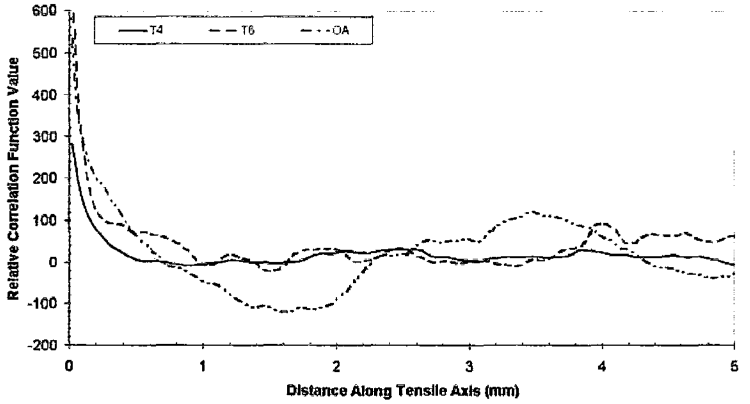

(b) Tested perpendicular to the rolling direction

Figure 4.32: Comparison of Covariance Functions versus separation of features along the tensile axis for all tempers.

For samples tested parallel to the rolling direction, the T4 sample shows weak similarities at separation distances of 1.87mm and 3.37mm. There are no distinct dips. The T6 sample has bumps at separation distances of 1.99mm, 2.96mm, and 3.80mm, and dips at 1.73mm, 2.46mm, and 3.56mm. The OA sample has a bump and a dip at 4.02mm, and

2.25mm separation distances respectively. For samples tested perpendicular to the rolling direction, the T4 sample shows the least amount of similarity or difference for separation distance. The T4 sample shows bumps at separation distances of 2.62mm and 3.88mm, and a dip at 3.08mm. The T6 sample has bumps at separation distances of 1.25mm, 1.97mm, 2.46mm, and 4.02mm. Dips occur at separation distances of 1.04mm, 1.51mm, and 2.16mm. The OA sample shows a significant dip region over a range of separation distances from 1.36mm to 1.94mm, and a significant bump for a separation distance of 3.48mm. Table 4.7 shows the distance on the surface and its relation to the average grain size for the distances previously listed.

Optical Micrographs

Optical images for T4 and T6 samples were taken on samples deformed to 15% true strain at 25X, 50X and 100X. Optical images the OA sets were taken on samples deformed to 8% true strain over the same magnification range. Composite images of pictures taken at 50X and 100X magnification were compiled using methods outlined in Section 3.7.1.

Images taken under 25X magnification were used to determine if any difference exists in the appearance of surface features with respect to sample placement on the microscope stage. There was a concern that different surface features could become more prominently visible depending how the light from the microscope illuminated the area. Images were taken of the same area on the sample when its tensile axis was placed left to right and back to front. For each temper and orientation, there appeared to be no difference in the appearance of the surface features with respect to sample alignment.

Pictures of the individual sample surfaces taken at 50X and 100X magnification of each temper testing condition are shown in Figures 4.33 through 4.38. In the T4 sample tested parallel to the rolling direction, grain clusters and valleys appear elongated parallel to the rolling direction, as seen in Figure 4.33. When tested perpendicular to the rolling direction, this preferential alignment of surface features is not present, and grain clusters

Table 4.7: Distances in mm for Specified Step Sizes for Temper samples.

Test Temperature	Orientation	Step Size	Distance (mm)	# of Avg. Grain Sizes
T4	∥ RD	10	0.23	2.62
T4	∥ RD	82	1.87	21.5
T4	∥ RD	148	3.37	38.8
T6	∥ RD	10	0.22	2.48
T6	∥ RD	80	1.73	19.8
T6	∥ RD	92	1.99	22.8
T6	∥ RD	114	2.46	28.3
T6	∥ RD	137	2.96	34.0
T6	∥ RD	165	3.56	40.9
T6	∥ RD	176	3.80	43.7
OA	∥ RD	104	2.25	25.8
OA	∥ RD	186	4.02	46.1
T4	⊥ RD	115	2.62	30.1
T4	⊥ RD	135	3.08	35.3
T4	⊥ RD	170	3.88	44.5
T6	⊥ RD	48	1.04	11.9
T6	⊥ RD	58	1.25	14.4
T6	⊥ RD	70	1.51	17.4
T6	⊥ RD	91	1.97	22.6
T6	⊥ RD	100	2.16	24.8
T6	⊥ RD	114	2.46	28.3
T6	⊥ RD	186	4.02	46.1
OA	⊥ RD	63	1.36	15.6
OA	⊥ RD	90	1.94	22.3
OA	⊥ RD	161	3.48	39.9

remain mostly isotropically shaped.

There was an added difficulty in determining cluster shape orientation between the T6 samples. The sample tested parallel to the rolling direction has a distinct surface film, which most likely developed during electropolishing. However, the underlying grain clusters and valleys are still visible, as shown in Figure 4.35. T6 sample tested perpendicular to the rolling direction shows some pitting on the surface, also most likely from the electropolishing procedure. The T6 samples showed a similar relationship between cluster shape and relation to the rolling direction as the T4 samples; grain clusters elongated parallel to the rolling direction when tested parallel to the rolling direction, but no shape change when tested perpendicular to the rolling direction. Comparing Figures 4.33 and 4.35 as well as 4.34 and 4.36 shows little to no difference between T4 and T6 sample surfaces tested in the same orientation.

The OA samples were tested to 8% true strain, close to half the amount of strain to which the T4 or T6 samples were tested. due to the onset of localized necking at lower true strains in the OA samples, the highest true strain that could be consistently reached was 8%. The surfaces show very different morphologies than the T4 and T6 surfaces. The OA sample tested parallel to the rolling direction does not show any grain cluster elongation. However, the sample tested perpendicular to the rolling direction appears to have distinct bands which look like depressed regions running parallel to the rolling direction, as seen in Figure 4.38. There also appears to be a slight elongation of the grain shape perpendicular to the rolling direction.

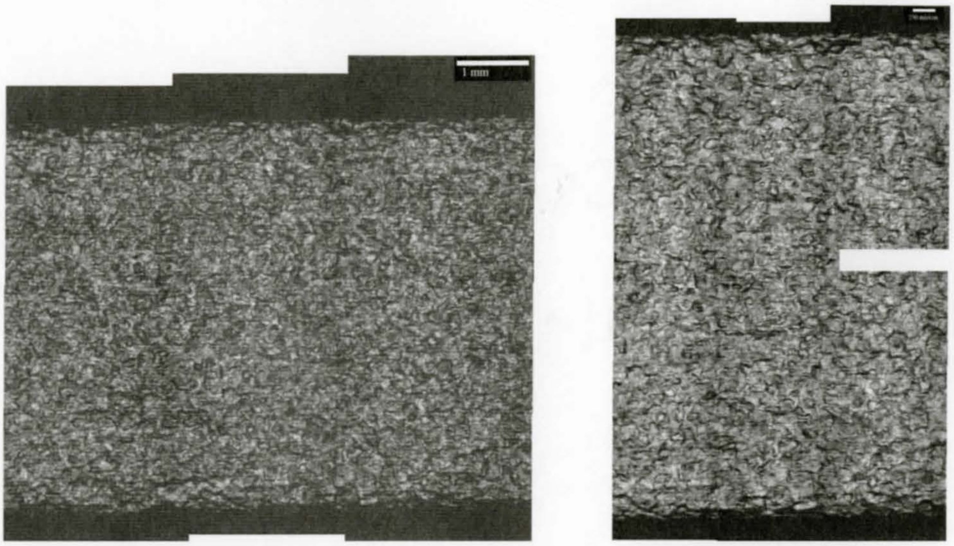

(a) 50X (b) 100X

Figure 4.33: Composite Optical Images for T4 Samples tested parallel to the rolling direction.

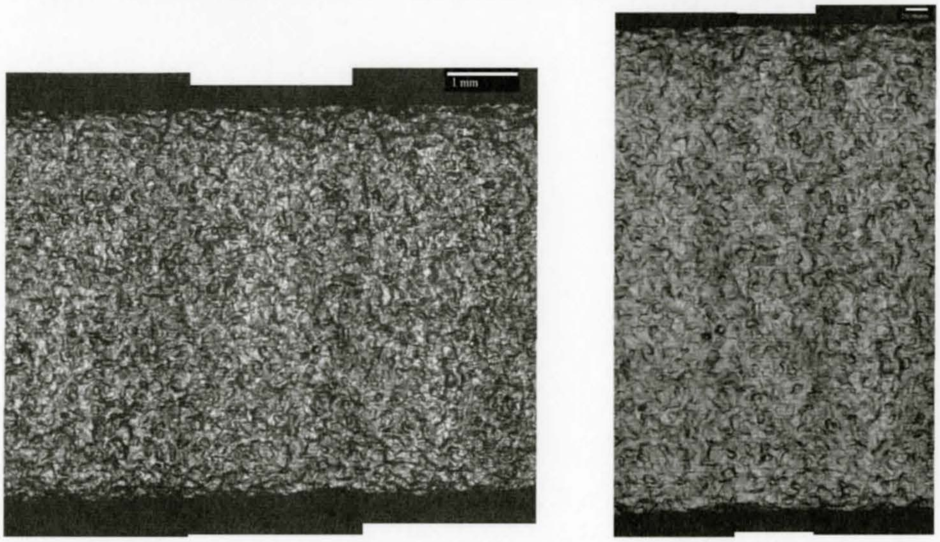

(a) 50X (b) 100X

Figure 4.34: Composite Optical Images for T4 Samples tested perpendicular to the rolling direction.

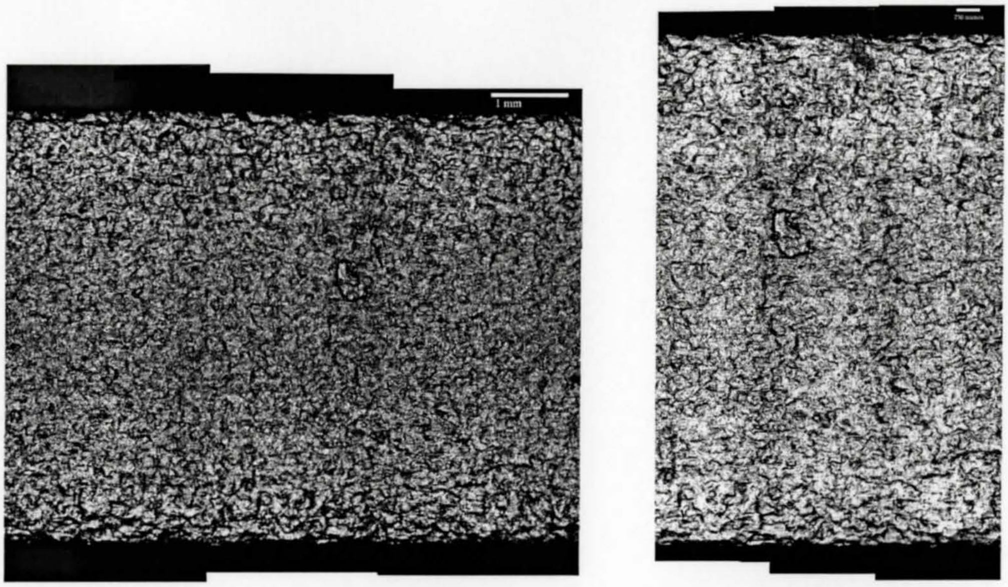

(a) 50X (b) 100X

Figure 4.35: Composite Optical Images for T6 Samples tested parallel to the rolling direction.

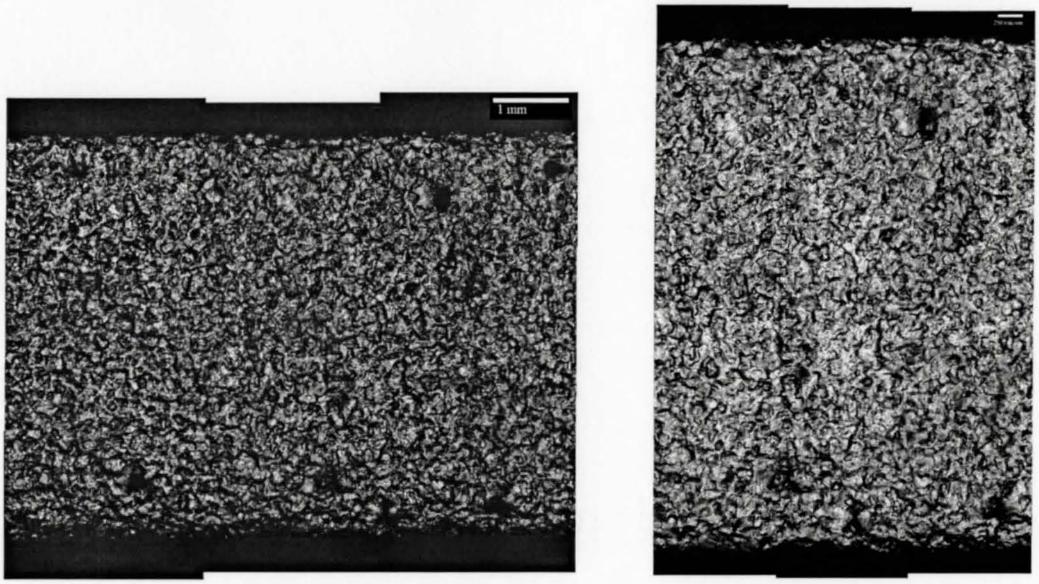

(a) 50X (b) 100X

Figure 4.36: Composite Optical Images for T6 Samples tested perpendicular to the rolling direction.

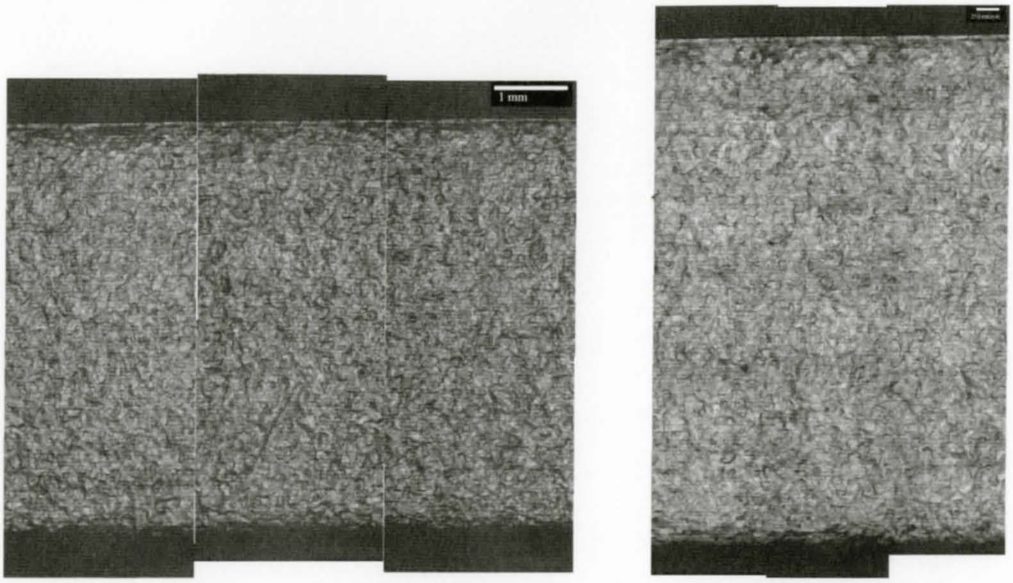

(a) 50X (b) 100X

Figure 4.37: Composite Optical Images for OA Samples tested parallel to the rolling direction.

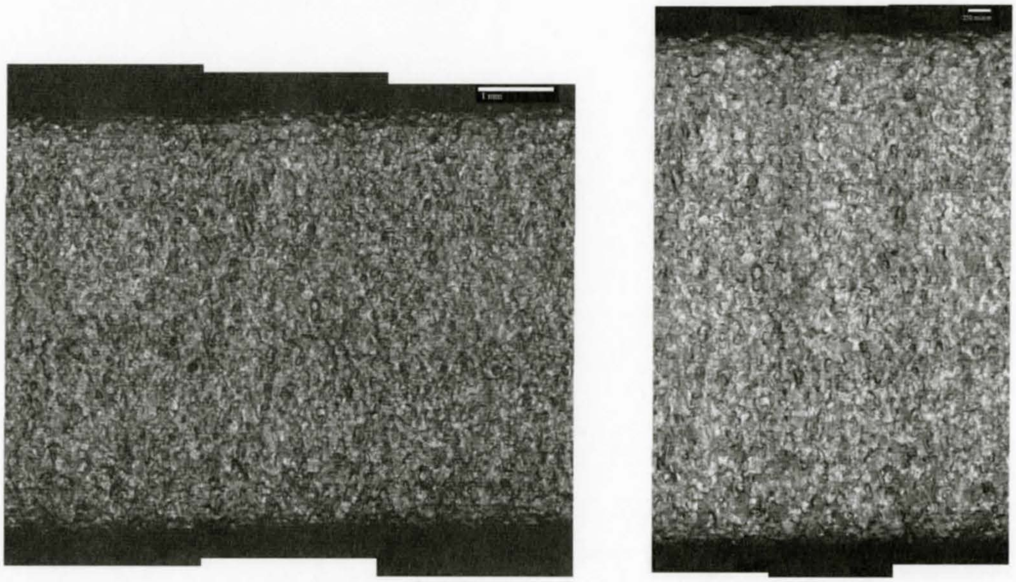

(a) 50X (b) 100X

Figure 4.38: Composite Optical Images for OA Samples tested perpendicular to the rolling direction.

4.5 Effect of Intermediate Polish

A second objective of this study was to determine how the surface roughness develops when deformed after an intermediate polish. Samples of both orientations were tested to 20% true strain, then given an intermediate polish and tested to additional strains as well as to fracture. The mechanical properties were determined using the true stress-strain curves, and the surface was quantified using parameter generated by scans taken using the WYKO system.

4.5.1 Mechanical Testing Results

At least 9 T4 samples per orientation were tested at 295K. The differences between the tensile curves of samples tested with the same orientation was less than 2% in strength for the same strain, as shown in Figure 4.39. Both samples tested to fracture during the second tensile run show a distinct 10MPa drop in strength between their strength at unloading after tensile testing during Run#1 and the strength at the onset of plastic deformation during Run#2. Samples are tested to fracture using one of three different testing procedures as outlined in Section 3.5. There are some differences in the diffuse necking strain between samples fractured under different testing procedures, as outlined in Table 4.8. All three curves show a similar mechanical response for samples tested parallel to the rolling direction, although they differ slightly in their necking strains. The sample tested to fracture during Run#1 with only an initial polish has a 3% lower necking strain than either of the samples tested to fracture during Run#2.

Samples tested perpendicular to the rolling direction show a greater difference in the strength with respect to strain between individual samples. Similar to the samples tested parallel to the rolling direction, the sample with only an initial polish tested to fracture during Run#1 has a necking strain approximately 2% lower than the samples fractured during the second run. These differences may be close to error values, as calculated error

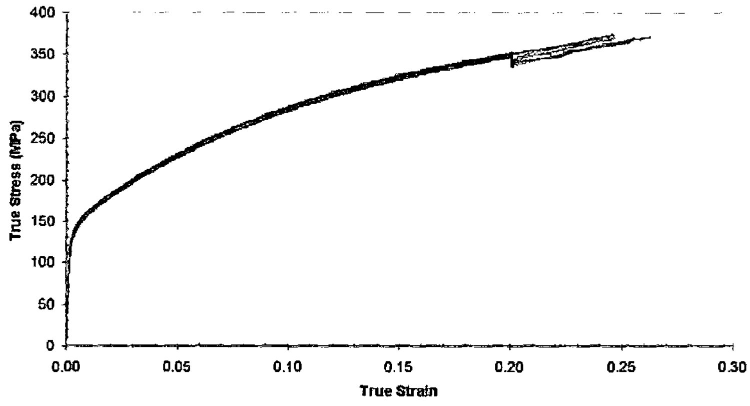

Figure 4.39: Full Test Condition Sample Sets tested Perpendicular to the rolling direction.

in the diffuse necking is as high as 1% for other experimental runs which tested up to three samples per test condition (refer to Table 4.2 on page 57 and Table 4.5 on page 80). The 0.2% offset yield stress for each orientation is the same as that of the 0.2% offset yield stress for T4 samples tested with the same orientation.

Table 4.8: Average Yield Stress and Specific Diffuse Necking Values for Fractured Samples of Repolish Experiment Runs

Orientation	0.2% Yield Stress (MPa)	Surface Condition	Fractured During	Diffuse Necking	
				Stress (MPa)	Strain (in %)
||RD	137.8 ± 2.9	Initial Polish Only	Run 1	363.3	24.5
		Initial Polish, No Intermediate Polish	Run 2	376.2	27.2
		Initial and Intermediate Polish	Run 2	371.7	26.2
⊥RD	140.0 ± 3.3	Initial Polish Only	Run 1	364.7	23.5
		Initial Polish, No Intermediate Polish	Run 2	376.2	27.2
		Initial and Intermediate Polish	Run 2	371.7	26.2

Samples tested to fracture parallel and perpendicular to the rolling direction with an intermediate polish are shown in Figure 4.40. Their true stress strain curves to maximum load are almost identical. Both samples show a strength decrease of 5MPa at 20% true strain as a result of unloading and resuming the test 48 hours later to accommodate the intermediate polishing step. The true fracture stress and strain appear to differ significantly, particularly the fracture strain. However, as other experimental runs have illustrated, it is possible to have a 15% difference in fracture strain between samples tested under the same conditions (refer to Figure 4.4(a) on page 59 for example). The apparent difference in the fracture strain may be the result of the measurement technique used for RA measurements, or be due to the presence of an internal flaw which could cause the fracture process to be initiated at different amount of deformation.

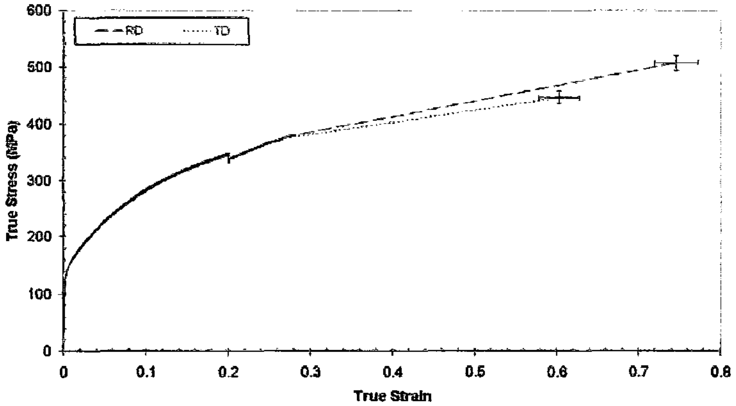

Figure 4.40: Samples tested to fracture parallel and perpendicular to the rolling direction after an intermediate polish at 20%

4.5.2 Surface Parameters

The WYKO system was used to measure the roughness on all the samples tested to uniform strains, as well as in the necked region of the sample with an intermediate polish tested to fracture. Figure 4.41 shows the average roughness for samples tested parallel and perpendicular to the rolling direction. The ten-point mean roughness measurement show the same trend. It is assumed from previous experiments that both the average roughness and ten-point mean roughness increase linearly with strain upon testing after initial surface preparation. As such, roughness measurements were only taken from an initially polished sample tested to 20% true strain and not at any true strain values below 20%. After the intermediate polish, both roughness parameters begin to increase linearly with strain immediately upon testing regardless of orientation. Both the average and ten-point mean roughening rates do not change after the intermediate polish.

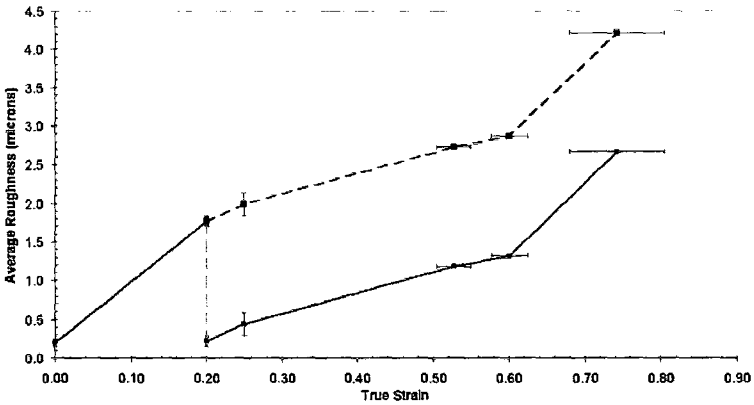

(a) Tested Parallel to the Rolling Direction

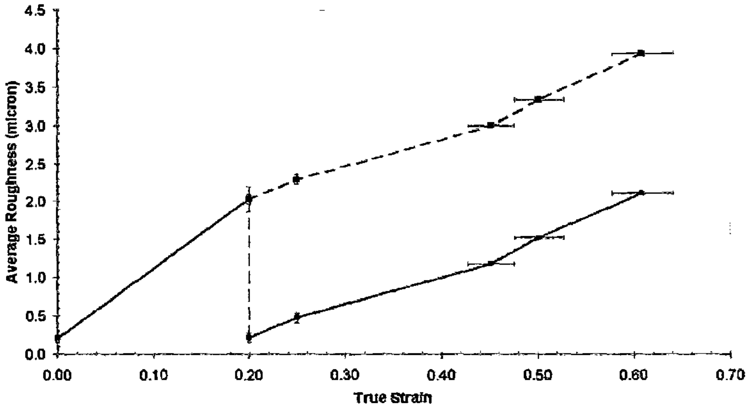

(b) Tested Perpendicular to the Rolling Direction

Figure 4.41: Average Roughness for Samples with an Intermediate Polish at 20% true strain; Roughness measurements after 20% are adjusted to show that roughness continues to increase linearly after the intermediate polish.

4.6 Results Summary

Regardless of either the testing temperature or the temper treatment, the roughness increased linearly with strain. The ten-point mean roughen rate for all test conditions increased quicker with respect to strain than the average roughening rate. The average roughening rate did not differ significantly between samples tested at different temperatures or between samples with different temper treatments with respect to orientation.

The surface of samples given an intermediate polish after deforming to 20% true strain began roughening when further deformed. There appeared to be no difference in the average rate of roughening between samples with only an initial surface polish and those with an intermediate polish.

Surface roughening appears to be a strain driven effect, evolving as the amount of deformation increases. However, there appears to be some influence of the grain shape on the development of the surface morphology. Other researchers have also investigated to role of grain size on roughening for a variety of materials.

Chapter 5

Discussion

This study investigated two material parameters and their effect on the development of surface roughness in sheet DC AA6111 aluminum alloy: the strain hardening rate and the material yield strength. For each strain hardening rate and strength test condition, samples were also tested with two orientations, parallel and perpendicular to the rolling direction, to assess the role of sheet anisotropy on surface development. The development of surface roughness occurs over several lengths scales, most notedly mesoscopic (grain-to-grain) and microscopic (multi-grain) scales. This chapter is organized into two main areas; the first discusses the results from specific experimental trials (dependence on strain hardening rate, dependence on strength and dislocation-precipitation interaction, redevelopment of surface features after straining, and effect of material orientation) and the second discusses the development of roughness with respect to the wavelength and amplitude of the developing surface features.

5.1 Dependence on Strain Hardening Rate

Altering the strain hardening rate can be accomplished using a variety of techniques. For this study it was important to keep factors known to affect roughness, such as crystal structure, grain size, texture, and thickness, the same throughout the sample set while only changing the strain hardening rate. Changing the test temperature affects the strain hardening rate by altering the rate of dislocation annihilation, or dynamic recovery, and thus changes the overall softening rate. This results in a higher strain hardening rate with a decrease in temperature. However, it does not alter the other parameters previously mentioned. Three different strain hardening rates were achieved by testing under three different test temperatures; 295K, 212K, and 77K. Comparing plots of the resulting average or ten-point roughness parameter with respect to true strain shows that there is no significant difference in the roughening rate between the three strain hardening rates. The roughening rate increases linearly with strain, as shown in Figure 4.10. The lack of a significant change in both the roughening rate and in the surface morphology with a change in strain hardening rate due to a decrease in the softening rates indicates that movement of the surface grains is not influenced by the net hardening rate. The roughness had the same magnitude with respect to strain regardless of the stress required to attain that amount of strain. Wu and Lloyd [24] report that their model indicates that as the strain hardening rate, as given by n, is decreased from 0.31 to 0.21, the averaged mean roughness increased from 1.91 to 2.38. However, the hardening model used by Wu and Lloyd is based on the single slip hardening rate as given by:

$$h_{(\beta)} = h_o \left(\frac{h_o \gamma_a}{\tau_o n} + 1 \right)^{n-1} \tag{5.1}$$

where τ_o is the initial critical shear stress, h_0 is the initial hardening rate, n is the hardening component, and γ_a is the accumulated slip. However, it is not known how this value of n relates to the n-value as given by Equation 3.1. The range of n-values investigated by varying the test temperature study ranged from 0.276 to 0.327 for samples tested parallel to the rolling direction and 0.274 to 0.316 for samples tested perpendicular to the rolling direction. The corresponding K values are given in Table 4.3. Becker [13] stipulated that crystallographic texture, strain hardening rate and materials homogeneities also affect the development of surface roughness. However, results presented in this work disagree with Becker's assertions. There was no change in the roughening rate with respect to the strain hardening rate over this range. Wu et al. [19] report that the strain hardening rate does not affect roping, however this assertion could not be verified as the consistent long range roughening features associated with roping did not manifest themselves on the surface of the materials used in the current work.

5.2 Dependence on Strength and Dislocation-Precipitate Interaction

AA6111 is a heat treatable aluminum alloy. The density and size of precipitates can easily be altered by subjecting the material to different heat treatment schedules. The precipitation sequence for aluminum alloys with the AA6111 composition is reported to be [27]:

$$SSS \rightarrow clusters/GP \quad zones \rightarrow \beta'' + Q \rightarrow equilibruim \quad Q + Mg_2Si$$

To determine if the dislocation distribution within individual grains, which affects how the grain reacts plastically, affects the development of surface roughness, samples were prepared with three different heat treatments; T4, T6, and OA, and tested at room temperature. Research done by Wang et al. [27] report that the T6 temper (artificially peak aged), which is aged at 180^{0}C, has shearable precipitates while samples peak aged at 250^{0}C have non-shearable precipitates. TEM images of the T6 temper and the peak aged at 250^{0}C for 30 minutes are shown in Figure 5.1. The OA temper using during the course of this study is based on Wang et al.'s peak aged at 250^{0}C, but was aged for 1 hour instead of 30 minutes. Further study conducted by Poole et al. [36] show a difference between temper treatment and visible surface slip lines. Samples aged at 180^{0}C for 7 hours, which is very similar to the T6 treatment used in this study, have visible surface slip lines while samples aged at 250^{0}C for 30 minutes show very few surface slip lines. Further, there were no visible slip lines on samples aged at 250^{0}C for over 7 days, as shown in Figure 5.2.

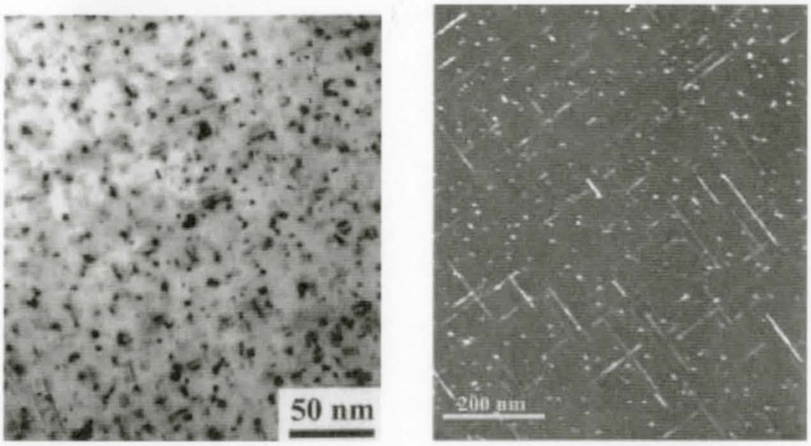

(a) TEM bright field image of sample aged at 180^{0}C for 7 hours - T6. From [27]

(b) TEM dark field image of sample aged at 250^{0}C for 30 minutes. From [28]

Figure 5.1: TEM Images of both T6 temper and peak aged at 250 ^{0}C.

The difference in the precipitate size and distribution between the three tempers affects the motion of dislocations and the distribution of slip. This has several effects, two being changes in the yield stress and the rate of hardening which subsequently affects the overall strain hardening rate. Comparing the measured roughness parameter versus true strain for all three temper treatments reveals that there is no appreciable difference in the roughening rate regardless of the slip distribution, as shown in Figure 4.27 There is also no significant change in surface morphology. Choi et al.[20] observed that grains with visible slip lines tended to exist in valleys while grains without visible slip lines tended to exist in peaks. However, as shown in Figure 2.3, two neighbouring grains that do not shown slip lines (Figure 2.3(b)) still exhibit a noticeable amount of rotation with respect to each other (Figure 2.3(c)). It is possible that the presence of slip lines on the surface may only indicate the

(a) 180^{0}C for 7 hours (b) 250^{0}C for 30 minutes (c) 250^{0}C for 7 days

Figure 5.2: Surface Slip Lines after 5% deformation for three different Heat Treatments. Courtesy of Dr. Xiang Wang

slip characteristics within the grains, and the resulting roughness development is mainly a result of the interaction between grains.

The process governing the initiation and development of surface roughness features does not seem to be affected by the stress level required to initiate deformation. Changes in the yield strength, as given by the 0.2% offset yield strength, do not affect the roughening rate. After the onset of plasticity, the roughening rate continues to increase linearly with strain regardless of temper treatment. However, as shown in Figure 4.25, there are distinct changes in the strain hardening rate between the three tempers. The overall strain hardening rate for samples tested with different temper treatments is altered by the increase in the rate of hardening due to precipitate affect. As shown in Figure 4.27, the average roughness does not change with respect to the temper tested, only with strain. The same is true of the ten-point mean roughness. The amount of stress (load) required to cause strain (deformation) does not affect the process of deformation roughness development. The development of roughness on free surface of a material seems to only depend on the amount of strain imparted on the material.

5.3 Development of Surface Features Upon Deformation

To further investigate the relationship between the formation of surface features and strain, T4 samples tested at room temperature were given an intermediate polish after being deformed to 20% true strain. Upon subsequent deformation, the surface roughness redeveloped at a constant rate with respect to strain as shown in Figure 4.41. The roughening rate of the surface remained the same before and after the intermediate polish for both testing orientations. The development of surface roughness is not dependent on the strain history of the sample. It is well documented [4, 7, 8, 9, 11, 10, 13] that the development of surface roughness with strain is linked with the rotation of surface grains, causing some of the grains to move out of plane. The grains will rotate at the same rate with increasing strain and the magnitude of the surface features will develop at the same rate with respect to strain regardless of previous deformation. It is only dependent on the relative amount of strain imparted on the material after the surface was modified. Grain rotation does not appear to be affected by previous deformation and is not a damage process.

5.4 Material Orientation

The effect of the relationship between the tensile axis and the rolling direction on surface roughness was systematically investigated by testing samples with 2 orientations: parallel and perpendicular to the rolling direction. The resulting roughness did not appreciably differ between either test orientation with respect to strain regardless of test condition. The average roughness and the ten-point mean roughness remained the same with respect to orientation.

However, there appeared to be a weak dependence between the test orientation and the shape of developing surface features. LaserScan surface maps taken over an 8mm by 5mm area, as seen in Figures 4.13 and 4.32, show a greater occurrence of longer-range surface features when samples were tested perpendicular to the rolling direction regardless of strain hardening rate or strength. On the samples tested perpendicular to the rolling direction at various temperatures there appears to be a weak relationship between the formation of long-range features and orientation. There is a possibility that small ridges have formed parallel to the rolling direction, as shown as a series of small repeating bumps in Figure 4.13(b). The relative height difference between long-range ridges and valleys is very small compared to the heights of the individual grain clusters, and is not visible on the surface. The presence of these longer range surface features would probably not be detected without the use of surface map analysis. Optical images of the surface revealed no indication of obvious roping/ridging in any test condition. However, published papers which look at the development of roping state that the development of such a morphology is dependent on orientation; a roping/ridging morphology forms when the sheet is tested perpendicular to the rolling direction, not when tested parallel to the rolling direction in uniaxial tension [13, 19, 21, 23, 25]. Samples tested at other test conditions did not show any significant repeating spatial distance. The lack of a distinctly repeating spatial distance between surface features further showed that the samples tested during this study did not develop surface features with a strong long-range relationship, such as roping/ridging.

5.5 Wavelength of Roughening

The wavelength of roughening refers to the length scale over which surface features form. LaserScan surface maps reveal distinct features that occur at different heights on the surface. These features often take the form of grain clusters. LaserScan surface maps were taken on T4 sample tested at room temperature to three different strains before the onset of necking, as shown in Figure 4.29. The differences in the size and distribution of the grain clusters that do exist between scans at different strains can be attributed to analyzing different samples and the vertical scale used.

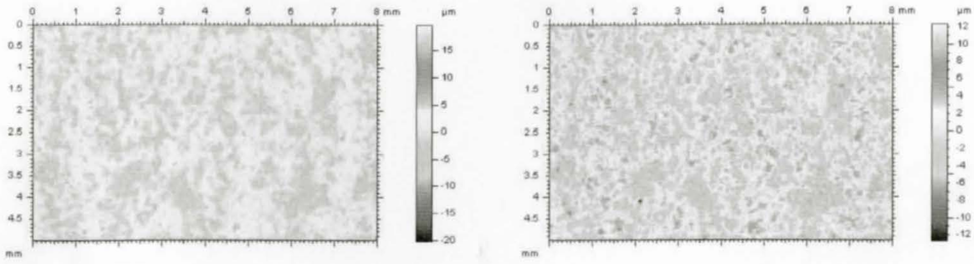

(a) 40μm vertical scale (b) 25μm vertical scale

Figure 5.3: LaserScan surface map of T4 Sample tested to 15% at room temperature perpendicular to the rolling direction with two different vertical scales. Images in greyscale

In order to compare the changes on the surface, all the LaserScan maps for above mentioned series were vertically scaled over for range of 40μm. If the scale were smaller, more features would be visible on the maps at smaller strains. For example, Figure 5.3 shows a T4 sample tested to 15% true strain at room temperature perpendicular to the rolling direction scaled to a vertical range of 40μm and 25μm respectively. Notice that the scan shows more features with the finer scale.

Analysis done on the LaserScan surface maps for all test conditions using the covariance function reveals that the wavelength of roughening does not significantly change with either increasing strain, changes in strain hardening rate, or strength. There is a characteristic surface feature separation distance of 2.4 to 2.6 average grain sizes regardless of orientation, test condition or amount of deformation. Individual peaks and valleys are between two to three grains big respectively. Examining the composite micrographs taken of the surfaces reveals that the appearance of these features does not significantly change between different sets of test conditions, nor between testing orientation. Surface features seem to develop early at low strains, and do not change their shape significantly with increasing strain. A systematic investigation of the development of surface features on one sample with respect to strain was not conducted during this study. Due to using multiple samples and the potential masking effect of the scale chosen, the relationship between imposed strain and any potential shape or size change in the surface features cannot be directly determined from this study. Thomson and Nayak [5] report that new feature emerge at intermediate and high strains as well as at lower strains. It is unknown whether this also occurs in this material as different samples were used. It is also possible that the same masking effect, due to vertical resolution, occurred during their measurements.

The spatial distribution of surface features is linked to the texture distribution on the surface of the sample as well as the texture components present. As outlined in Section 2.7, the presence of different texture component pairs and their layout on the surface can greatly affect the surface's morphology. The distribution of selected crystallographic texture components, as outlined in Table 2.1, is reported to greatly affect the surface morphology. However, due to the limited nature of the ESBD analysis done during this study, the distribution of the texture components over the entire surface of the region investigated is unknown. Thus, any relationship between the development of the morphology of the surface with respect to strain and the texture components present could not be determined.

5.6 Amplitude of Roughness

Although the size and shape of the surface features does not appear to change with increasing strain, the amplitude, or depth, of the features does change significantly with increasing strain. The LaserScan surface maps of the T4 sample tested at room temperature to different strains shows a marked increase in the amplitude of the surface features with increasing strain, as shown in Figure 4.29. The resulting increase in measured roughness is linear with increasing strain. For all the test conditions investigated, including the sample set with the intermediate polish, the roughening rate remained the same. The linear increase in measured roughness parameter with increasing strain is well documented [4, 5, 7, 8, 9, 11, 13]. Wilson and Roberts [7] and Wilson et al. [8] report one distinct deviation from the linear relationship between developing roughness and increasing strain occurs just after the onset

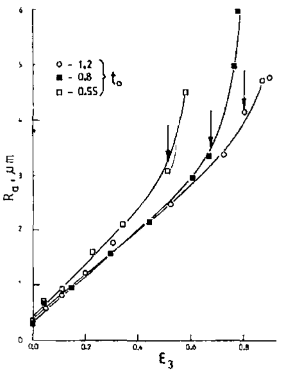

Figure 5.4: Deviation of measured roughness from linearity after the onset of necking, as indicated by the vertical arrows. From [8]

of localized necking, as indicated in Figure 5.4 by the vertical arrows. Comparing Figure 5.4 to Figures 4.11 and 4.28 on pages 69 and 90 respectively, the drastic increase in the average roughness over a small range of strain after the onset of localized necking does not occur in any of the test condition investigated in this study. Wilson et al. used a stylus-type profilometer in their study, which typically uses a relatively long scan length. It is possible that measurement made during their study captured features over a larger distance than simply within the groove caused by necking. As such, the calculated average roughness would show a significant increase after the onset of necking, just as indicated in their paper.

The increase in roughness with increasing strain is reported to be related to the grain size as given by Equation 2.1. Fitting the data for each test condition to a linear trend line and taking $d_o = 87.1\mu m$ and averaging the resulting values, the constant K is calculated to be 0.078. Sarkar et al. [35] have roughness results for AA6111 with two different grain sizes; 40μm and 110μm. The data was presented as an initial roughness value, and one taken at 25% true strain. Linear roughening with respect to strain was assumed and the roughness trend is plotted as a dashed grey line. Comparing their data to a sample tested during this study with the same heat treatment (T4) tested perpendicular to the rolling direction, the sample with the 110μm grain size has a very similar roughening rate. However, the sample with the average grain size 40μm lower shows a marked decrease in its rough-

Table 5.1: Calculated Material Constant K values for Sarkar et al.

Grain Size	Material Constant K
40μm	0.12
110μm	0.084

ening rate, as shown in Figure 5.5. The calculated K values for these sample sets are shown in Table 5.1. The sample with a grain size of 110μm has a very similar value to the one calculated for material used in this study. However, this K values is much higher for Sarkar et al.'s sample with the reduced grain size. For a grain size of 40μm tested to 25% true strain using K = 0.078, the resulting increase in roughness would be 0.78 μm, only 0.5 μm lower than Sarkar et al.'s calculated value of K for the same grain size. Using K = 0.078, the grain size required to reduce the average roughness at 20% true strain to a quarter of its current value is 27μm. If the material had an average grain size of 1 μm, the average roughness would further reduce to 0.016μm at 20% strain.

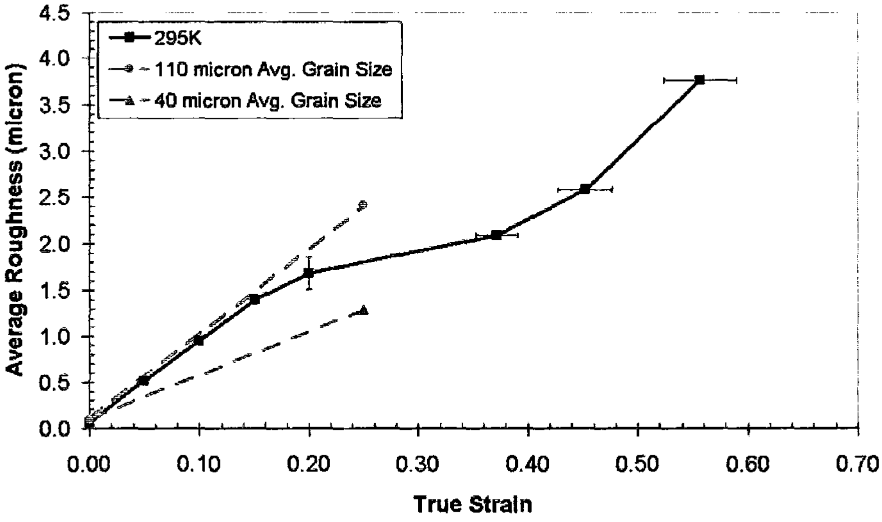

Figure 5.5: Comparison of data on T4 material tested perpendicular to the rolling direction with Sarkar et al. Includes data from [35].

In order to make use of the benefits of a smaller grain size, the size of the surface grains has to be reduced. Work done by Weck [37] investigating the coalescence of voids by drilling holes into commercial purity aluminum using a femtosecond laser reveals a drastically smaller grain size in the region near the holes as compared to the bulk material. The average grain size of the bulk material is 10μm while the average grain size in the heat affected region near the holes ranges between 5-10nm, as shown in Figure 5.6. The depth of the fine-grain region can be altered by changing the fluence, or power of the laser. The rapid cooling of the melted material due to the laser pulses is thought to be the likely cause for the smaller grain size. It is conceivable that the grain size of the surface grains in sheet aluminum could also be reduced using a similar technique, thus reducing the amplitude of roughening significantly. Using Equation 2.1 with K=0.078, a sheet with an average grain size of 10nm deformed to 20% strain would have an approximate average roughness increase of only 0.0002μm, which would be negligible compared to the starting roughness of the sheet. Such a drastic reduction in grain size would be coupled with an equally drastic reduction in the amount of roughness as a result of deformation.

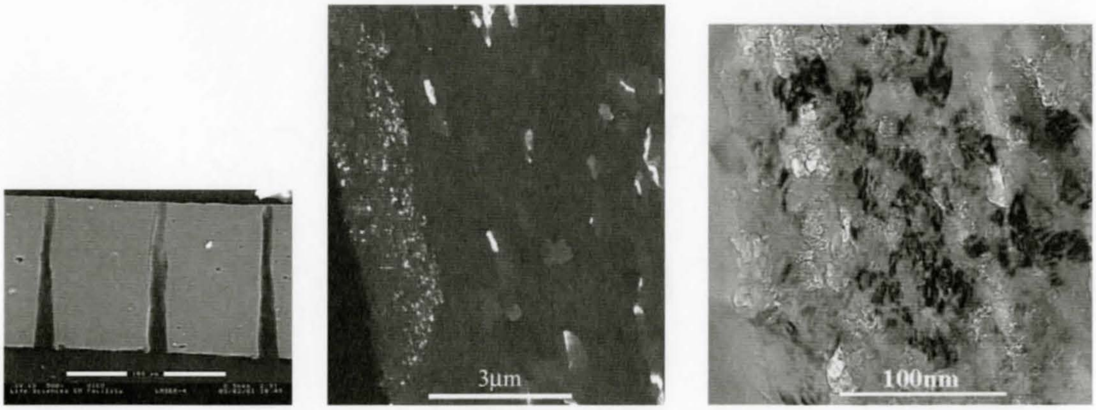

(a) Cross section of Drilled Holes

(b) Heat Affected Region (HAR) of one Hole

(c) Close-up View of HAR

Figure 5.6: Change in Grain Size at sides of Holes Laser Drilled in Commercial purity (99.99%) Aluminum. Courtesy of Arnaud Weck. Laser Parameters: 150femtoseconds, E=10?J, Nb-pulses/hole=1000, Env.. air, spinning half wave plate. This set-up allows the drilling of 10μm in diameter holes through 100μm thick sheets.

In rolled sheet, the average grain size differs with sheet orientation. The material used in this study had an average grain size of 87.1 μm in the rolling/transverse direction. However, the grain size measure parallel to the normal plane was 27.4 μm, approximately one third smaller. Surface roughness measurements in this study were only taken on the surface in the rolling/transverse plane. The relationship between grain shape and the development of surface roughness was not investigated during the course of this study.

Chapter 6

Conclusions

The measured surface roughness increased linearly with strain with the same rate regardless of strength or strain hardening rate. The process of roughness development appears to be a primarily strain driven, and is independent of the amount of stress the material is subjected to with respect to strain. It is a result of grain-to-grain interactions during deformation. The surface features on samples given an intermediate polish at 20% true strain increased in magnitude at the same rate as those that developed upon straining from 0% true strain. As such, surface features redevelop and grow at the same rate regardless of strain history and are not an indication of damage, which is irreversible.

The developed morphology of the surface is dependent on the relationship between the tensile axis and rolling direction. The wavelength of the surface features is not affected by changes in strain hardening rate or strength. Features have a distinct spatial relationship of 2.4 to 2.6 average grain sizes. Surface features occur on the order of that characteristic length. Both individual peaks and valleys are two to three grains large. When tested perpendicular to the rolling direction,a weak relationship emerged: longer-range surface features developed parallel to the rolling direction. However, this relationship between orientation and surface morphology was not significant enough to form a distinct roping/ridging morphology. Although it was not investigated in this study, the main factor in the development of surface morphology is believed to be related to crystallographic texture, both texture distribution and the texture components present. Any change in the number and size of the surface features with increasing strain cannot be directly determined from this study. A systematic study on the development of one sample needs to be done for verification. The amplitude of the surface features increases with increasing strain, leading to the well reported linear increase in surface roughness with increasing strain. As grains are strained, they rotate to relieve the strains that develop at the grain boundary. Grains can either rotated upwards out of the surface plane to form peaks, or down into the surface to form valleys. The governing factor controlling the magnitude of the amplitude is the size of the grains. The smaller the grain size, the smaller the developed roughness for an equivalent strain. To illustrate, if Eqn. 2.1 is used as a first approximation of how much a surface roughens with respect to grain size and strain, the peaks and valleys resulting from grain rotation due to deformation of close to nano-sized grains will not significantly alter the surface. Essentially the material will not appreciably roughen.

Bibliography

[1] Takakura, N., Yamaguchi, K., Fukuda, M. (1987) JSME International Journal Vol. 30 No. 270 pg. 2034-2039

[2] Raabe, D., Sachtleber, M., Weiland, H., Scheele, G., Zhao, Z. (2003) Acta materialia Vol. 51 pg. 1539-1560

[3] Dallas, Daniel (Ed.) (1976) Tool and Manufacturing Engineers Handbook 3rd Ed. USA: McGraw-Hill

[4] Shimizu, I., Okuda, T., Abe, T., Tani, H. (2001) JSME International Journal Series A Vol. 44 No. 4 pg. 499-506

[5] Thomson, P.F., Nayak, P. U. (1980) Int. J. Mach. Tool Des. Res. Vol. 20 pg. 73-86

[6] Tong, W., Hector Jr., L. G., Weiland, H., Wieserman, L. F. (1997) Scripta Materialia Vo. 36 No. 11 pg. 1339-1344

[7] Wilson, D. V., Mirshams, A. R., Roberts, W. T. (1983) Int. J. Mech. Sci. Vol. 25 No. 12 pg. 859-870

[8] Wilson, D. V., Roberts, W., T., Rodrigues, P.M.B. (September 1981) Met. Trans A Vo. 12A pg. 1595-1602

[9] Stoudt, M. R., Ricker, R. E. (September 2002) Meta Mater Trans Vol. 33A pg. 2883-2889

[10] Kawai, N., Nakamura, T., Ukai, Y. (April 1986) Bulletin of JSME Vol. 29 No. 250 pg. 1337-1343

[11] Guangnan, C., Huan, S., Shiguang, H., Baudelet. (1990) Mater. Sci. Eng. Vol. A128 pg. 33-38

[12] Thomson, P. F., Shafer, B., V. (1982) Int. J. Mach. Tool Des. Res. Vol. 22 No. 4 pg. 261-264

[13] Becker, R. (1998) Acta mater. Vol. 46 No. 4 pg. 1385-1401

[14] Baczynski, G. J., Guzzo, R., Ball, M. D., Lloyd, D. J. (2000) Acta mater. Vol. 48 pg. 3361-376

[15] Porter, D. A. and Easterling, K. E. (1981) Phase Transformations in Metals and Alloys. Great Britain: Van Nostrand Reinhold Company Ltd.

[16] Randle, Valerie and Engler, Olaf. (2000) Introduction to Texture Analysis-Macrotexture, Microtexture and Oientation Mapping. Singapore: Gordon and Breach Science Publishers

[17] Wittridge, N. J., Knutsen, R. D. (1999) Materials Science ad Engineering Vol. A269 pg. 205-216

[18] Hatch, J. E. [Ed.] (1984) Aluminum: Properties and Physical Metallurgy. USA: American Society for Metals.

[19] Wu, P. D., Lloyd, D. J., Bosland, A., Jin, H., MacEwan, S. R. (2003) Acta materialia vol. 51 pg. 1945-1957

[20] Choi, Y. S., Piehler, H. R., Rollett, A. D. (Feb. 2004) Metall. Mater. Trans. Vol. 35A pg. 513-524

[21] Beaudoin, A. J, Bryant, J. D., Korzekwa, D. A. (Sept. 1998) Metallurgical and Materials Trans Vol. 29A pg. 2323-2332

[22] Lee, P. S., Piehler, H. R., Adams, B. L., Jarvis, G., Hampel, H., Rollett, A. D. (1998) J. of Materials Processing Technology Vol. 80-81 pg. 315-319

[23] Winson, D. V., Roberts, W. T., Rodrigues, M. M. B. (Sept. 1981) Metallurgaical Trans. Vol. 12A pg. 1603-1611

[24] Wu, P. D., Lloyd, D. J. (2004) Acta Materialia Vol. 52 pg. 1785-1798

[25] Zhao, Z., Radovitzky, R., Cuitiño, A. (2004) Acta mater. Vol. 52 pg. 5791-5804

[26] Hosford, William F., Caddell, Robert M. (1993) Metal Forming New Jersey: Prentice-Hall pg. 310-311

[27] Wang, X., Poole., W. J., Esmaeili, S., Lloyd, D. J., and Embury, J. D. (Dec. 2003) Metallurgical and Mater Trans A Vol. 34A pg. 2913-2924

[28] Poole, W.J., Lloyd, D. J., Embury, J. D., (1997) Mater Sci Eng Vol. A234-236 pg. 306-309

[29] Huang, X., Hansen, N. (1997) Scripta Materialia Vol. 37 No. 1 pg. 1-7

[30] Gimple, J. (August 2001) M. Eng. Thesis. McMaster Univeristy.

[31] White light interferometry - a method for height profile measurement of technical surface (n.d.). Retrieved January 15, 2005 from http://rco.upol.cz/optics/research/witelite/wli_2.htm

[32] Solarius: Confocal Measurement (n.d.). Retrieved January 15, 2005 from http://www.solarius-inc.com/html/confocal.html

[33] Misumi: Technical Data (n.d.). Retrieved January 15, 2005 from http://www.misumiamerica.com/technical/pdf/usa_pdf_tech_p1381.pdf

[34] Influence of Counterpace Material Compatibility on Interface Behavior (n.d.). Retrieved January 16, 2005 from http://www.prism.gatech.edu/ gt0126b/research.htm

[35] Private Communication from Dr. D. S. Wilkinson: Department of Materials Science and Engineering, McMaster University; Full Paper Authors - J. Sarkar, K.T. Conlon, A.D. Rollett, M.D. Ball, D.S. Wilkinson, J.D. Embury and D.J. Lloyd.

[36] Poole, W. J., Wang, X., Lloyd, D. J., Embury, J. D. (2005) Accepted for publication in "Philosophical Magazine"

[37] Private Communication with Arnaud Weck: Department of Materials Science and Engineering, McMaster Univesity, August 10, 2005